



**HAL**  
open science

# Nonlinear transient analysis of isotropic and composite shell structures under dynamic loading by SPH method

Jun Lin

► **To cite this version:**

Jun Lin. Nonlinear transient analysis of isotropic and composite shell structures under dynamic loading by SPH method. Other. Université de Technologie de Compiègne, 2014. English. NNT : 2014COMP2138 . tel-00997702

**HAL Id: tel-00997702**

**<https://theses.hal.science/tel-00997702v1>**

Submitted on 28 May 2014

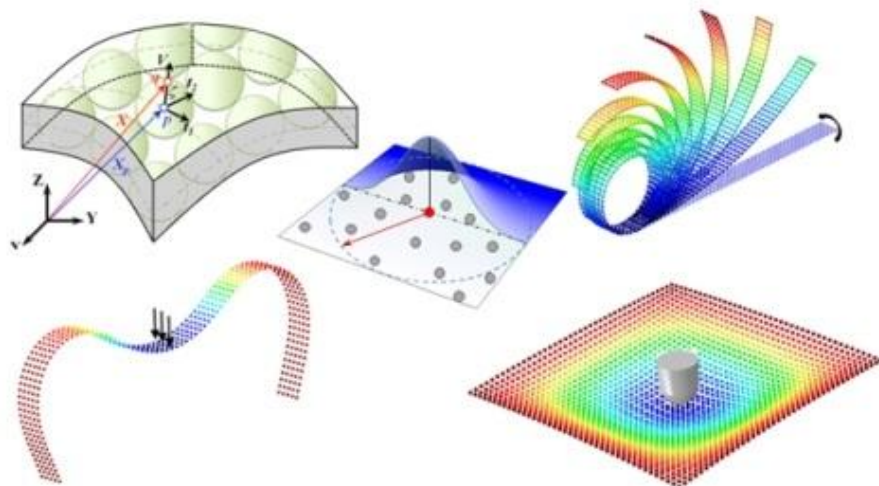
**HAL** is a multi-disciplinary open access archive for the deposit and dissemination of scientific research documents, whether they are published or not. The documents may come from teaching and research institutions in France or abroad, or from public or private research centers.

L'archive ouverte pluridisciplinaire **HAL**, est destinée au dépôt et à la diffusion de documents scientifiques de niveau recherche, publiés ou non, émanant des établissements d'enseignement et de recherche français ou étrangers, des laboratoires publics ou privés.

Par Jun LIN

*Nonlinear transient analysis of isotropic and composite shell structures under dynamic loading by SPH method*

Thèse présentée  
pour l'obtention du grade  
de Docteur de l'UTC



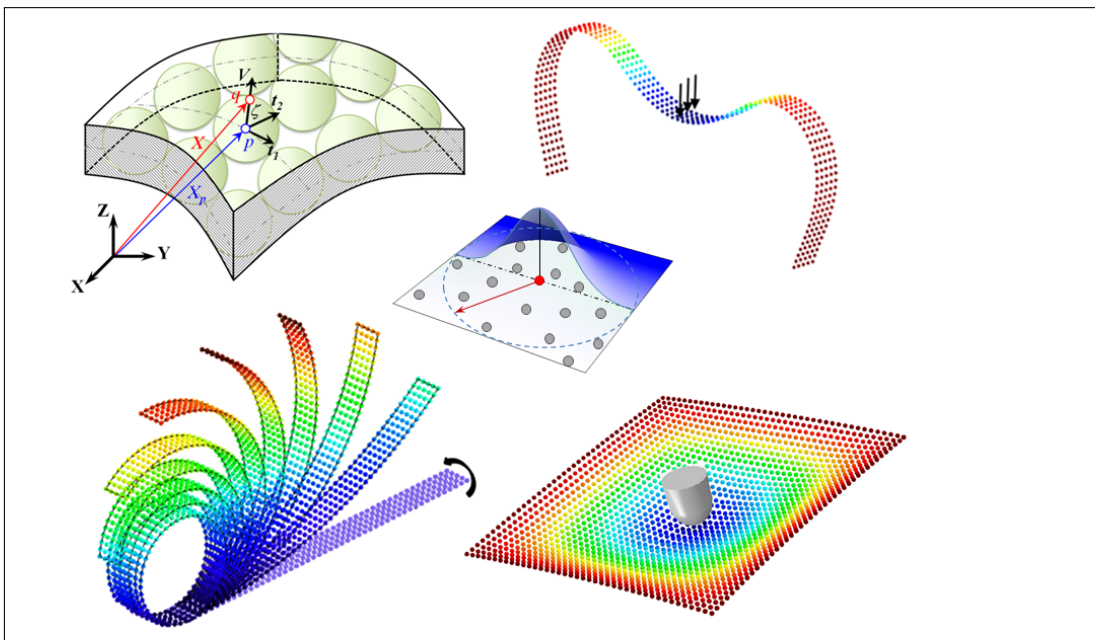
Soutenue le 02 avril 2014  
**Spécialité** : Mécanique avancée

D2138

par **Jun LIN**

***Nonlinear transient analysis of isotropic and composite shell structures under dynamic loading by SPH method***

Thèse présentée  
pour l'obtention du grade  
de Docteur de l'UTC.



Soutenu le : 02 avril 2014

**Spécialité** : Mécanique avancée



# Nonlinear transient analysis of isotropic and composite shell structures under dynamic loading by SPH method

Thèse soutenue le 02 avril 2014 devant le jury composé de :

Prof	WU Jianjun	Northwestern Polytechnical University, Xi'an	(Rapporteur)
Prof	IORDANOFF Ivan	ENSAM de Bordeaux	(Rapporteur)
Prof	RASSINEUX Alain	Université de Technologie de Compiègne	
Prof	COUTELLIER Daniel	Université de Valenciennes	
Prof	LAKSIMI Abdelouahed	Université de Technologie de Compiègne	(Directeur de thèse)
Prof	NACEUR Hakim	Université de Valenciennes	(Co-directeur de thèse)



*I lovingly dedicate this thesis to my parents, my wife and my sister for  
their understanding and encouragement*





---

# *Acknowledgements*

---

First of all, I would like to express my profound gratitude to my supervisor Prof. Hakim NACEUR, for his sincere and patient guidance and help along this academic journey. He believed in me and encourages me constantly, keeping me motivated throughout this long journey. He is not only a great supervisor, but also a very good friend. I believe that the experience working with him will be of much benefit in my future scientific life.

I owe special gratitude to Prof. Abdelouahed LAKSIMI, for giving me the opportunity to work in UTC. He allowed me all the freedom I wanted to follow my own steps and offered me tremendous support and advice which are invaluable for this thesis.

Besides my supervisors, I feel very lucky to get precious suggestions and support from Prof. Daniel COUTELLIER and Dr. Jamila RAHMOUN. I would like to show my heartfelt appreciation to you.

I would like to gratefully acknowledge Prof. WU Jianjun, Prof. IORDANNOF Ivan, Prof. RASSINEUX Alain for their acceptance to participate in the evaluation committee of this thesis.

I am indebted to the CSC (China Scholarship Council) for the scholarship and the opportunity of the study in France.

I would like to express my sincere gratitude to my colleagues, Thanh Loan NGUYEN, Lukasz KURPASKA, Amira JAZIRI, Joseph HENRY, Ha Manh HUNG and Khanh-toan TRAN who helped me a lot to habituate the work and life in France.

Special thanks would be paid to my lovely friends, Weiting TIAN & Weidong DANG, Xiaojuan JIA & Baochao WANG, Lei QIN, Shengcheng Ji, Manyu XIAO, Erliang ZHANG, Yang XIA & Mengdi SONG, Jianquan LUO, Bin DONG, Fang WANG & Zhenzhou ZHU, Dan LIU, Liguozhang ZHANG, Yingjuan ZHAO, Pengfei HUYAN, Peng CAO, Yang Song, Dingfu ZHOU, Xiaodong WANG, Liang XIA in Compiègne, and Yingshuang XIE, Yufei ZHANG, Guijin YAO, Yaojie SHI, Yuxi CUI, Sicong LIU, Amina LAOUIRA, Wassem ARIF, and Jimin GUAN in Valenciennes, etc. Without you, my life would be dark in France.

I'd like to thank my parents and my sister, your unconditional love and understanding are my lifeblood.

Finally, this dissertation is dedicated to my wife, Jiao LI, for your endless love, neverending support and long wait, making me never fear and move forward.

---

# *Contents*

---

<b>Acknowledgements</b>	<b>vii</b>
<b>Table of Contents</b>	<b>ix</b>
<b>List of Tables</b>	<b>xiii</b>
<b>List of Figures</b>	<b>xv</b>
<b>1 General Introduction</b>	<b>1</b>
1.1 Introduction . . . . .	1
1.2 Meshless methods . . . . .	2
1.3 SPH method and its applications . . . . .	4
1.4 Motivations and outline of the thesis . . . . .	6
1.4.1 Motivations . . . . .	6
1.4.2 Outline of the thesis . . . . .	8
<b>2 SPH formulation for 2D solids</b>	<b>11</b>
2.1 Brief recall of basic continuum mechanics relations . . . . .	11
2.1.1 Kinematics . . . . .	11
2.1.2 Constitutive relations . . . . .	13
2.1.3 Principle of mass conservation . . . . .	13
2.1.4 Principle of conservation of linear momentum . . . . .	14
2.1.5 Principle of conservation of angular momentum . . . . .	15
2.1.6 Principle of conservation of energy . . . . .	16
2.2 SPH foundation . . . . .	17
2.2.1 Approximation of a field variable . . . . .	17
2.2.2 Smoothing function . . . . .	18
2.2.3 Approximation of field derivatives . . . . .	20
2.3 SPH discretization of the equilibrium equations of solids . . . . .	20

2.4	Inconsistency problems and corrective techniques . . . . .	21
2.5	Artificial viscosity . . . . .	24
2.6	Extension of the SPH method using the Total Lagrangian Formulation . . . . .	25
2.7	Time step and time integration . . . . .	28
2.8	Numerical applications . . . . .	30
2.8.1	Geometrically linear analysis . . . . .	30
2.8.2	Geometrically nonlinear analysis . . . . .	34
2.9	Conclusion . . . . .	46
<b>3</b>	<b>SPH formulation for isotropic shell structures</b>	<b>47</b>
3.1	Overview of shell modeling using meshless methods . . . . .	47
3.2	Kinematics of shell structures using SPH discretization . . . . .	49
3.3	Constitutive relations and dynamic equilibrium equations . . . . .	53
3.4	SPH implementation for shell structures . . . . .	54
3.5	Treatment of large rotations of shells using the SPH method . . . . .	55
3.6	Numerical applications . . . . .	57
3.6.1	Large deflection of cantilever beam under transverse loads . . . . .	57
3.6.2	Roll-up of a clamped plate . . . . .	60
3.6.3	Large deformation of a square plate under uniform load . . . . .	62
3.6.4	Post-buckling of the Euler column . . . . .	64
3.6.5	Nonlinear analysis of a clamped circular arch . . . . .	67
3.6.6	Nonlinear Analysis of a Plate Buckling . . . . .	70
3.6.7	Geometrically Nonlinear Analysis of a cylindrical roof . . . . .	72
3.6.8	Snap-through of a shallow spherical shell . . . . .	73
3.7	Conclusion . . . . .	75
<b>4</b>	<b>Shell-based SPH method for thin multilayered structures</b>	<b>77</b>
4.1	Overview of laminates modeling using mesfree methods . . . . .	77
4.2	Constitutive relations of a multilayered shell structure . . . . .	80
4.2.1	Shear correction factor . . . . .	84
4.3	SPH implementation for multilayered shell structures . . . . .	86
4.4	Numerical applications . . . . .	87
4.4.1	A clamped square plate under uniform pressure load . . . . .	87
4.4.2	A hinged multilayered square plate under uniform load . . . . .	89

4.4.3	Laminated strip under three-point bending . . . . .	89
4.4.4	Composite shallow cylindrical shell with a central point load . . . . .	91
4.4.5	Laminated dome under concentrated load . . . . .	93
4.5	Conclusion . . . . .	94
<b>5</b>	<b>Low velocity impact and failure modeling of composite shells using the SPH method</b>	<b>95</b>
5.1	Brief overview on shell impact modeling . . . . .	95
5.2	Modeling of contact force and indentation . . . . .	96
5.3	Modeling of progressive failure modeling using SPH . . . . .	99
5.4	Low-velocity impact analysis . . . . .	101
5.4.1	Impact of a clamped isotropic plate by a steel sphere . . . . .	101
5.4.2	Impact of a T300/934 carbon-epoxy plate by a steel sphere . . . . .	105
5.4.3	Impact of a clamped graphite-epoxy laminate by a rigid sphere . . . . .	109
5.5	Progressive failure analysis . . . . .	113
5.5.1	Damage analysis of a carbon/epoxy square plate impacted by a point-nose projectile . . . . .	113
5.5.2	Damage analysis of a carbon/epoxy cylindrical shell panel impacted by a point-nose projectile . . . . .	117
5.6	Conclusion . . . . .	120
	<b>Conclusion</b>	<b>121</b>
5.7	General conclusion . . . . .	121
5.8	Future works . . . . .	122
	<b>Bibliography</b>	<b>125</b>



---

# *List of Tables*

---

2.1 Comparison of the end-beam deflection $W_C$ (mm) . . . . .	36
3.1 Comparison of the SPH results with Timoshenko reference solution [82] . . . . .	58
3.2 Comparison of CPU time for analysis of the beam (Present SPH vs. Continuum SPH) . . . . .	60
3.3 Summary of the principal results of the built-in Euler column . . . . .	66
3.4 Summary of the principal results of the arch . . . . .	68
3.5 Comparison of CPU time for analysis of the beam (Present SPH vs. Continuum SPH) . . . . .	75
4.1 Vertical displacement of the central point $W_C$ (mm) . . . . .	88
4.2 Non-dimensional deflection of the centroid of the plate $W_C/t$ . . . . .	89
4.3 Convergence of the laminated strip deflection $W_C$ . . . . .	90
5.1 Geometrical and material parameters of the projectile and target plate . . . . .	102
5.2 Comparison of the impact load (SPH vs. FE and Analytical solutions) . . . . .	104
5.3 Geometrical and material parameters of the projectile and the target . . . . .	106
5.4 Comparison of the impact load (SPH vs. semi-analytical solution) . . . . .	107
5.5 Maximum impact force and contact duration for the $t$ , $2t$ and $4t$ plate thickness	109
5.6 Geometrical and material parameters of the projectile and the target . . . . .	110
5.7 Maximum impact force (N) and contact duration (ms) using different projectile masses . . . . .	111
5.8 Comparison of the maximum impact load (N) and contact duration (ms) function of the initial velocity . . . . .	112
5.9 Parameters of the projectile and target . . . . .	114
5.10 Dimensions of damaged area . . . . .	116
5.11 Dimensions of damaged area . . . . .	120





---

# *List of Figures*

---

2.1 Kinematics of a continuum body . . . . .	12
2.2 Continuum of forces acting on the current configuration. . . . .	15
2.3 Modeling of a 2D structure using the SPH discretization. . . . .	18
2.4 Kernel function used in two-dimensional space. . . . .	19
2.5 Comparison of the performance between the classical SPH method (left) and the CSPM (right). . . . .	24
2.6 Clamped plate under transverse load. . . . .	26
2.7 Evolution of the plate deflection at point C, in function of time. . . . .	27
2.8 Cantilever beam with tip load . . . . .	31
2.9 Applied load evolution in time . . . . .	31
2.10 Influence of the smoothing length . . . . .	32
2.11 Influence of particles discretization . . . . .	32
2.12 Deformed configurations with different viscosity . . . . .	33
2.13 Shear stress distribution through the thickness at $x = 50mm$ . . . . .	33
2.14 Cook's membrane . . . . .	34
2.15 Configurations of Cook's membrane . . . . .	35
2.16 Final deformed configurations under maximal load (SPH <i>vs.</i> FEM) . . . . .	36
2.17 Geometry and loading of a clamped beam strip . . . . .	37
2.18 Comparison of load-displacement of the strip (SPH <i>vs.</i> FE) . . . . .	38
2.19 Deformed configuration of the strip (SPH solution) . . . . .	38
2.20 Pinned-pinned shallow arch . . . . .	39
2.21 Comparison of load-displacement path at the central point . . . . .	39
2.22 Comparison of deformed configurations of the arch at maximal displacement . . . . .	40
2.23 Clamped-clamped deep arch . . . . .	40
2.24 Velocity control factor . . . . .	40
2.25 Load-Displacement curve at the central point of the arch . . . . .	41
2.26 Predicted loading history ( $W_C = 250mm$ ) . . . . .	41

2.27	Deformed configurations of the deep arch at maximal displacement . . . . .	42
2.28	Four points bending test on a sandwich beam . . . . .	42
2.29	Force-displacement curve at point $A$ . . . . .	43
2.30	Deformed configuration of the sandwich beam . . . . .	44
2.31	Stress distribution on the top face of the sandwich beam . . . . .	45
3.1	Discretization of a shell mid-surface using SPH particles . . . . .	49
3.2	Position vectors and covariant basis in the deformed configuration . . . . .	50
3.3	Flow chart of the present shell-based SPH method . . . . .	57
3.4	Initial and deformed configurations of the clamped beam . . . . .	58
3.5	Comparison of load-displacement curve (Present SPH model vs. Analytical solution) . . . . .	59
3.6	Evolution of the deflection over time at the right end section . . . . .	60
3.7	Comparison of deformed configurations of the beam at maximum load(present SPH vs. LS-DYNA <sup>®</sup> ) . . . . .	61
3.8	Initial and intermediate configurations.using the present SPH method . . . . .	61
3.9	Comparison of load-displacement curve (Present SPH vs. FEM) . . . . .	62
3.10	Geometry of the square plate under a uniform load . . . . .	63
3.11	Load-deflection curves of the square plate . . . . .	64
3.12	Built-in Euler column buckling . . . . .	65
3.13	Evolution of the normalized axial load in function of the mid column transversal displacement . . . . .	66
3.14	Three different deformed configurations of the Euler column using the present SPH model . . . . .	67
3.15	Geometry of the deep arch . . . . .	68
3.16	Comparison of the load-displacement at the centroid of the arch . . . . .	69
3.17	Different deformed configurations of the arch: (a) Limit point SPH (b) Limit point ABAQUS (c) Maximal displacement SPH (d) Maximal displacement ABAQUS . . . . .	69
3.18	Geometry and Material characteristics of the plate . . . . .	70
3.19	Load-Deflection curve at the central plate . . . . .	71
3.20	Comparison of the deformed plate configurationsfor $P = 100N/mm$ (Present SPH vs. FEM) . . . . .	71
3.21	Hinged cylindrical roof (geometry and material data) . . . . .	72

3.22	Curve of Load-Displacement at point $C$ . . . . .	73
3.23	Deformed configuration at the vicinity of the limit point ( $W_C = 10.5mm$ ) . . . . .	73
3.24	Geometry and material data of the shallow shell . . . . .	74
3.25	Comparison of the load-displacement at the centroid of the shallow shell . . . . .	74
3.26	Initial and deformed configuration of the shallow shell for $W = 300mm$ using the present SPH model . . . . .	76
4.1	Fiber-reinforced lamina orientation axes . . . . .	81
4.2	A lamina in a plane state of stress. . . . .	81
4.3	Stacking of $NL$ material layers within the shell thickness . . . . .	83
4.4	Geometry of the square plate . . . . .	88
4.5	Geometry and loading of the laminated strip . . . . .	90
4.6	Deformed configuration of the laminated strip : (a) SPH model (b) FE model (ABAQUS <sup>®</sup> ) . . . . .	91
4.7	Composite shallow cylindrical shell . . . . .	92
4.8	Load-displacement curve . . . . .	92
4.9	Geometry of the spherical shell segment . . . . .	93
4.10	Load-displacement curve at point $C$ . . . . .	94
4.11	Deformed configuration . . . . .	94
5.1	Impact problem of two deformable spherical bodies . . . . .	97
5.2	Indentation produced by the impact . . . . .	98
5.3	Impact of a clamped isotropic plate by a steel sphere . . . . .	102
5.4	Evolution of the impact load vs. time . . . . .	103
5.5	Evolution of the velocity of the projectile and the plate centroid). . . . .	104
5.6	Evolution of the projectile stroke and the target centroid deflection. . . . .	104
5.7	Evolution of the target deflection vs. time at the impact point. . . . .	105
5.8	Evolution of the impact load vs. time (plate of thickness $t$ ) . . . . .	106
5.9	Evolution of the plate deflection and projectile stroke vs. time. . . . .	107
5.10	Comparison of predicted impact force for the $t$ , $2t$ and $4t$ plate thickness . . . . .	108
5.11	Evolution of the impact load vs. time, for $\xi_m < 1.0$ and $v = 5m/s$ . . . . .	110
5.12	Evolution of the impact load vs. time, for $\xi_m > 1.0$ and $v = 5m/s$ . . . . .	111
5.13	Comparison of the impact load function of the initial velocity, for $\xi_m = 35$ . . . . .	112
5.14	Evolution of the impact load vs. time for $\xi_m = 35$ and $v = 2.76m/s$ . . . . .	113
5.15	Superposed damage area and location . . . . .	115

5.16	Damage area of all plies . . . . .	116
5.17	Transient reponse of the laminate impacted by $1M_p$ mass projectile - Effect of matrix degradation. . . . .	117
5.18	Transient reponse of the laminate impacted by $4M_p$ mass projectile - Effect of matrix/fibers degradation. . . . .	118
5.19	Geometry of the laminated cylindrical shell panel . . . . .	119
5.20	Superposed damage area and location . . . . .	119

# *General Introduction*

---

## **1.1 Introduction**

Nowadays, numerical simulation plays an important role in solving complex practical problems in engineering and science, which are often described using ordinary/partial differential equations (ODEs/PDEs) and are often difficult to solve by analytical methods. In the numerical procedure, the physical problem is transformed into a discrete form of mathematical description and then the resulting algebraic equations derived from the ODEs/PDEs are solved using a computer code. Domain discretization is a key technique in this procedure, which divides a continuum domain into a finite number of components. The choice of the domain discretization type determines the way of numerical representation of the physical phenomenon.

Among all simulation techniques, the Finite Element Method (FEM) is well established and represents the most widespread numerical method for simulation of multi-physical problems in modern engineering. In the FEM, a finite number of discrete elements are used for subdivision of the continuum. The grid nodes and the elements connectivities constitute a computational frame for the numerical simulation. This mesh allows to perform a local approximation of the solution on each element independently using shape functions which makes ODEs/PDEs easy to solve and therefore increases the robustness of the method. Currently, an increasing number of practical engineering problems related to solids and structures are solved using well developed commercial FEM softwares.

As a prerequisite of the FEM, the predefined mesh also can present some shortcomings and often restricts the use of the FEM in certain problems. Firstly, although mesh generators have known numerous advances during the last recent decades, the procedure of obtaining a "good" mesh is still time consuming and not always fully automatic. Especially for problems involving complex geometries, the procedure of construction of a "good" mesh is typically much more time-consuming than the FE simulation itself [1].

Furthermore, the shapes of the finite elements are expected to be as ideal as possible, to insure the approximation accuracy. But in highly nonlinear problems involving large deformation, such as extrusion, forging, casting or crash, the mesh distortion arise. A FE mesh of a poor-quality may cause severe loss of accuracy or even the complete failure of computation. Remeshing techniques are commonly used to overcome this difficulty, unfortunately remeshing procedures remain time-consuming and still being tedious in most of three-dimensional industrial problems. Moreover, it is well known that the classical FEM is not suitable to simulate crack propagation with arbitrary and complex paths which normally do not coincide with the original element edges. For the naturally discrete systems such as the interaction of stars in astrophysics, the movement of millions of atoms, the FE simulation is also not suitable.

To avoid the aforementioned problems, several meshless methods have been developed since the late seventies. In these alternative methods, only particles (or nodes) are generated and scattered to represent the structure shape and special continuous weighting functions (kernels) are defined in a compact support domain at each point [2–4]. The nodes do not need to be connected to form any kind of explicitly defined elements for the simulation. Therefore, time-consuming mesh generation and element distortion problems in grid-based methods may not arise. The nodal connectivity is generated as part of the computation and can change with time, so it can easily deal with the problems of large deformation [5, 6]. Most of meshless methods have been originally introduced originally for crack propagation and problems of blast [7, 8]

## 1.2 Meshless methods

Due to their flexibility and the non-use of classical mesh, meshless (meshfree) methods have attracted many researchers. Numerous meshless methods have been proposed in the last few decades. Based on the form of PDEs used in the computation process, meshless methods can be classified into three distinct groups:

- *Methods based on strong formulation*

To approximate the strong-form of PDEs using meshless methods, the PDEs are usually discretized at points by some forms of collocation, such as the Smoothed Particle Hydrodynamics (SPH) method [9, 10], the Finite Points Method [11] and the Meshfree Collocation Method [12]. The PDEs of strong-form are discretized

straightforwardly without the need of the variational formulation, and hence no numerical integration is required. The resulting discretized equations are simple and fast to implement, and the methods are truly meshfree. However, they are often unstable and less accurate, especially for the case of non-uniform nodal distribution or the case of irregular computation domains.

- *Methods based on weak formulation*

In the weak-form-based method, the PDEs of a problem are first converted into integral equations, thus the field variables require only half order continuity than those using the strong formulation. Integral operation can regularize the solution and make meshless methods based on weak formulation more stable and accurate. Although very accurate in solving numerous different engineering problems, this type of meshless method is known to not be "truly" meshfree, since they still require a background cells (FE mesh) for the integral operation of the weak forms.

This family of meshless methods is still under an active investigation from researchers since the early 1990s. Typically it includes the Diffuse Element Method (DEM) [13] generated by Moving Least Squares (MLS) methods [14], the Element Free Galerkin (EFG) method [7, 15, 16] based on DEM, the Radial Point Interpolation Method (RPIM) [17] and the Reproducing Kernel Particle Method (RKPM) [18] by improving the SPH approximation to satisfy consistency requirements using correction functions.

To overcome the drawback of necessitating an integration background mesh, the local weak-form methods using the local Petrov-Galerkin weak-form were proposed by Atluri and his colleagues [19], called also Meshless Local Petrov-Galerkin (MLPG) method. Some other typical local weak-form method are Method of Finite Spheres (MFS) [20] developed using the MLPG principle and the hp-cloud method [21]. One has to notice that when the meshless local weak-form methods employ delta function as the weight function they become meshless strong-form methods.

- *Methods based on weak-strong formulations*

This family of methods was firstly developed by GR Liu and Gu [22]. In this approach, both strong-form and local weak-form are used to discretize the same set of PDEs, but different groups of points that carry different types of equations/conditions.

The strong formulation is used for all the internal nodes and the nodes on the essential boundaries. The local weak form is used only for nodes near the boundaries with derivative boundary conditions which are difficult to handle by collocation method. Less background cells are used for the integration compared to the weak-form methods which makes this method more stable and efficient.

### 1.3 SPH method and its applications

Smoothed Particle Hydrodynamics (SPH) method is one of earliest meshless methods, which was invented for the modeling of astrophysical problems [9,10]. In the SPH method, the system state is represented by a finite number of discrete particles and each particle possesses a set of field variables such as mass, position, displacement, momentum, temperature, *etc.* The particle can be a discrete physical object like a star or a part of the continuum problem domain like the volume or the area.

SPH method is a truly particle method which uses only the particles distribution as a computational basis for the field variable approximation without any kind of background mesh. This makes the method well-adapted for the treatment of problems involving very large deformations.

The SPH particles are not only used as interpolation points, but also represent material properties and move accordingly to the internal and external forces. Therefore, the time history of all the field variables at a material particle can be easily tracked and obtained which can be described as Lagrangian nature.

SPH method is based on a strong formulation of the governing equations which are directly discretized. However the weak form operation is also adopted to replace the derivative of a field with a numerical integral representation of the state variables by the use of smoothing (weight/shape) functions [23]. Indeed, the integral formulation reduces the requirement on the consistency order of the approximated field function, therefore the smoothing function will allow obtaining a higher accuracy of solution.

The "truly" meshless particles, Lagrangian and strong-form-based SPH method is easy for programming and numerical implementation. It has drawn a lot of attention of the scientific community to improve its stability and accuracy, which will be detailed in Chapter 2. Furthermore, it has been applied into a wide range of problems.

In 1977, Lucy [9], Gingold and Monaghan [10] firstly create the so-called Smoothed Particle



Hydrodynamics (SPH) method, to solve astrophysical problems in three-dimensional open space. In such problems, the real physical system is always discrete and the SPH method consolidates astrophysical particles into a quasi-continuum media. The collective movement of these discrete particles at a large scale is similar to a fluid or a gas flow. Hence, the equations of the classical Newtonian hydrodynamics governing the fluid flow are adopted in the SPH method to describe the particle movement. Nowadays, the SPH method is being widely used in the astrophysics, such as formation of galaxies [24], single or multiple detonations in white dwarfs [25] and even the evolution of the universe [26].

The original SPH method was based on probabilistic principle and statistical techniques. The algorithm did not conserve linear and angular momentum. However, they could give reasonably good results for many astrophysical phenomena. The nature of the non-conservation of linear and angular momentum in the original SPH algorithm was studied by Gingold and Monaghan [27] using different kernels to reproduce known densities. They proposed new kernel estimates to ensure the conservation of both energy and momentum on the basis of the even smoothing function. Hu and Adams [28] also invented an angular-momentum conservative SPH algorithm using viscous force for incompressible viscous flows, which was initially based on empirical findings and then was improved by a more theoretical derivation.

Few years later the SPH method was modified, to be a deterministic meshfree particle method which directly treats the governing system of nonlinear equations based on physical laws. In the last three decades, the SPH method has been widely extended to solve continuum mechanics problems.

Computational Fluid Dynamics became quickly the most active application field of the SPH method, although it was invented and still used for astrophysical problems. A parallel pore-scale numerical model based on SPH was proposed for the simulation of quasi-incompressible two-dimensional flow through porous media [29]. Experimental work and SPH simulations were performed for the study of the gravity current traveling down a ramp in a tank with a layer of fresh water above a layer of salty water [30], numerical results show a good agreement with the experience data. In 1995, Monagan and Kocharyan [31] extended the general SPH formulation to deal with two phase flow of a dusty gas. Then Cleary [32] developed the SPH method to describe accurately the conductive and convective heat transfer for a sequence of idealized benchmark problems. Several unsteady heat conduction problems governed by second-order derivatives were investigated using a

Corrective Smoothed Particle Method (CSPM) [33]. Colagrossi and Landrini [34] treated two-dimensional interfacial flows for low density ratios, like dam-break problem. Alia and Souli [35] used the Eulerian multi-material formulation to simulate high pressure wave propagation in the air explosion.

Since its creation, the SPH method did not use any kind of mesh, which makes the method particularly suitable for the simulation of large deformation, and it continuously attracts attention in computational solid mechanics. For instance, plane strain forging process was simulated using constant Corrected Smoothed Particles Hydrodynamics (CSPH) [36], in which the metals were regarded as non-Newtonian fluids. High pressure die casting simulations were carried out using 3D SPH program [37]. Gray *et al.* [38] successfully investigated the linear and nonlinear oscillations of a plate using an artificial stress which aimed to remove the tensile instability.

An important application area is the hyper velocity impact (HVI), since shock waves propagate through the colliding bodies which behave like fluids [39]. The oblique impact and fracture of multilayered panels by tungsten cubes has been simulated by SPH [40]. The SPH method including different formula to describe the artificial viscosity was studied in the hyper velocity impact of metallic projectiles on thin metallic plates [41]. Benz and Asphaug [42] demonstrated the capabilities of the SPH model by examining the propagation of cracks in a simple tensile rod.

The SPH method is also widely used for the modeling of explosion phenomena. Sweigle and Attaway [43] have studied the feasibility of the SPH method used for the analysis of various types of underwater explosion problems involving fluid-structure and shock-structure interactions. SPH was applied also for the simulation of high explosions which consist in a detonation and a dispersion process [44].

More details on the various applications of the SPH method and its developments can be found in the following papers [45–49] and the books [50, 51].

## 1.4 Motivations and outline of the thesis

### 1.4.1 Motivations

SPH method is one of the earliest meshless method and was initially used for the investigation of astrophysical phenomenon. It possesses the special features of meshfree, Lagrangian and particle nature, and hence it is expected to solve the problems involving

large deformation. Nowadays, the SPH method has been modified and its accuracy and stability are highly improved. The focus of its various applications has been transferred to Computational Fluid Dynamics by discretizing the Navier-Stokes equations. Such application includes incompressible flows with solid boundaries [29], free surface flows [52], and heat transfer and mass flow [32], *etc.*

Under extreme loading conditions, such as hyper-velocity impact, explosion and metal forming, solids are subjected to large deformations and they behave almost like fluids. The conventional SPH method for fluid dynamics can be used in computational solid mechanics by incorporating treatment of material strength. Many researchers have investigated impact and explosion using SPH method, such as Taylor bar impacting on a solid wall [53], bird strike impacting on an aircraft wing [54], projectile impact and penetration [55], extrusion and forging processes [56]. In these investigations, the hydrostatic pressure is generally calculated as a function of density changed by an "equation of state", and the deviatoric shear stress is typically purely viscous and depends on the fluid models.

The classical SPH method has been developed and successfully applied in structural mechanics as well as in the modeling of forming processes, in metal cutting and in impact on a fuel tank using only 3D continuum approach [41, 57]. However modeling shell-like structures using a 3D continuum approach is very time-consuming, because several particles need to be placed in the thickness direction. It has been shown [57] that a minimum of three particles through the plate thickness is needed to ensure a good quality of results. Hence, simple and time-saving meshless shell formulation with a single layer of particles on the mid-plane has attracted numbers of researchers. For instance, Krysl and Belytschko [58] combined the Kirchhoff plate theory with EFG method for solving structural problems involving plates, in which a congruent background cells are necessary to integrate the global weak forms. Li *et al.* [59] adopted RKPM to simulate large deformation of thin shell structures using the window function to construct highly smoothed shape functions. The MLPG method is successfully used for solving Mindlin shells by using a local weak form [60].

The research investigation presented in the present thesis concerns the development of the SPH method for the elastodynamic nonlinear analysis of shell structures, including isotropic and composite multilayered structures. This goal can be reached by deriving the discretized governing equations of solid with SPH particles, as well as the shell concept for describing the structure kinematics. In this novel algorithm called *Shell-based SPH method*, only the

shell mid-surface is discretized by a unique layer of SPH particles to represent the behavior of the entire shell continuum. The kinematics concept is described using the Reissner-Mindlin theory for isotropic shell or First-Order Shear Deformation Theory (FSDT) for laminated structures which takes into account the transverse shear stress. The plane stress condition is assumed in the plane tangent to the mid-surface. Instead of the equation of state used in the conventional SPH method for solid, material constitutive models is adopted to link the stresses and strains tensors.

Nevertheless, the stability and accuracy of the SPH method for solids are affected severely by the inherent drawbacks of the conventional SPH method. Many treatment methods have been proposed in last two decades and will be thoroughly discussed and an appropriate technique is selected in service for the shell-based SPH method.

### 1.4.2 Outline of the thesis

The PhD thesis manuscript is organized into five chapters:

- Chapter 1 presents a general introduction including a literature overview of the SPH method. An outline of the thesis manuscript is given at the end of this chapter.
- In Chapter 2, the principles of SPH method are detailed, together with its inherent drawbacks. After handling these problems, the SPH strong formulation using the Total Lagrangian (TL) approach for solids is established.
- Then, the extension of the SPH method involving only one layer of particles for the modeling of shell structures is developed in Chapter 3.
- In Chapter 4, the constitutive material laws applied for multilayered composite structures are presented, these structures are then, modeled by the shell-based SPH method by combining the first-order shear deformation theory.
- In Chapter 5 is presented the modeling of low velocity impact on laminated composite shells by rigid projectiles. The contact force between the laminate and impactor is pre-determined thanks to the Hertzian contact law. Tsai-Wu failure criterion and maximum stress criterion are used to determine the damage initiation of matrix crack and fiber fracture.

Through Chapters 2-5, are exposed numerous applications including isotropic and

composite shell structures under dynamic loading, to demonstrate the feasibility of the proposed shell-based SPH method.

- The concluding remarks and outlooks are drawn.



---

## *SPH formulation for 2D solids*

---

In this chapter, an efficient SPH formulation adapted for geometrically linear and nonlinear analysis of two-dimensional solids is developed. Firstly, fundamental solid mechanics is recalled. Then the classical SPH approach for a field variable and its derivatives using a smoothing function are detailed, as well as some variants of SPH formulations for discretizing the balance equations of continuum. Two intrinsic drawbacks of the classical SPH method involving the consistency and stability are illustrated and many handling methods are proposed to alleviate these problems. Finally a strategy combining the Corrective Smoothed Particle Method (CSPM), the Total Lagrangian (TL) formulation based on the use of artificial viscosity, is employed in the present investigation. The performance of the proposed SPH method will be demonstrated by solving a variety of numerical examples using an Explicit Dynamics scheme for the time integration of the PDEs. Comparison of the obtained results with the one from literature and FE simulation using ABAQUS<sup>®</sup> (Explicit/Standard) code will show the efficiency of the proposed SPH method.

### 2.1 Brief recall of basic continuum mechanics relations

The aim of this section is to briefly recall some basic fundamentals of solid mechanics which will be used later in the following chapters.

#### 2.1.1 Kinematics

At time  $t = 0$ , the continuum is regarded as an assembly of material particles and occupies an initial configuration  $C_0$  with a volume  $V_0$  enclosed by a surface  $S_0$  as indicated in Figure 2.1. After deformation, at time  $t$ , these points transform to another configuration  $C$  which has a volume  $V$  and a surface  $S$ . During this transformation (Figure 2.1), a point  $P_0$  in  $C_0$  moves from its initial position  $\mathbf{X}$  to the current position  $P$  referenced with final position

vector  $\mathbf{x}$ . The motion of the particle  $P_0$  can be expressed as,

$$\mathbf{x} = \mathbf{x}(\mathbf{X}, t) \quad (2.1)$$

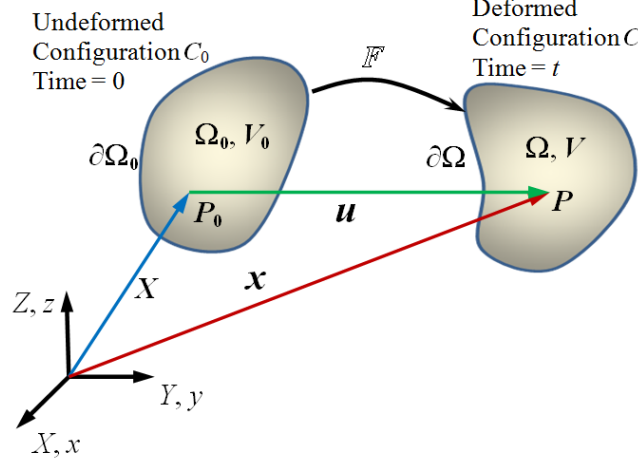


Figure 2.1: Kinematics of a continuum body

In the deformation process, the difference between the initial and the current positions constitute the displacement field  $\mathbf{u}$ ,

$$\mathbf{u} = \mathbf{x} - \mathbf{X} \quad (2.2)$$

A key quantity in finite deformation analysis is the deformation gradient tensor  $\mathbb{F}$ , which is involved in all equations relating quantities before and after deformation.  $\mathbb{F}$  is said to be a two-point second order tensor defined by

$$\mathbb{F} = \frac{\partial \mathbf{x}}{\partial \mathbf{X}} = \mathbb{I} + \mathbb{L} \quad (2.3)$$

with  $\mathbb{I}$  unit tensor and  $\mathbb{L} = \frac{\partial \mathbf{u}}{\partial \mathbf{X}}$  the displacement gradient tensor. The determinant of the deformation gradient  $J = \det(\mathbb{F})$  is known as the volume ratio or Jacobian determinant, *i.e.*  $V = J(\mathbf{X}, t) V_0$ .

The Green-Lagrangian strain tensor  $\mathbb{E}$  associated with the initial configuration can be obtained using

$$2\mathbb{E} = \mathbb{F}^T \mathbb{F} - \mathbb{I} = \mathbb{L}^T + \mathbb{L} + \mathbb{L}^T \mathbb{L} \quad (2.4)$$

The strain tensor described in the current configuration is known as Euler-Almansi strain tensor  $\boldsymbol{\varepsilon}$ , which can be obtained from  $\mathbb{E}$  thanks to the use of  $\mathbb{F}$



$$\boldsymbol{\varepsilon} = \mathbb{F}^{-T} \mathbb{E} \mathbb{F}^{-1} \quad (2.5)$$

Following the engineering notation, the second order strain tensor  $\boldsymbol{\varepsilon}$  can be written in a vector form as

$$\boldsymbol{\varepsilon}^T = \{\varepsilon_{11} \quad \varepsilon_{22} \quad \varepsilon_{33} \quad 2\varepsilon_{12} \quad 2\varepsilon_{23} \quad 2\varepsilon_{31}\} \quad (2.6)$$

### 2.1.2 Constitutive relations

In the scope of elastic deformation, the generalized Hooke's law is often adopted to give the relationship between the stress and the strain components. For an isotropic material, it is given as,

$$\sigma_{ij} = \frac{E}{1+\nu} \left( \varepsilon_{ij} + \frac{\nu}{1-2\nu} \varepsilon_{kk} \delta_{ij} \right) \quad (2.7)$$

where  $E$  is the Young's modulus,  $\nu$  the Poisson's ratio,  $\delta_{ij}$  the Kronecker symbol and  $\varepsilon_{kk}$  is the shorthand notation of the strain tensor trace.

If the structure thickness in direction 3 is very small compared to the two other dimensions 1, 2, the stresses in direction 3 are assumed to vanish, yielding to the so-called plane stress condition. Thus, the stress-strain relationship changes to be

$$\begin{Bmatrix} \sigma_{11} \\ \sigma_{22} \\ \sigma_{12} \end{Bmatrix} = \frac{E}{1-\nu^2} \begin{bmatrix} 1 & \nu & 0 \\ \nu & 1 & 0 \\ 0 & 0 & (1-\nu)/2 \end{bmatrix} \begin{Bmatrix} \varepsilon_{11} \\ \varepsilon_{22} \\ 2\varepsilon_{12} \end{Bmatrix} \quad (2.8)$$

Another case is the plane strain condition, which occurs when the thickness in direction 3 is very large compared to the other dimensions 1, 2. In this situation, the strain components in direction 3 are zero, which allows the following relationship

$$\begin{Bmatrix} \sigma_{11} \\ \sigma_{22} \\ \sigma_{12} \end{Bmatrix} = \frac{E}{(1+\nu)(1-2\nu)} \begin{bmatrix} 1-\nu & \nu & 0 \\ \nu & 1-\nu & 0 \\ 0 & 0 & (1-2\nu)/2 \end{bmatrix} \begin{Bmatrix} \varepsilon_{11} \\ \varepsilon_{22} \\ 2\varepsilon_{12} \end{Bmatrix} \quad (2.9)$$

### 2.1.3 Principle of mass conservation

During the process of deformation and motion, there are neither mass sources nor mass sinks, so that total mass of the body is a conserved quantity, *i.e.*  $M = M_0$ . Considering the mass is distributed continuously in the region  $\Omega$ , then the local (pointwise) mass  $dm$

can be measured by the mass density  $\rho$  and the volume  $dV$  it occupies, *i.e.*  $dM = \rho dV$ .

The conservation of mass in the global (integral) form can be expressed as

$$M_0 = \int_{\Omega_0} \rho_0(\mathbf{X}) dV_0 = M = \int_{\Omega} \rho(\mathbf{x}, t) dV \quad (2.10)$$

or in the rate form as

$$\frac{dM}{dt} = \frac{d}{dt} \int_{\Omega} \rho(\mathbf{x}, t) dV = 0 \quad (2.11)$$

in which  $dV_0$  and  $dV$  are the standard infinitesimal volumes defined in the reference and current configurations, respectively.

Since the relation  $dV = JdV_0$ , we can get the local form of the mass conservation equation at each point,

$$\rho_0(\mathbf{X}) = J(\mathbf{X}, t)\rho(\mathbf{x}, t) \quad \text{or} \quad \dot{\rho}(\mathbf{x}, t) = -\rho(\mathbf{x}, t) \operatorname{div} \mathbf{v}(\mathbf{x}, t) \quad (2.12)$$

Therefore the continuity condition in the spatial description can be written as

$$\frac{\partial \rho(\mathbf{x}, t)}{\partial t} = -\operatorname{div} [\rho(\mathbf{x}, t) \mathbf{v}(\mathbf{x}, t)] \quad (2.13)$$

where the over-dot notation signifies the material time derivative and  $\operatorname{div}(\cdot)$  is the divergence operator with respect to the spatial coordinates.

#### 2.1.4 Principle of conservation of linear momentum

In dynamics, the equilibrium is stated as the rate of the linear momentum to be equal to the resultant force  $\mathbf{F}$  of all actions on a solid in movement. The resultant force  $\mathbf{F}$  includes the traction  $\mathbf{t} = \mathbf{t}(\mathbf{x}, t, \mathbf{n})$  acting on the boundary surface and the body force  $\mathbf{b} = \mathbf{b}(\mathbf{x}, t)$ , as illustrated in Figure 2.2. The unit vector  $\mathbf{n}$  is the outward normal to an infinitesimal surface  $dS$  on the region boundary  $\partial\Omega$ . The global form of balance equation of linear momentum can be given in the spatial description as

$$\frac{d}{dt} \int_{\Omega} \rho \mathbf{v} dV = \mathbf{F} = \int_{\partial\Omega} \mathbf{t} dS + \int_{\Omega} \mathbf{b} dV \quad (2.14)$$

By virtue of Cauchy's stress theorem  $\mathbf{t} = \mathbf{t}(\mathbf{x}, t) = \boldsymbol{\sigma}(\mathbf{x}, t) \mathbf{n}$  and by using divergence theorem which converts the surface integral into a volume integral, we find that

$$\int_{\partial\Omega} \mathbf{t} dS = \int_{\partial\Omega} \boldsymbol{\sigma} \mathbf{n} dS = \int_{\Omega} \operatorname{div} \boldsymbol{\sigma}(\mathbf{x}, t) dV \quad (2.15)$$

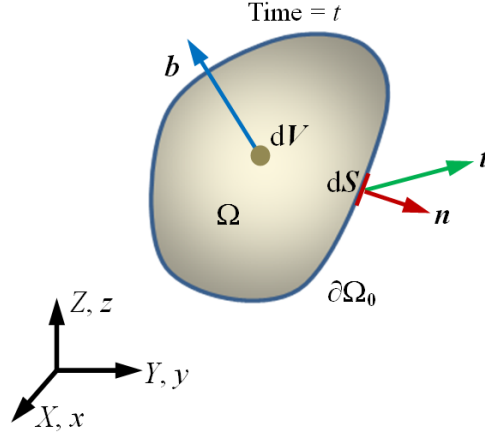


Figure 2.2: Continuum of forces acting on the current configuration.

Substituting this result into the equation of conservation of linear momentum, one can get

$$\int_{\Omega} \rho \dot{\mathbf{v}} dV = \int_{\Omega} (\operatorname{div} \boldsymbol{\sigma} + \mathbf{b}) dV \quad (2.16)$$

or the local form

$$\rho \dot{\mathbf{v}} = \operatorname{div} \boldsymbol{\sigma} + \mathbf{b} \quad (2.17)$$

where the material time derivative of  $\mathbf{v}$  is

$$\dot{\mathbf{v}} = \frac{\partial \mathbf{v}}{\partial t} + (\operatorname{grad} \mathbf{v}) \mathbf{v} \quad (2.18)$$

In the material description, the linear momentum conservation equation may be written in the local form

$$\rho_0 \dot{\mathbf{V}} = \operatorname{Div} \mathbf{P} + \mathbf{b}_0 \quad (2.19)$$

in which  $\mathbf{P} = J \boldsymbol{\sigma} \mathbb{F}^{-T}$  is the first Piola-Kirchhoff stress tensor and  $\mathbf{b}_0 = J \mathbf{b}$  is the body force per unit initial volume. Note that  $\operatorname{Div}(\cdot)$  is the divergence operator with respect to the material coordinates.

### 2.1.5 Principle of conservation of angular momentum

The rate of the angular momentum about any fixed point  $\mathbf{x}_0$  is equal to the resultant moment  $\mathbf{M}$  about that point. We define a position vector  $\mathbf{r}$  from the material point  $\mathbf{x}$  to the fixed point  $\mathbf{x}_0$  ( $\mathbf{r} = \mathbf{x} - \mathbf{x}_0$ ). So the conservation equation of angular momentum can be described in the global form using the Equation (2.14)

$$\frac{d}{dt} \int_{\Omega} \mathbf{r} \times \rho \mathbf{v} dV = \mathbf{r} \times \mathbf{F} = \int_{\partial \Omega} \mathbf{r} \times \mathbf{t} dS + \int_{\Omega} \mathbf{r} \times \mathbf{b} dV \quad (2.20)$$

Since  $\mathbf{t} = \mathbf{t}(\mathbf{x}, t) = \boldsymbol{\sigma}(\mathbf{x}, t) \mathbf{n}$ , we have

$$\int_{\partial\Omega} \mathbf{r} \times \mathbf{t} dS = \int_{\partial\Omega} \mathbf{r} \times \boldsymbol{\sigma} \mathbf{n} dS = \int_{\Omega} (\mathbf{r} \times \operatorname{div} \boldsymbol{\sigma} + \mathcal{E} : \boldsymbol{\sigma}^T) dV \quad (2.21)$$

where  $\mathcal{E}$  is third-order alternating (permutation) tensor.

Rearranging terms in Equation (2.20) to take into account the translational equilibrium Equation (2.19) and noting that the resulting equation is valid for any enclosed region of the body gives,

$$\mathcal{E} : \boldsymbol{\sigma}^T = \begin{bmatrix} \sigma_{32} - \sigma_{23} \\ \sigma_{13} - \sigma_{31} \\ \sigma_{21} - \sigma_{12} \end{bmatrix} = \mathbf{0} \quad (2.22)$$

which clearly implies the symmetry of the Cauchy stress tensor  $\boldsymbol{\sigma}$ . That means when and only when the Cauchy stress tensor is symmetric, the angular momentum quality is conserved.

### 2.1.6 Principle of conservation of energy

The balance of mechanical energy states that the rate of change of the kinetic energy  $\mathcal{K}(t)$  is equal to the balance between the internal power  $\mathcal{P}_{int}(t)$  and external power  $\mathcal{P}_{ext}(t)$ . The global form of conservation of energy can be written as

$$\frac{d}{dt} \mathcal{K}(t) = \mathcal{P}_{ext}(t) - \mathcal{P}_{int}(t) \quad (2.23)$$

with

$$\mathcal{P}_{ext}(t) = \int_{\partial\Omega} \mathbf{t} \cdot \mathbf{v} dS + \int_{\Omega} \mathbf{b} \cdot \mathbf{v} dV \quad (2.24)$$

$$\mathcal{K}(t) = \frac{1}{2} \int_{\Omega} \rho \mathbf{v} \cdot \mathbf{v} dV \quad (2.25)$$

and

$$\mathcal{P}_{int}(t) = \int_{\Omega} \boldsymbol{\sigma} : \nabla \mathbf{v} dV \quad (2.26)$$

where  $\nabla(\cdot)$  notation means the gradient operator.

## 2.2 SPH foundation

### 2.2.1 Approximation of a field variable

In the SPH method, the continuum is discretized into a finite number of particles which possess a set of physical properties. The field variables at each particle such as displacement, density, velocity and stresses, can be approximated using the corresponding quantities of the neighboring particles. The basis of the SPH method is built on the principle that a variable  $u = u(\mathbf{x})$  at a point with a position vector  $\mathbf{x}$  can be exactly reproduced by the use of the Dirac delta function  $\delta$ ,

$$u(\mathbf{x}) = \int_{\Omega} u(\mathbf{x}') \delta(\mathbf{x} - \mathbf{x}') d\Omega_{\mathbf{x}'} \quad (2.27)$$

in which the delta function is defined by

$$\delta(\mathbf{x} - \mathbf{x}') = \begin{cases} 1, & \mathbf{x} = \mathbf{x}' \\ 0, & \mathbf{x} \neq \mathbf{x}' \end{cases} \quad (2.28)$$

However, the Dirac delta function is impossible to be used in its current form for either interpolation or a collocation process, because it is not smooth, continuous and differentiable. To remedy this pathology, a so-called smoothing (or kernel) function  $W(\mathbf{x} - \mathbf{x}', h)$  is designed to keep the delta function property and used to replace the delta function itself. The parameter  $h$  is noted as smoothing length which defines the influence or support area of the smoothing function  $W$ . Therefore, the identical equation (2.27) becomes to a integral representation form

$$u(\mathbf{x}) \approx \int_{\Omega} u(\mathbf{x}') W(\mathbf{x} - \mathbf{x}', h) d\Omega_{\mathbf{x}'} \quad (2.29)$$

In the following text, the notation  $\approx$  is replaced by  $=$  if there is no confusion taken place. With the aid of the quantities of all particles in the compact support domain (see Figure 2.3), the continuous integral representation (kernel representation/estimate) of the field  $u(\mathbf{x})$  can be converted into a discretized form of summation (particle representation/estimate), given by

$$u_i = u(\mathbf{x}_i) = \sum_{j=1}^{N_j} u(\mathbf{x}_j) W(\mathbf{x}_i - \mathbf{x}_j, h) V_j = \sum_{j=1}^{N_j} u_j W_{ij} V_j \quad (2.30)$$

with  $i$  the point where the field variable is approximated and  $j$  is the neighboring point in the support domain of  $i$ .  $N_j$  and  $V_j$  are the total number and the volume of point  $j$  respectively.

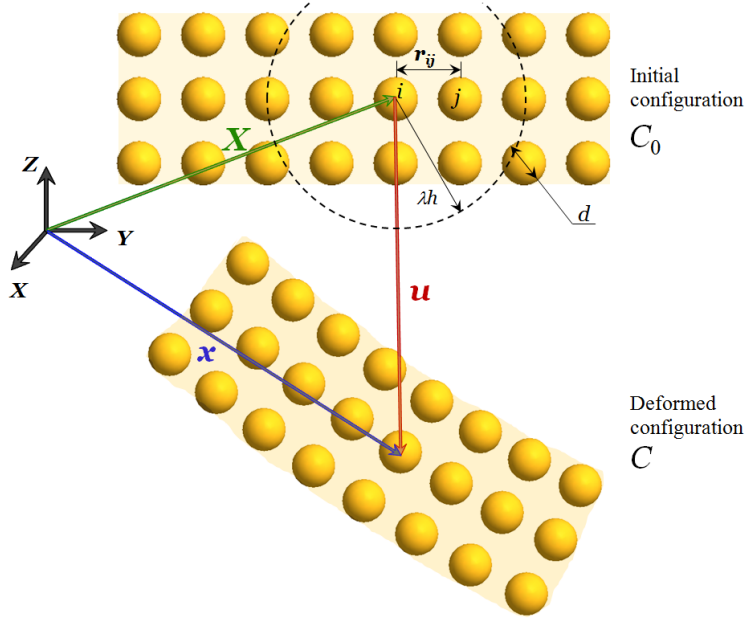


Figure 2.3: Modeling of a 2D structure using the SPH discretization.

### 2.2.2 Smoothing function

In view of the above deriving process of a field variable, the smoothing function represents a significant ingredient of the SPH method. The smoothing (kernel) function determines the interaction of two neighboring points, confines the size of the support domain of a particle rather than the whole region and hence improves the computational efficiency. It also can influence the accuracy and stability property of the SPH simulation [61]. Therefore, the choice of an appropriate smoothing function is critical to build an efficient and accurate SPH approximation of the problem solution. Generally, it is required for the smoothing function, to satisfy several conditions [50].

At first the smoothing function should have a compact support, which implies that  $W = 0$  when  $|\mathbf{x} - \mathbf{x}'| \geq \lambda h$  with a constant  $\lambda$  specifying the non-zero region of  $W$ . The smoothing function has to satisfy also the normalization condition

$$\int_{\Omega} W(\mathbf{x} - \mathbf{x}', h) d\Omega_{\mathbf{x}'} = 1 \quad (2.31)$$

so that it can ensure the zero-th order consistency of the integral representation of a field variable. The third condition is the Dirac delta function property

$$\lim_{h \rightarrow 0} W(\mathbf{x} - \mathbf{x}', h) = \delta(\mathbf{x} - \mathbf{x}') \quad (2.32)$$

which allows the approximated value approaches the function value when smoothing length tends to zero ( $\mathbf{x}' \rightarrow \mathbf{x}$ ).

In addition to the above conditions, the smoothing function should also be positive (physical meaning), even and monotonically decreasing away from the origin, which signify that particles of same distance give the same effects and further particle has smaller influence on the particle under consideration.

There exist numerous smoothing functions proposed in the literature, such as the bell-shaped function by Lucy in his original paper [9], the Gaussian function by Gingold and Monaghan [10], the cubic B-spline function Monaghan and Lattanzio [62] and some higher order functions by Morris [61].

In the present work, we adopt the most frequently used cubic B-spline function, in which the constant  $\lambda = 2$

$$W(\mathbf{x}_i - \mathbf{x}_j, h) = \alpha_d \times \begin{cases} \frac{2}{3} - s^2 + \frac{1}{2} s^3 & \text{if } 0 \leq s < 1 \\ \frac{1}{6} (2 - s)^3 & \text{if } 1 \leq s < 2 \\ 0 & \text{if } s \geq 2 \end{cases} \quad (2.33)$$

where  $\alpha_d$  is a scaling factor to assure the normalization condition and takes  $1/h$ ,  $15/7\pi h^2$  and  $3/2\pi h^3$  in one-, two- and three-dimensional space respectively.  $s = r_{ij}/h$  and  $r_{ij} = |\mathbf{x}_i - \mathbf{x}_j|$  is the distance between the points  $i$  and  $j$ . This smoothing function is plotted in Figure 2.4 together with its first-order and second-order derivatives.

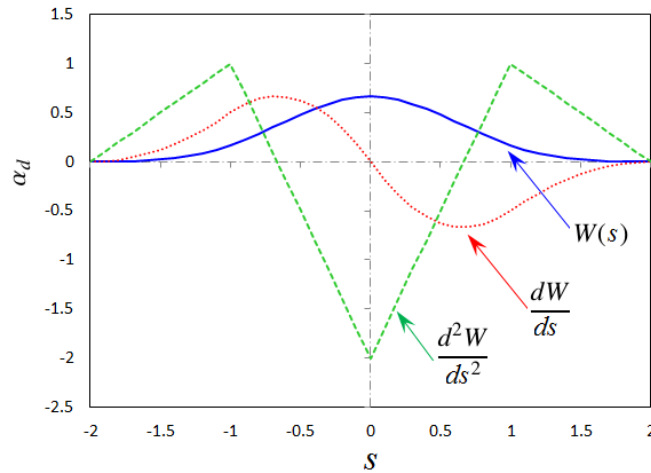


Figure 2.4: Kernel function used in two-dimensional space.

### 2.2.3 Approximation of field derivatives

To obtain the approximation form of the derivatives of a field variable, one can directly replace the field variable  $u(\mathbf{x})$  in the Equation (2.29) with its gradient  $\nabla u(\mathbf{x})$

$$\nabla u(\mathbf{x}) = \int_{\Omega} \nabla u(\mathbf{x}') W(\mathbf{x} - \mathbf{x}', h) d\Omega_{\mathbf{x}'} \quad (2.34)$$

By virtue of integration by parts and the divergence theorem, we can obtain

$$\begin{aligned} \nabla u(\mathbf{x}) &= \int_{\Omega} \nabla u(\mathbf{x}') W(\mathbf{x} - \mathbf{x}', h) d\Omega_{\mathbf{x}'} \\ &= \int_{\Omega} \nabla [u(\mathbf{x}') W(\mathbf{x} - \mathbf{x}', h)] d\Omega_{\mathbf{x}'} - \int_{\Omega} u(\mathbf{x}') \nabla W(\mathbf{x} - \mathbf{x}', h) d\Omega_{\mathbf{x}'} \\ &= \int_{\partial\Omega} u(\mathbf{x}') W(\mathbf{x} - \mathbf{x}', h) \mathbf{n} dS_{\mathbf{x}'} - \int_{\Omega} u(\mathbf{x}') \nabla W(\mathbf{x} - \mathbf{x}', h) d\Omega_{\mathbf{x}'} \end{aligned} \quad (2.35)$$

where  $\mathbf{n}$  is the unit vector normal to the element surface  $dS$ .

If the point  $\mathbf{x}$  is enough far away from the boundary, the support domain of its smoothing function is entirely interior of the region  $\Omega$ . Hence the smoothing function vanishes at the boundaries of the support domain due to its compact support character. The above function can be rewritten as,

$$\nabla u(\mathbf{x}) = - \int_{\Omega} u(\mathbf{x}') \nabla W(\mathbf{x} - \mathbf{x}', h) d\Omega_{\mathbf{x}'} \quad (2.36)$$

Noting that this formulation is not satisfied when the point is near or located at the boundary because of the truncation of the compact support domain by the boundary.

The corresponding discrete approximation form using the neighboring particles, is

$$\nabla u_i = - \sum_{j=1}^{N_j} u_j \nabla_j W(\mathbf{x}_i - \mathbf{x}_j, h) V_j = \sum_{j=1}^{N_j} u_j \nabla W_{ij} V_j \quad (2.37)$$

where  $\nabla W_{ij}$  is a simplified form of  $\nabla_i W(\mathbf{x}_i - \mathbf{x}_j, h)$  and  $\nabla_i W(\mathbf{x}_i - \mathbf{x}_j, h) = \frac{\mathbf{x}_i - \mathbf{x}_j}{|\mathbf{x}_i - \mathbf{x}_j|} \frac{\partial W}{\partial r}(\mathbf{x}_i - \mathbf{x}_j, h) = -\nabla_j W(\mathbf{x}_i - \mathbf{x}_j, h)$ .

## 2.3 SPH discretization of the equilibrium equations of solids

In solid mechanics, the equations governing the conservation of mass and linear momentum mentioned in Section 1 can be discretized using the SPH method, leading for each particle  $i$  to

$$\frac{d\rho_i}{dt} = -\rho_i \operatorname{div} \mathbf{v}_i = -\rho_i \sum_{j=1}^{N_j} \mathbf{v}_j \nabla W_{ij} V_j \quad (2.38)$$



$$\frac{d\mathbf{v}_i}{dt} = \frac{1}{\rho_i} \operatorname{div} \boldsymbol{\sigma}_i = \frac{1}{\rho_i} \sum_{j=1}^{N_j} \boldsymbol{\sigma}_j \nabla W_{ij} V_j \quad (2.39)$$

Considering the even property of the smoothing function, its gradients should be odd and we have

$$\sum_{j=1}^{N_j} \nabla W_{ij} V_j = 0 \quad (2.40)$$

Multiplying above equation with  $\rho_i \mathbf{v}_i$  and adding to the right hand side (RHS) of Equation (2.38), we can get a popular antisymmetrized form [63] for the mass conservation equation

$$\frac{d\rho_i}{dt} = -\rho_i \sum_{j=1}^{N_j} \mathbf{v}_{ji} \nabla W_{ij} V_j \quad (2.41)$$

where  $\mathbf{v}_{ji} = \mathbf{v}_j - \mathbf{v}_i$  is the difference of velocity vector between two neighboring particles  $j$  and  $i$ . This approximation form of mass conservation equation is preferred because the density change is forced to be zero if rigid motion occurs.

For the momentum conservation equation, there exist another widespread symmetrized expression given by [38, 51]

$$\frac{d\mathbf{v}_i}{dt} = \sum_{j=1}^{N_j} \left( \frac{\boldsymbol{\sigma}_i}{\rho_i^2} + \frac{\boldsymbol{\sigma}_j}{\rho_j^2} \right) \nabla W_{ij} \rho_j V_j \quad (2.42)$$

This form will ensure that the force acting on particle  $i$  from particle  $j$  is of the same magnitude as the force applied on particle  $j$  from the particle  $i$ , but the two forces are acting in opposite directions. In other words, it satisfies the Newton's law.

## 2.4 Inconsistency problems and corrective techniques

In the FE method, the degree of consistency can be characterized by the order of the polynomial that can be exactly reproduced by the approximation using the shape functions. The same concept can be used in the SPH method. In fact, the standard SPH approximation is not even of 0-th completeness, *i.e.* constant field and linear gradient can not be exactly reproduced. This is mainly due to the following reasons:

- At first, the inconsistency results from the edge effect. The smoothing function is required to meet the normalization condition,  $\int_{\Omega} W d\Omega = 1$ , *i.e.* the approximation can produce constant field. This is true for the interior particles far away from the boundaries. However, for the particles located on the boundaries or nearby, the

support domain is truncated by the boundary, so that the integral of  $W$  in the insufficient support domain is less than 1. For instance, in 1D geometry, the integral of the smoothing function is equal to  $1/2$  on the two end points. The error of 50% is obnoxious.

For the approximation of the gradients, truncated support domain of the nearby boundary particles also leads the surface integral of the deviates of smoothing function (first term of RHS of Equation (2.35)) not to vanish. Therefore, Equation (2.37) is not always satisfied for constant field function.

- The second reason is the discrepancy between the kernel and particles approximation [50]. When the integral on a domain is discretized into the summation over the neighboring particles, the trapezoidal rule is used. The variant smoothing function in a discretized domain is replaced by a constant value on the centroid. Furthermore, the total volume of the particles in the neighboring region in general is not the same as the one of the compact support domain, which can produce numerical errors, not to mention the irregularly distributed particles. The same observation can be done for the gradient approximation.

Many researchers proposed different methods to restore the consistency of the SPH approximation. The anti-symmetrized [63] and symmetrized forms [38] of the gradient approximation are detailed in the previous section. Libersky and Petschek [64] introduced ghost particles to reflect a symmetrical surface boundary condition. Randles and Libersky [65] proposed a normalization formulation for density and the divergence of the stress tensor. Liu *et al.* gave a general approach to rebuild the smoothing function for restoring particle consistency through reproducing kernel particle method (RKPM) [18, 51, 66]. The reproducing kernel function was developed by multiplying a correction function with the so-called window function (same as the SPH kernel function). Generally, the correction function is expressed by a linear combination of polynomial basis functions. This method can reproduce  $n$ -th order polynomials with  $n$ -th order correction function by expanding the Taylor series for the function in the integral transformation. However, the resulting shape function do not satisfy the Kronecker delta property and can not exactly match the real value at sample points, therefore essential boundary conditions cannot be directly enforced [66]. Special care must be taken because the resultant shape function maybe negative, not symmetric and not monotonically decreasing as the particle distance increases [51].

Some other techniques can restore high order consistency such as Moving Least Square Particle Hydrodynamics (MLSPH) proposed by Dilts [67, 68], Modified SPH (MSPH) and Symmetric SPH (SSPH) proposed by Zhang and Batra [69, 70]. To avoid non-singularity problem, a number of particles should be included in the support domain of the kernel function. The number is required to be no less than the linearly independent monomials used for construction of approximation basis. Like RKPM, Kronecker delta property don't be guaranteed in MLSPH and SSPH.

Chen *et al.* [33, 71] developed a Corrective Smoothed Particle Method (CSPM) by combining the kernel estimates with the Taylor series expansion. They proved that the general problem of particle deficiency was resolved using this algorithm and derivatives of any order could be reproduced, which is essential for the time-dependent boundary value problems. Moreover, it could be suitable for modeling any unsteady boundary value problem with the Dirichlet and/or von Neumann types of boundary conditions

In the following developments, the CSPM will be adopted in this work.

1. Performing Taylor series expansion of a variable  $u(\mathbf{x})$  at point  $i$  with coordinates  $\mathbf{x}_i = (x_{i1}, x_{i2}, x_{i3})$ , gives

$$u = u_i + u_{i,\alpha}(x_\alpha - x_{i\alpha}) + \frac{1}{2}u_{i,\alpha\beta}(x_\alpha - x_{i\alpha})(x_\beta - x_{i\beta}) + \dots \quad \alpha, \beta = 1, 2, 3 \quad (2.43)$$

where  $u_{i,\alpha} = \left. \frac{\partial u}{\partial x_\alpha} \right|_{\mathbf{x}=\mathbf{x}_i}$ ,  $u_{i,\alpha\beta} = \left. \frac{\partial^2 u}{\partial x_\alpha \partial x_\beta} \right|_{\mathbf{x}=\mathbf{x}_i}$  and summation is implied on repeated indices  $\alpha$  and  $\beta$ .

2. By multiplying both sides of (2.43) by the kernel function  $W(\mathbf{x}_i - \mathbf{x}, h)$  and integrating the resulted equation over the domain  $\Omega$ , yields to

$$\begin{aligned} \int_{\Omega} u W d\Omega = & u_i \int_{\Omega} W d\Omega + u_{i,\alpha} \int_{\Omega} (x_\alpha - x_{i\alpha}) W d\Omega \\ & + \frac{1}{2}u_{i,\alpha\beta} \int_{\Omega} (x_\alpha - x_{i\alpha})(x_\beta - x_{i\beta}) W d\Omega + \dots \end{aligned} \quad (2.44)$$

3. By neglecting all the derivative terms, a corrective version of the kernel approximations is then generated

$$u_i = \frac{\int_{\Omega} u W(\mathbf{x}_i - \mathbf{x}, h) d\Omega}{\int_{\Omega} W(\mathbf{x}_i - \mathbf{x}, h) d\Omega} \quad (2.45)$$

and corresponding particle approximation formulation

$$u_i = \frac{\sum_{j=1}^{N_j} u_j W_{ij} V_j}{\sum_{j=1}^{N_j} W_{ij} V_j} \quad (2.46)$$

4. Repeat the above procedure by replacing  $W$  with  $W_\gamma = \frac{\partial W}{\partial x_\gamma}$  and neglecting second-order derivatives and higher, which gives

$$u_{i,\alpha} \int_{\Omega} (x_\alpha - x_{i\alpha}) W_\gamma d\Omega = \int_{\Omega} (u - u_i) W_\gamma d\Omega \quad (2.47)$$

5. The particle approximation of first-order derivatives converted from the above equation are written in a concise notation form as

$$\nabla u_i = \left( \sum_{j=1}^{N_j} (\mathbf{x}_j - \mathbf{x}_i) \otimes \nabla W_{ij} V_j \right)^{-1} \sum_{j=1}^{N_j} (u_j - u_i) \nabla W_{ij} V_j \quad (2.48)$$

6. Using a similar approach, the generalized particle approximation can be derived for any higher-order derivatives.

To explain the efficiency of this corrected version for first-order derivatives, let consider the function  $f = \frac{1}{2} \left( \frac{\partial x}{\partial x} + \frac{\partial y}{\partial y} \right)$  for which the value is unity everywhere. Approximations of this function in a 2D rectangle domain by the classical SPH method and the CSPM are then performed. The distribution of this function is depicted in the Figure 2.5. The values at the corners obtained using the classical SPH method is only 0.43, which represents an awful error of 63%. In the right hand side of Figure 2.5 is represented the solution obtained using the CSPM. This results shows clearly a big improvement in the approximation thanks to the CSPM and the function value is equal to 1 at all particles.

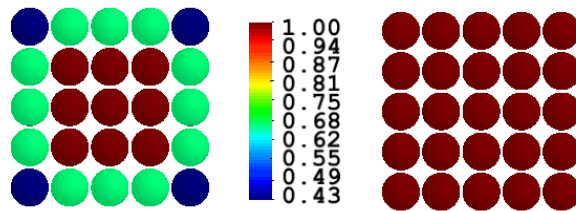


Figure 2.5: Comparison of the performance between the classical SPH method (left) and the CSPM (right).

## 2.5 Artificial viscosity

The artificial viscosity was firstly introduced into the inviscid Euler equations in fluid dynamics in order to treat the shock wave discontinuities [72]. This strong numerical instability can be solved by transferring kinetic energy into heat energy across the shock

wave front, which can be represented by viscous dissipation. Therefore, a dissipative term, called *artificial viscosity* is introduced into the momentum equations.

The term of the artificial viscosity was firstly used by Monaghan and Gingold [73] into the SPH method to simulate the shock. It is given by

$$\Pi_{ij} = \begin{cases} \frac{-\alpha_{\Pi} \bar{c}_{ij} \phi_{ij} + \beta_{\Pi} \phi_{ij}^2}{\bar{\rho}_{ij}} & \mathbf{v}_{ij} \cdot \mathbf{x}_{ij} < 0 \\ 0 & \mathbf{v}_{ij} \cdot \mathbf{x}_{ij} \geq 0 \end{cases} \quad (2.49)$$

where

$$\phi_{ij} = \frac{h_{ij} \mathbf{v}_{ij} \cdot \mathbf{x}_{ij}}{|\mathbf{x}_{ij}|^2 + 0.01 h_{ij}^2}, \quad h_{ij} = \frac{h_i + h_j}{2}, \quad \mathbf{v}_{ij} = \mathbf{v}_i - \mathbf{v}_j, \quad \mathbf{x}_{ij} = \mathbf{x}_i - \mathbf{x}_j \quad (2.50)$$

$$\bar{\rho}_{ij} = \frac{\rho_i + \rho_j}{2}, \quad \bar{c}_{ij} = \frac{c_i + c_j}{2} \quad (2.51)$$

In the above equations,  $\alpha_{\Pi}$  and  $\beta_{\Pi}$  are constant coefficients relative to bulk viscosity and von Neumann-Richtmyer artificial viscosity;  $c$  is the sound velocity in the material; the term  $0.01 h_{ij}^2$  is introduced to prevent the singularities when two particles become too close.

The values of  $\alpha_{\Pi}$  and  $\beta_{\Pi}$  were typically chosen to be 1 and 2 [45].  $\alpha_{\Pi} = \beta_{\Pi} = 2.5$  was proposed for the modeling of solids [5]. In the present investigation,  $\alpha_{\Pi} = 0.2$  and  $\beta_{\Pi} = 0.4$  were tested to be the best combination for isotropic elastic materials. An exception is done for the last application in this chapter (sandwich beam), where the used pair of coefficients are  $\alpha_{\Pi} = 2.5$  and  $\beta_{\Pi} = 0.6$ .

The artificial viscosity provides viscous forces associated to the linear momentum Equation (2.42), thus the numerical instability will be attenuated. The viscous forces are implemented in the normal direction and hence the discretized equilibrium equation is given by

$$\frac{d\mathbf{v}_i}{dt} = \sum_{j=1}^{N_j} \left( \frac{\boldsymbol{\sigma}_i}{\rho_i^2} + \frac{\boldsymbol{\sigma}_j}{\rho_j^2} - \Pi_{ij} \right) \nabla W_{ij} \rho_j V_j \quad (2.52)$$

## 2.6 Extension of the SPH method using the Total Lagrangian Formulation

If the standard SPH method is adopted for the modeling of continua in solid mechanics, using the Updated Lagrangian Formulation (ULF) expressed into the current deformed configuration, it is often accompanied by an artificial unstable motion of particles, which arises when the structure is under tensile stress state [43]. This phenomenon is known as *tensile instability* and can result in particles clumping. Indeed, this instability often occurs

when the product of the stress state and the second derivative of the smoothing function is positive [43].

Different approaches have been proposed to control the tensile instability. For instance, the Conservative Smoothing Approach (CSA) introduced by Swegle *et al.* in 1994 [74] was designed to add stabilizing dissipation into the velocity difference rule. It introduces a smoothing operators in 1D given by

$$\bar{\mathbf{v}}_i = \mathbf{v}_i + \alpha_{cs} \left( \frac{1}{2} (\mathbf{v}_{i-1} + \mathbf{v}_{i+1}) - \mathbf{v}_i \right) \quad 0 < \alpha_{cs} \leq 0.5 \quad (2.53)$$

Balsara [75] also proposed in 1995, a similar spatial filter in three dimensions which was improved later by Randles and Libersky [65] in 1996, which states

$$\bar{\mathbf{v}}_i = \mathbf{v}_i + \alpha_{cs} \left( \frac{\sum_{j \neq i} \mathbf{v}_j W_{ij} A_j}{\sum_{j \neq i} W_{ij} A_j} - \mathbf{v}_i \right) \quad (2.54)$$

This technique is attractive because of its simplicity and time saving. Adams and Wicke [76] showed that if the corrected velocities can be stored and used in subsequent time steps, the viscosity effect may become stronger. They studied a variation of the viscosity when  $\alpha_{cs}$  changes between 0 and 1, and they noticed that the stability increased as  $\alpha_{cs}$  gets closer to 1.

Herein we carry out a numerical application using a 2D cantilever plate to study the influence of the parameter  $\alpha_{cs}$ . The left edge of the plate is clamped and the right free end is subjected to a transverse load  $F = 1750N$  as shown in Figure 2.6. The geometrial and material data of the plate are as follows :  $L = 100mm$ ,  $t = 10mm$ , width  $1mm$ ,  $E = 210GPa$ ,  $\nu = 0.3$ ,  $\rho = 7800kg/m^3$ . The total simulation time is  $10ms$ . Different values of  $\alpha_{cs}$  are used and the evolution of the displacement of point  $C$  are depicted in Figure 2.6.

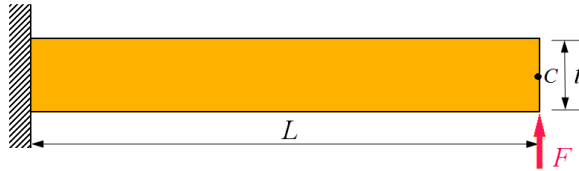


Figure 2.6: Clamped plate under transverse load.

From Figure 2.7, we can remark for small values of  $\alpha_{cs}$  (0 and 0.01) the solution diverges at the beginning of the computation. More the value of  $\alpha_{cs}$  is increased, better the stability

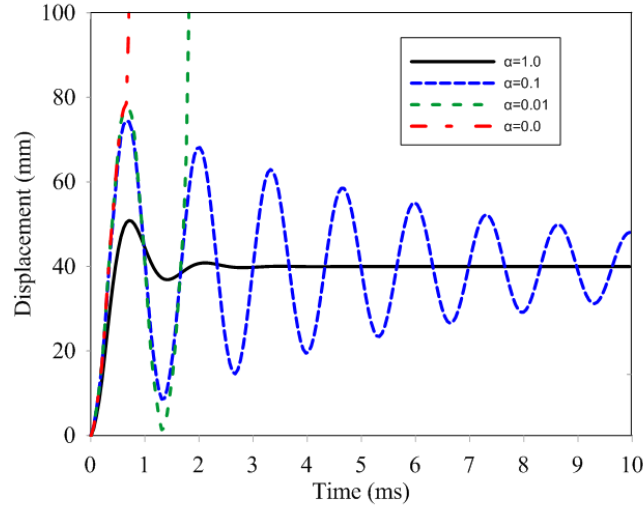


Figure 2.7: Evolution of the plate deflection at point C, in function of time.

of the solution is. However higher values lead to a quicker reduction of the deflection magnitude due to a strong dissipation of the kinematic energy (Figure 2.7).

Another approach has been proposed initially by Monaghan [77] which consists in the use of artificial repulsive forces, unfortunately good results can be obtained only when the discretization is sufficiently fine [77]. A unified stability analysis of meshless methods with Eulerian and Lagrangian kernels has been discussed in details by Belytschko *et al.* in 2000 [78]. The authors showed that the tensile instability, which is inherent in the use of the Eulerian kernel in the spatial coordinates, does not exhibit when Lagrangian kernels are used [78].

In the present investigation the Total Lagrangian SPH Formulation is adopted and the governing elastodynamic equations are reformulated by the TL SPH using a Lagrangian kernel. In this case, the initial geometry of the structure is regarded as the reference configuration and therefore the kernel function is computed just once at the first step and stored. The cumbersome nearest neighboring particles search operation in each time step is no longer needed. The density used in the momentum conservation equation is the initial density, therefore it is not necessary to update the density using Equation (2.41). Time-saving in this formulation compared to the classical Eulerian SPH formulation is remarkable.

Firstly, the deformation gradient tensor is approximated by

$$\mathbb{F} = \frac{\partial \mathbf{x}}{\partial \mathbf{X}} = \sum_{j=1}^{N_j} (\mathbf{x}_j - \mathbf{x}_i) \nabla_0 W_{0ij} V_{0j} \quad (2.55)$$

where  $\nabla_0 W_0$  is the gradient of the Lagrangian kernel function  $W_0$  with respect to the material coordinates.

Then the Green Lagrangian strain is calculated by  $\mathbb{E} = \frac{1}{2}(\mathbb{L} + \mathbb{L}^T + \mathbb{L}^T \mathbb{L})$  and the displacement gradient tensor  $\mathbb{L}$  is estimated by TL SPH formulation

$$\mathbb{L} = \frac{\partial \mathbf{U}}{\partial \mathbf{X}} = \sum_{j=1}^{N_j} (\mathbf{U}_j - \mathbf{U}_i) \nabla_0 W_{0ij} V_{0j} \quad (2.56)$$

The Euler-Almansi strains can be obtained thanks to the GL strain and the deformation gradient tensors, and hence the work conjugated Cauchy stress is determined based on the generalized Hooke's law.

To transform the equilibrium equation written in the current configuration into the initial configuration, the Cauchy stress and viscous forces need to be pulled back through the deformation gradient

$$\mathbb{P} = J \boldsymbol{\sigma} \mathbb{F}^{-T}; \quad \mathbb{P}_v = J \Pi \mathbb{F}^{-T} \quad (2.57)$$

The final discretized equilibrium equation is expressed with the respect to the initial configuration

$$\frac{d\mathbf{v}_i}{dt} = \sum_{j=1}^{N_j} \left( \frac{\mathbb{P}_i}{\rho_{0i}^2} + \frac{\mathbb{P}_j}{\rho_{0j}^2} - \mathbb{P}_{vij} \right) \nabla_0 W_{0ij} \rho_{0j} V_{0j} \quad (2.58)$$

## 2.7 Time step and time integration

The present study focuses on the prediction of the deformation fields (displacement, velocity, acceleration) and internal values (strains, stresses) in a structure. Explicit time integration scheme is widely employed because the nonlinearities are overcome straightforwardly since no iterations are required at each time step.

A viscously damped dynamical system can be expressed as the following generalized PDE formulation

$$\mathbb{M} \dot{\mathbf{U}} + \mathbb{C} \dot{\mathbf{U}} = \mathbf{R} = \mathbf{F}_{ext} - \mathbf{F}_{int} \quad (2.59)$$

where  $\mathbb{M}$  and  $\mathbb{C}$  represents the mass and damping matrices;  $\mathbf{R}$  is the residual force vector between the external force vector  $\mathbf{F}_{ext}$  and internal force vector  $\mathbf{F}_{int}$ .



For a particle  $i$ ,  $(\mathbf{F}_{ext})_i = b_i V_i$  where  $b$  is the body force per unit volume. The internal force vector  $(\mathbf{F}_{int})_i$  is the product of the mass matrix with the RHS of the Equation (2.58). Rayleigh damping model (also called proportional damping) defined as  $\mathbb{C} = \alpha_C \mathbb{M} + \beta_C \mathbb{K}$ , is used in this investigation which has been extensively used to reduce the undesirable vibration in an oscillatory system [79]. The stiffness proportional term  $\beta_C \mathbb{K}$  is insignificant for low-frequency applications and this model can reduce to a single mass proportional term [80].

The total simulation duration  $T_t$  is assumed to be divided in  $N_t$  equal time-steps  $\Delta T$ . The initial conditions are assumed to be given by

$$\mathbf{U}(T = 0) = \mathbf{U}^0 \quad \text{and} \quad \dot{\mathbf{U}}(T = 0) = \dot{\mathbf{U}}^0 \quad (2.60)$$

Central difference method is based on the Taylor's series expansion of  $\mathbf{U}^{n+1}$  and  $\mathbf{U}^{n-1}$  about  $\mathbf{U}^n = \mathbf{U}(T = T_n)$  at current time step  $n$ .

$$\begin{cases} \mathbf{U}^{n+1} = \mathbf{U}^n + \Delta T \dot{\mathbf{U}}^n + \frac{\Delta T^2}{2} \ddot{\mathbf{U}}^n + \frac{\Delta T^3}{6} \dddot{\mathbf{U}}^n + \dots \\ \mathbf{U}^{n-1} = \mathbf{U}^n - \Delta T \dot{\mathbf{U}}^n + \frac{\Delta T^2}{2} \ddot{\mathbf{U}}^n - \frac{\Delta T^3}{6} \dddot{\mathbf{U}}^n + \dots \end{cases} \quad (2.61)$$

Calculating the velocity  $\dot{\mathbf{U}}$  and acceleration  $\ddot{\mathbf{U}}$  by only taking into account the first three terms of the RHS of Equation (2.61), and substituting the results into the Equation (2.59), an explicit time integration form of the displacement champ is generated

$$\mathbf{U}^{n+1} = \frac{4}{2 + \alpha_C \Delta T} \mathbf{U}^n + \frac{\alpha_C \Delta T - 2}{2 + \alpha_C \Delta T} \mathbf{U}^{n-1} + \frac{2\Delta T^2}{2 + \alpha_C \Delta T} \ddot{\mathbf{U}}^n \quad (2.62)$$

Repeated application of the above equation gives us the response time history of the displacement field. Note that in order to compute the  $\mathbf{U}^1$ , both  $\mathbf{U}^0$  and  $\mathbf{U}^{-1}$  are required. The last term  $\mathbf{U}^{-1}$  can be obtained from the Equation (2.61) by neglecting the third-order and higher derivatives at  $T = 0$

$$\mathbf{U}^{-1} = \mathbf{U}^0 - \Delta T \dot{\mathbf{U}}^0 + \frac{\Delta T^2}{2} \ddot{\mathbf{U}}^0 \quad (2.63)$$

where the acceleration  $\ddot{\mathbf{U}}^0$  can be computed from the Equation (2.59) with the initial conditions and internal/external forces.

The use of the central difference method leads to a system of uncoupled linear equations and only vector operations are performed thanks to the use of a diagonal mass matrix. This leads to less CPU-time requirement per time step, compared to the implicit methods.

However, the explicit methods are well-known to be conditionally stable. For most problems, the time step is given by the Courant limit, in which the smallest amount of time necessary for a sound wave to cross the particle distance  $r_{ij}$  [81],

$$\Delta T = C_t \Delta T_{crit} = C_t \cdot \min(r_{ij}/c) \quad (2.64)$$

where  $c$  is the sound speed in the material and generally equal to  $\sqrt{E/\rho}$ . The factor  $C_t = 0.8$  is sufficient for moderately nonlinear problems and 0.8 or smaller value has to be used for highly nonlinear problems.

## 2.8 Numerical applications

In this section, geometrically linear and nonlinear analysis of several numerical applications are presented and the obtained results are compared with reference analytical solutions and FE results obtained using ABAQUS<sup>©</sup> commercial software. The quadratic term  $\mathbf{L}^T \mathbf{L}$  in the GL strain tensor is ignored in the geometrically linear analysis.

All applications hereinbelow involve thin-walled structures in which three-dimensional (3D) solid problems can be degraded to two-dimensional (2D) problems and plane stress assumption is taken into account. Note that, in the 2D continuum SPH formulations, the factor  $\alpha_d$  is chosen to be  $15/7\pi h^2$  and the region occupied by a particle is described by the area  $A$  rather than the volume  $V$ . A default is made for all examples that the thickness always follows the  $z$ -direction and 2D problem are described in the  $xz$ -plane.

### 2.8.1 Geometrically linear analysis

#### 2.8.1.1 Deflection of cantilever beam with tip load

The first application studied here is a cantilever beam made of a steel material with the properties  $E = 210GPa$  and  $\nu = 0.3$ . The geometrical dimensions of the structure are shown in Figure 2.8, where the length  $L = 100mm$ , the width  $b = 1mm$  and the beam thickness  $t = 10mm$ . The beam is clamped at one edge and supports a concentrated load  $F$  at the other edge. The load is applied gradually following a quadratic evolution (see Figure 2.9), starting from 0 to reach its maximum value  $1750N$  at time  $T_1 = 1.5ms$ . Then the load is maintained constant until the end of simulation  $T_{total} = 3ms$ . The static reference solution obtained using linear analysis of beam deflection  $W_C$  has been reported by Timoshenko [82], and corresponds to  $W_{analytical} = \frac{FL^3}{3EI} + \frac{6FL}{5GA} = 33.59mm$ .

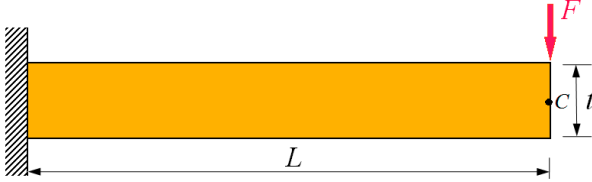


Figure 2.8: Cantilever beam with tip load

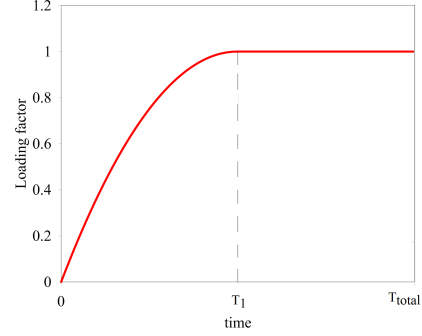


Figure 2.9: Applied load evolution in time

Firstly we propose to investigate the influence of the smoothing length on the accuracy of the result obtained using the present 2D-continuum SPH model. As reported in the literature [50, 51], the smoothing length  $h$  is a key parameter in the SPH method and has a great influence upon the general solution. The idea hereby is to conduct a sensitivity analysis of the smoothing length  $h$  in order to find its optimal value that has a less influence on the solution while keeping a reasonable computational time. The smoothing length  $h$  is directly related to the pair of particles diameters  $d_i$  and  $d_j$

$$h_{ij} = \lambda_h \frac{d_i + d_j}{2} \quad (2.65)$$

where  $\lambda_h$  is a coefficient which is often suggested to be [0.8, 1.5] [83].

We discretize the beam uniformly using  $100 \times 10$  particles of a uniform diameter  $d = 1mm$ . The present 2D-continuum SPH model is based on an explicit dynamic resolution scheme, therefore in order to reach the permanent deflection corresponding to the static solution, one has to include damping for energy dissipation. For this application we applied a damping using  $\alpha_C = 6$  and  $\beta_C = 0$ . Different ratios  $h/d$  from 0.8 to 2.0 were used and the corresponding non-dimensional  $W_C/W_{analytical}$  values are depicted in Figure 2.10. As we can observe, when  $h/d$  gets far away from the value 1 the quality of the predicted solution deteriorates rapidly. However the predicted end-deflection becomes very close to the analytical solution when  $h/d$  approaches 0.95. Therefore, the smoothing length of  $0.95d$  is adopted as a default value for the remaining applications in this chapter. In this case, each interior particle possess 8 neighboring points in its support domain for a regular particles distribution. This is found to be slightly different from what is reported in some commercial softwares such as LS-DYNA<sup>®</sup> which suggests  $h/d = [1.05, 1.3]$  [85].

In the following we carried out a sensitivity analysis of the particles discretization. Different

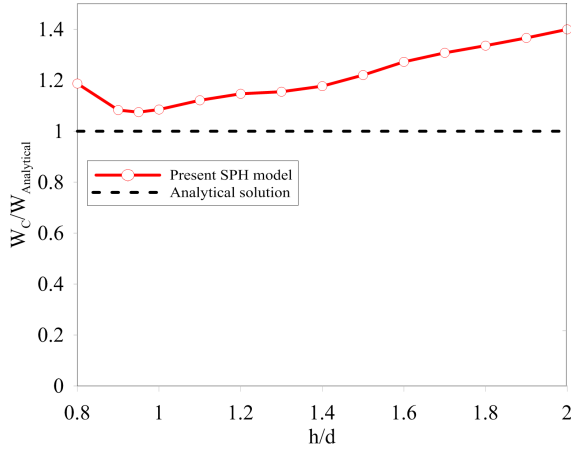


Figure 2.10: Influence of the smoothing length

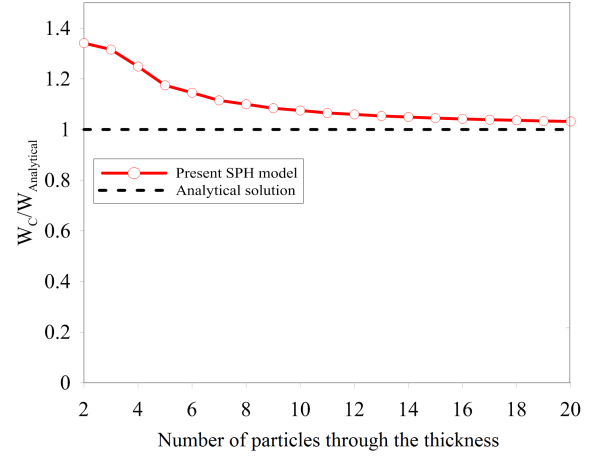


Figure 2.11: Influence of particles discretization

uniform discretizations have been used, starting from 2 particles through the thickness until 20 particles. For every case, the solution  $W_C/W_{analytical}$  is selected and the evolution of the end-deflection versus number of particles is depicted in Figure 2.11. As one can observe, the predicted SPH end-deflection converges to the analytical solution as the number of particles increases. When the number of particles is over 10, the error between the end-deflection obtained using the proposed 2D continuum SPH model and the analytical value is less than 6.6%, which is acceptable.

In above investigation, the artificial viscosity coefficients are fixed as  $\alpha_{II} = 0.2$ ,  $\beta_{II} = 0.4$ , where this combination has been shown to be suitable for most applications. Thus, this couple of parameters is adopted for the remaining cases of isotropic materials.

The appropriately defined artificial viscosity can efficiently prevent the unphysical oscillations, that occur during the numerical analysis of shock wave. In order to illustrate the viscosity influence on the solution, we conducted a study by varying the two coefficients ( $\alpha_{II}$ ,  $\beta_{II}$ ) from 0.02 to 0.4. In Figure 2.12 are shown four configurations obtained using different couples of values. We can remark that stability is affected severely when the coefficients are small, and the more the values increase better is the stability of the solution. Different calculations have been carried out, and the authors found that  $\alpha_{II} = 0.04$ ,  $\beta_{II} = 0.08$  are the minimum values which allow achieving a first stable solution.

Figure 2.13 shows the distribution of transverse shear stress  $\sigma_{xz}$  through the thickness at  $x = 50mm$ , this is obtained using different discretizations of particles from 2 to 10 particles on the thickness. The predicted shear stress  $\sigma_{xz}$  is compared with the analytical well-

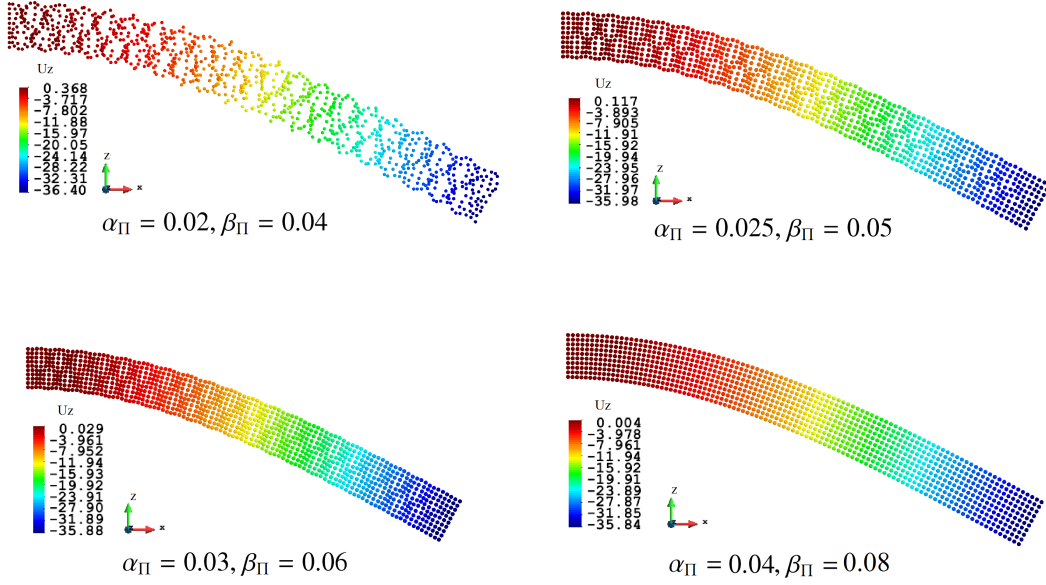


Figure 2.12: Deformed configurations with different viscosity

known solution, which is quadratic in thickness for the case of elastic isotropic materials

$$\sigma_{xz}^{analytical} = \frac{F}{2I} \left( \frac{t^2}{4} - \left(z - \frac{t}{2}\right)^2 \right).$$

One can observe that the present 2D-continuum SPH model can predict the shear stress accurately even with only two particles in the thickness with an error of approximately 29.6%. When three particles are used, this error drops to 10.9% and for only four particles the error is less than 1.4%. As we can see from Figure 2.13, the predicted shear stress distribution obtained using 10 particles is very close to the analytical solution of a quadratic shape.

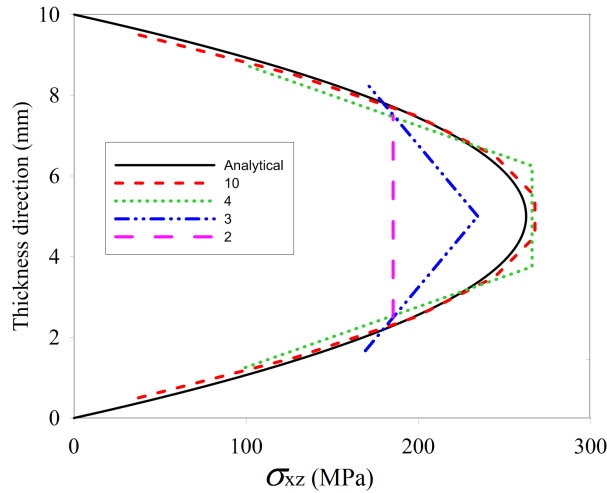


Figure 2.13: Shear stress distribution through the thickness at  $x = 50mm$ .

### 2.8.1.2 Cook's membrane

The second application deals with the well known Cook's membrane problem [86], which is depicted in Figure 2.14(a) where geometrical dimensions are given. The tapered structure is clamped on its left edge and subjected to a uniformly distributed total shear load of  $1kN$  on the opposite free edge.

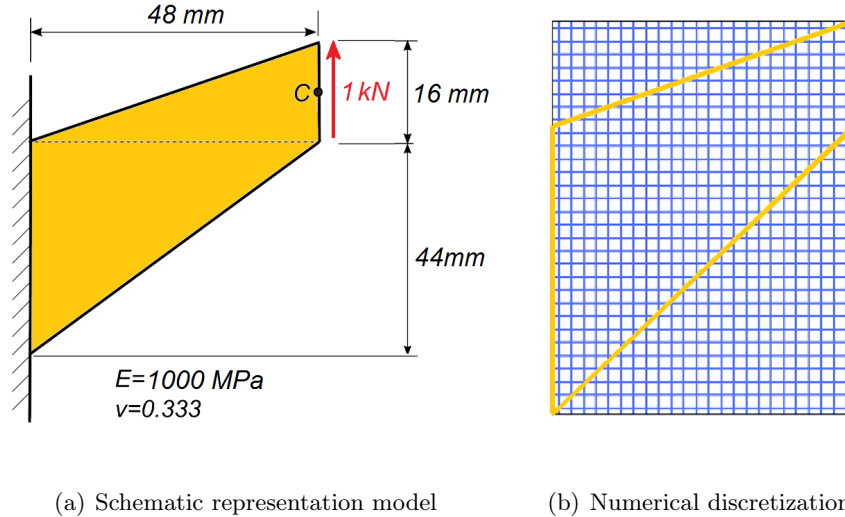


Figure 2.14: Cook's membrane

As shown in Figure 2.14(b), a larger rectangle domain including the whole geometry of the structure is first discretized using a uniform particles distribution with a gap of  $1mm$ . The particles which are located inside the geometry domain of the structure are considered as SPH particles and are used for the modeling of the Cook's membrane deformation.

In Figure 2.15 are given the initial and deformed configurations of the Cook's membrane. Compared with the reference vertical deflection [86] of the middle point  $C$  at the right free edge  $23.81mm$ , the result obtained using the 2D-continuum SPH model is  $24.99mm$  which is in good agreement with the reference solution, with an error less than 4.9%.

## 2.8.2 Geometrically nonlinear analysis

### 2.8.2.1 Large deflection of a cantilevered beam

The cantilever beam studied in the first application (Example 2.8.1.1) with its dimensions given in Figure 2.6 is considered again by taking into account the geometrically nonlinear behavior. The end load is applied gradually on the right free edge, starting from 0 to  $17.5kN$  ( $FL^2/EI$  is ranged from 0 to 10). In the present application, the structure is discretized

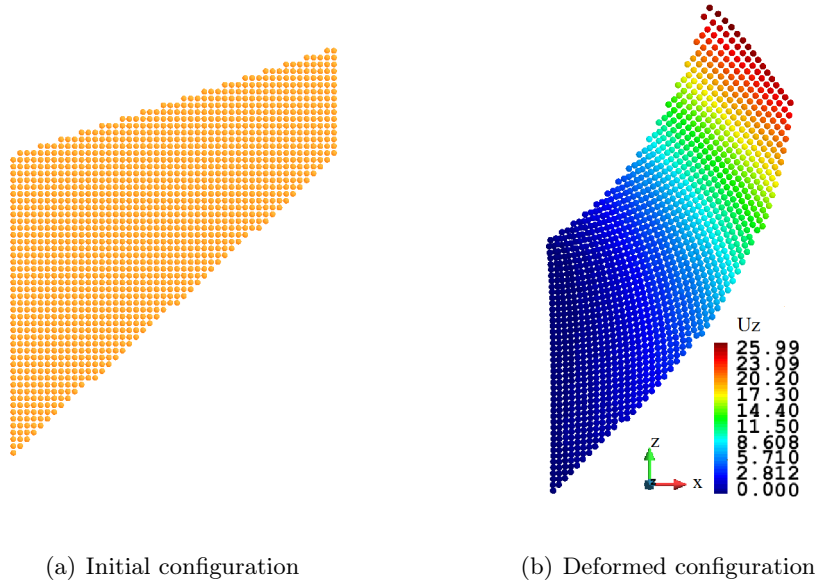


Figure 2.15: Configurations of Cook's membrane

uniformly using 100 particles along the length and 10 particle through the thickness.

A nonlinear analysis is carried out using a loading control strategy while the deflection of the beam free edge centroid  $C$  is stored. The obtained results are summarized in Table 2.1 and a comparison is made with respect to the reference solution given by Timoshenko [82].

We can observe that the results obtained by the proposed 2D-continuum SPH model are in good agreement with the reference solution. We also remark that the error decreases as the deflection increases (load increases), which indicates a good stability and efficiency of the proposed SPH model in the modeling of large displacements and large rotations of structure.

For comparing the computation time consumed for the dynamic analysis of the clamped beam by the present SPH model and ABAQUS<sup>®</sup> FE model, a FE model using ABAQUS<sup>®</sup> explicit dynamics scheme with the same number of CPS4R elements is solved. The maximal force  $17.5kN$  is considered and the loading process is referred to 2.9. In contrast to 13s CPU-time expended by the ABAQUS<sup>®</sup> model, the proposed SPH model is more fast and only consumes 0.546s. The deflection of the free edge centroid is 84.0mm solved by ABAQUS<sup>®</sup> explicit dynamics scheme, which includes an higher error than the presented SPH model. The deformed configurations of the clamped beam obtained these two models are presented in Figure 2.16.

We can also observe from Figure 2.16 that the obtained deformed structures using the

Table 2.1: Comparison of the end-beam deflection  $W_C$  (mm)

F (kN)	$FL^2/EI$	Analytical	SPH model	Error (%)
0	0	0	0	—
0.4375	0.25	8.3	8.9	7.35
0.875	0.5	16.2	17.4	7.41
1.3125	0.75	23.5	25.2	7.19
1.75	1	30.2	32.1	6.29
3.5	2	49.4	51.7	4.55
5.25	3	60.3	62.5	3.62
7	4	67.0	69.0	2.99
8.75	5	71.4	73.3	2.63
10.5	6	74.4	76.3	2.57
12.25	7	76.7	78.6	2.45
14	8	78.5	80.4	2.39
15.75	9	79.9	81.8	2.43
17.5	10	81.1	83.1	2.42

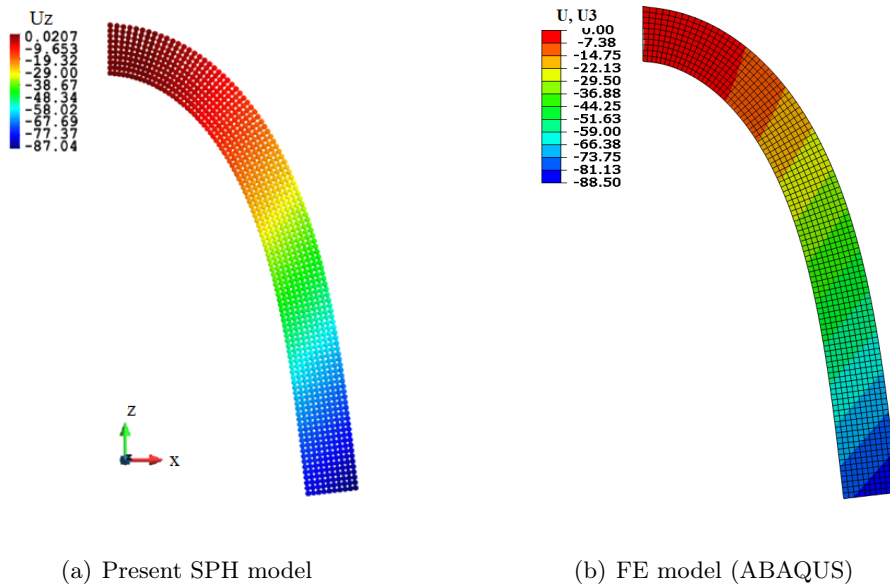


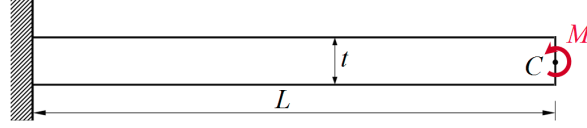
Figure 2.16: Final deformed configurations under maximal load (SPH *vs.* FEM)

proposed 2D-continuum SPH model 2.16(a) is of a very close shape to the one obtained using the FE method 2.16(b).

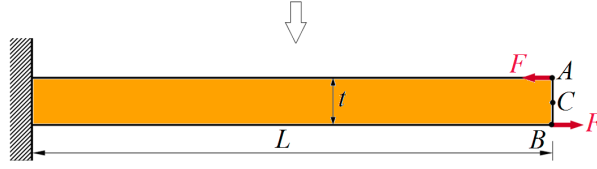


### 2.8.2.2 Roll up of a clamped beam

In this example, a clamped beam strip under a bending moment is studied. The geometrical dimensions of the structure are shown in Figure 2.17, where the length  $L = 100mm$ , the width  $b = 5mm$  and the beam thickness  $t = 5mm$ . This strip is made of an aluminum material with the properties  $\rho = 2700kg/m^3$ ,  $E = 73.4GPa$  and  $\nu = 0.3$ .



(a) Idealized beam with end-moment



(b) Equivalent studied beam model

Figure 2.17: Geometry and loading of a clamped beam strip

In order to carry out the nonlinear analysis of the structure given in Figure 2.17(a), the idealized moment acting at the free edge of the beam can be generated using a couple of follower forces applied normal to the free edge  $AB$  and are maintained normal to the edge  $AB$  during all simulation process, showed in Figure 2.17(b).

The analytical solution of the curvature  $\kappa$  at the end central point  $C$  is given by Euler formula [87]  $\kappa = M/EI$ . For the chosen properties, the value of the bending moment which transforms the beam into a full-circle shape is  $M = Ft = 2\pi EI/L = 76.46\pi \text{ kN} \cdot \text{mm}$  thus the correspondent force  $F = 15.29\pi \text{ kN}$ .

The structure is discretized using  $200 \times 10$  particles of diameter  $0.5mm$ . The load  $F$  is applied incrementally using the parameter  $\lambda$  such as  $F = M/t = \lambda \pi EI/L$ , where  $\lambda = \{0.1, 0.2, \dots, 2\}$ . For comparison purpose, a first trial analysis using the CPS4R 2D solid element of ABAQUS<sup>®</sup> has been conducted, unfortunately the simulations failed to achieve the maximal rotation of  $2\pi$ . Therefore an alternative FE analysis was conducted on the same structure using  $200 \times 10$  S4R shell elements of ABAQUS<sup>®</sup> through an implicit static scheme. The FE result will be taken as a reference solution to evaluate the quality of the SPH model.

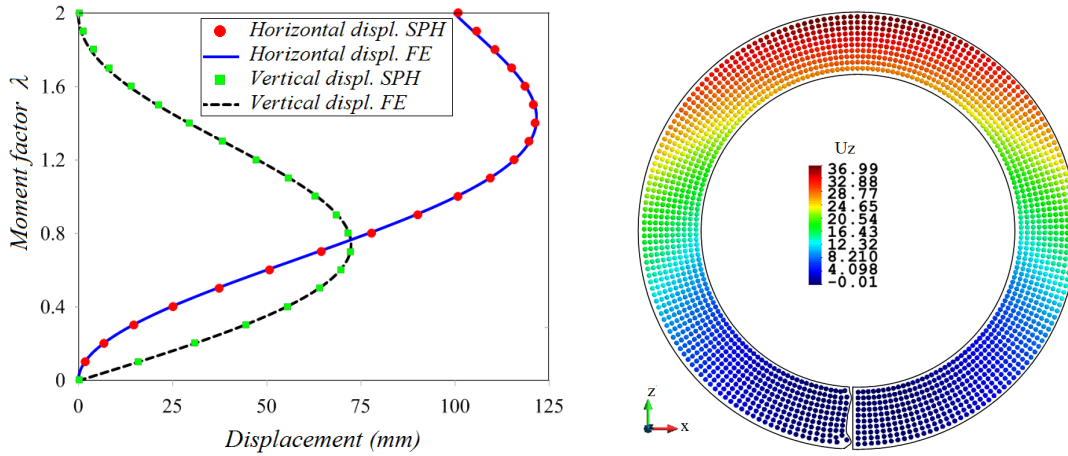


Figure 2.18: Comparison of load-displacement of the strip (SPH *vs.* FE)      Figure 2.19: Deformed configuration of the strip (SPH solution)

Figure 2.18 shows the load-displacement paths at point  $C$ , where one can remark the highly nonlinear behavior exhibits by the structure. As we can observe the solution obtained using the present SPH model matches perfectly the FE solution obtained using ABAQUS<sup>®</sup> code. The analysis of the overall loading path shows that the error of the present SPH model is less than 1% compared to the FE solution, and this is true even for very large rotations up to  $2\pi$ .

Comparison of the vertical displacements at point  $C$  obtained for the maximal load corresponding to  $\lambda = 2$ , gives  $0.055\text{mm}$  for the present SPH model and  $-0.006\text{mm}$  from the FE model. This means the straight beam is transformed closely to a circle. The final deformed strip shape is drawn in Figure 2.19 where the proposed 2D continuum SPH model is capable of representing the nonlinear behavior of the structure even involving large rotation.

### 2.8.2.3 Post-buckling analysis of shallow arch

In the present application, we investigate the nonlinear buckling behavior of a thin shallow arch subjected to a central pinching force. The two ends of the arch are pinned as shown in Figure 2.20. The geometrical data are given as follows (Figure 2.20):  $R = 200\text{mm}$ ,  $L = 100\text{mm}$ ,  $t = 5\text{mm}$  and width  $b = 1\text{mm}$ . The arch is made of steel with a Young's modulus of  $E = 210\text{GPa}$  and a Poisson ratio corresponding to  $\nu = 0.3$ .

The arch is discretized using 425 particles along the circumference and 10 particles in the radial direction. For comparison purpose, the same structure is analyzed using  $425 \times 10$  CPS4R 2D solid elements of ABAQUS<sup>®</sup>. The FE results will constitute a reference solution

for the validation of the SPH results. The nonlinear analysis is conducted using the explicit dynamics scheme.

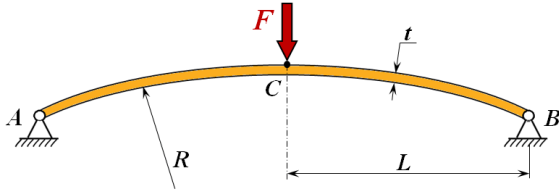


Figure 2.20: Pinned-pinned shallow arch

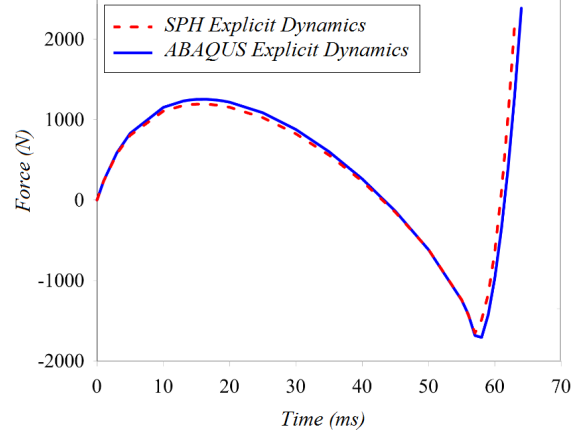
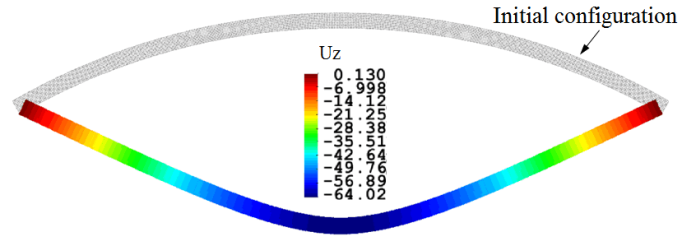


Figure 2.21: Comparison of load-displacement path at the central point

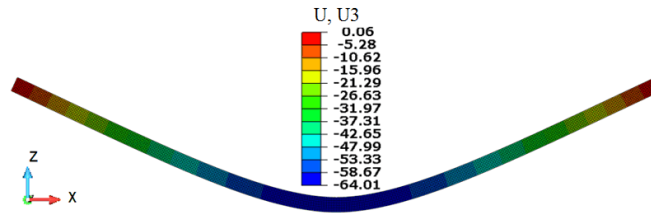
In this problem, the loading control technique failed to pass through the first limit point where the stiffness matrix becomes singular. To achieve the global response of the arch under these conditions, a displacement control technique [88] of the central top point of the arch is carried out with a maximal displacement corresponding to  $W_C = 64mm$  which is imposed incrementally.

In Figure 2.21 are plotted the load-displacement curves obtained using both ABAQUS<sup>®</sup> code and the proposed SPH model. The critical buckling load predicted by the present 2D continuum SPH model corresponds to  $F_{cr}^{SPH} = 1205.3N$  with a deflection of  $W_C^{SPH} = 15.5mm$ , while the reference critical buckling load of FE is  $F_{cr}^{ABA} = 1261.8N$  for the same deflection. As we can see from Figure 2.21, the proposed SPH model allows obtaining a very good solution with an error less than 4.5% when compared to the FE solution. This solution represents a very good approximation for a thin structure ( $t/R = 0.025$ ). We can observe from Figure 2.21 that the present SPH model can achieve a good accuracy even in the post-buckling phase, where the second bifurcation point is captured also accurately without difficulties.

The deformed arch shapes corresponding to the maximal displacement ( $W_C = 64mm$ ) are shown in Figure 2.22. As one can remark, the two deformed structures are of approximately the same shape, which indicates the accuracy of the present SPH model.



(a) Present SPH model



(b) FE model (ABAQUS)

Figure 2.22: Comparison of deformed configurations of the arch at maximal displacement

#### 2.8.2.4 Post-buckling analysis of a deep arch

Herein, we investigate the buckling behavior of a thin structure made of an deep arch shape and subjected to a central pinching force. The arch is clamped at its two ends as shown in Figure 2.23. Similar planar circular arches with different boundary conditions have been studied by Yau [89], Wriggers and Simo [90].

The arch is made of steel with a Young's modulus of  $E = 210GPa$  and a Poisson ratio corresponding to  $\nu = 0.3$ . The geometrical characteristics of the structure are as follows (see Figure 2.23):  $R = 100mm$ ,  $t = 5mm$ ,  $b = 1mm$  and  $\phi = 215^\circ$ .

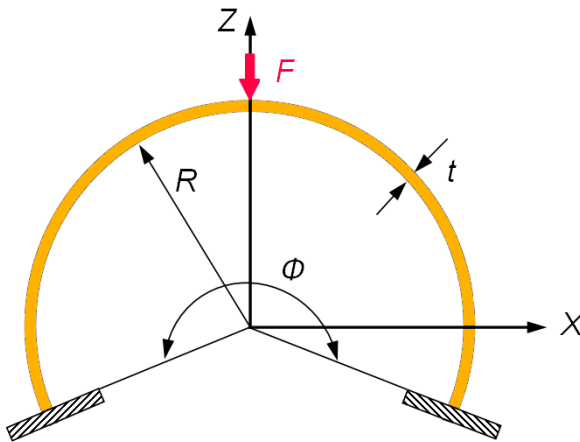


Figure 2.23: Clamped-clamped deep arch

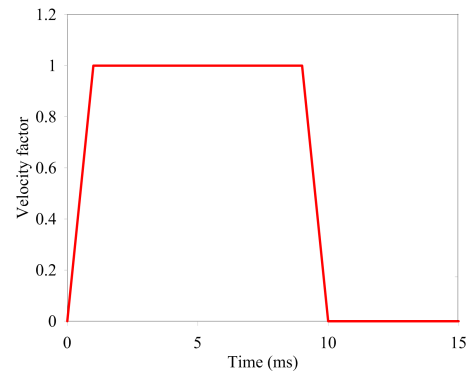


Figure 2.24: Velocity control factor

Due to the symmetry, only one half of the arch is modeled and discretized with  $387 \times 10$  particles of diameter  $0.5\text{mm}$ . For comparison purpose, the same structure is analyzed using a FE model of ABAQUS<sup>®</sup> which will constitute a reference solution for the validation of the SPH results. The FE model consists of the same number of CPS4R 2D elements using the explicit dynamic analysis. Similar as the precedent application, the displacement control strategy for the central top point of the arch is employed to overcome the first buckling limit point.

For the numerical resolution, the velocity control curve given in Figure 2.24 is used. At the first stage a linear velocity is imposed, starting from 0 to reach a maximal velocity of  $27.78\text{m/s}$ . Then the velocity is maintained constant during  $8\text{ms}$  to achieve the required displacement. The last stage is a deceleration using the same slope as in the first stage. In order to avoid oscillations due to the deceleration, the solution is evaluated  $5\text{ms}$  after vanishing the velocity at  $10\text{ms}$ . Damping forces are introduced by means of  $\mathbb{C} = 6\text{M}$ , to allow obtaining the quasi-static solution.

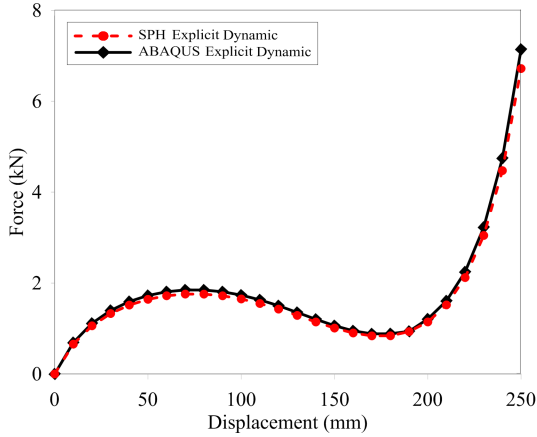


Figure 2.25: Load-Displacement curve at the central point of the arch

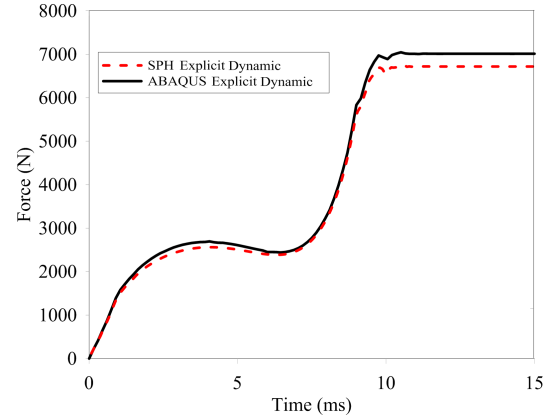


Figure 2.26: Predicted loading history ( $W_C = 250\text{mm}$ )

Resulted load-displacement curves are depicted in Figure 2.25. The critical buckling load predicted using the present SPH model is  $F_{cr} = 1761.7\text{N}$  with a deflection corresponding to  $W_C = 75\text{mm}$ , while the reference critical buckling load  $F_{cr} = 1893.41\text{N}$  is obtained for the same deflection using FE model. A first comparison of the buckling load values, shows that the proposed SPH model gives a good solution with an error less than 7%, which constitutes a very good approximation when considering a very thin structure ( $t/R = 0.05$ ). We can observe from Figure 2.25 that the present SPH model can achieve a good accuracy even in

the post-buckling region, where the second limit point is captured also accurately.

In Figure 2.26 is presented the loading history of the arch until achieving a total displacement of  $250\text{mm}$ . It shows the nonlinear character of the loading path that is needed if one wants to use the classical loading control procedure.

The final deformed configurations ( $W_C = 250\text{mm}$ ) obtained using the present SPH model and the FE method are shown in Figure 2.27, as we can remark the two deformed structures are of the same shape, which indicates the efficiency of the present SPH model.

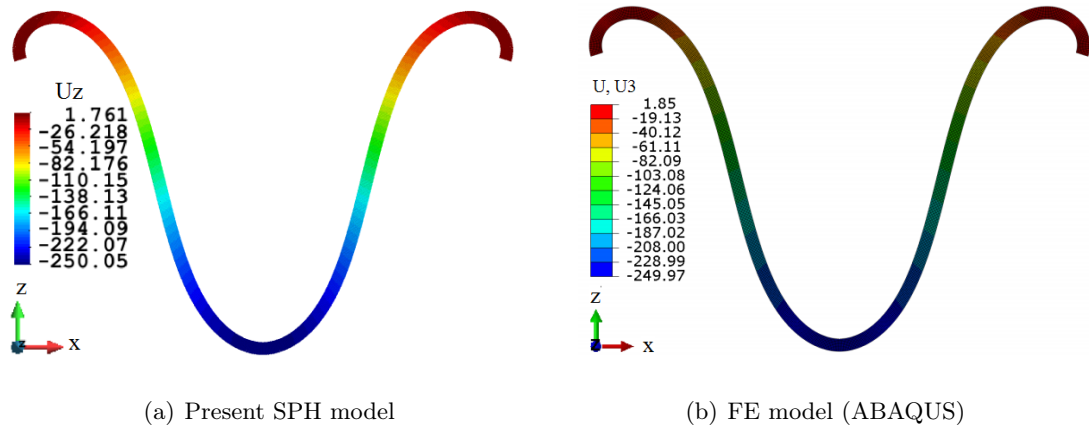


Figure 2.27: Deformed configurations of the deep arch at maximal displacement

### 2.8.2.5 Delamination of a sandwich beam

In the last application, nonlinear analysis of a sandwich beam is carried out using the proposed SPH model. The studied beam is depicted in Figure 2.28, in which the loads are imposed on the upper face points  $A$  and  $B$  which located at a distance of  $60\text{mm}$  from the two ends.

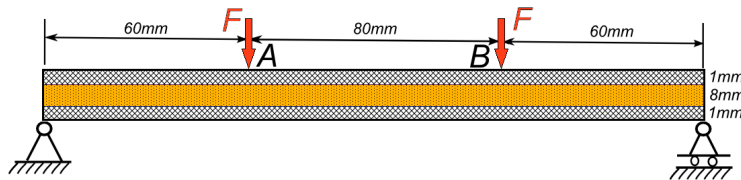


Figure 2.28: Four points bending test on a sandwich beam

The left-bottom end of the lower sheet layer is simply fixed while the other end is simply supported and can freely move through the longitudinal direction. The overall span of the beam is  $200\text{mm}$  and its width is  $b = 1\text{mm}$ . Top and bottom faces are made of an isotropic

aluminum with  $E^f = 73.4GPa$ ,  $\nu^f = 0.32$  and thickness of  $t^f = 1mm$ . The core is a polymer with elastic constant  $E^c = 0.16931GPa$ ,  $\nu^c = 0$  and the thickness is  $t^c = 8mm$ . The material densities are  $\rho^f = 2700kg/m^3$  and  $\rho^c = 468kg/m^3$  respectively. A similar test using FE method can be found in the Kemmochi [91].

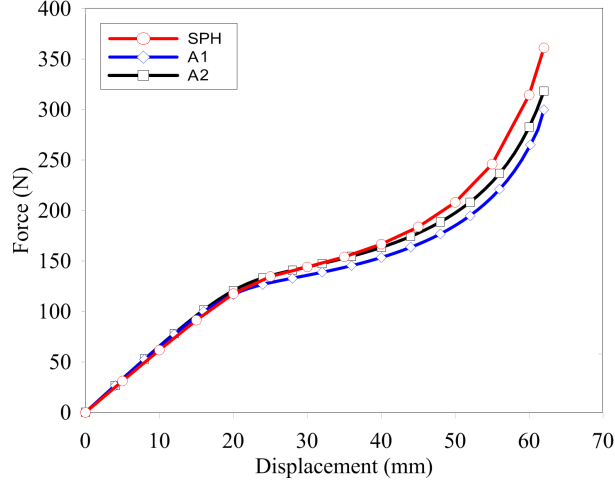


Figure 2.29: Force-displacement curve at point A

The beam is discretized using a uniform distribution of particles with a gap of  $0.5mm$ , allowing the use of 2 particles in the faces, 16 particles in the core, while the overall span of the beam uses 400 particles.

The displacement control procedure is adopted and the prescribed displacement  $W = 65mm$  was applied on the points A and B simultaneously. The displacement is applied gradually starting from 0 until reaching its maximal value of  $65mm$  during  $T_1 = 3ms$  as described in Figure 2.9, then the displacement is maintained constant during  $4ms$  until the end of computation.

For comparison purpose, a FE model is built using ABAQUS<sup>®</sup> implicit software, and two different meshes are analyzed. The first FE model (A1) uses the same discretization as the SPH model, *i.e.* a mesh of 2 – 16 – 2 CPS4R four-node elements is used to discretize the beam thickness. In the second FE model (A2) a refinement is used for the faces with 4 elements instead of 2 previously.

In the present application, several analyses have been conducted to study the influence of the viscosity parameters, and it has been found that setting the constants  $\alpha_{II}$  to 2.5 and  $\beta_{II}$  to 0.6 is a good compromise between stability and calculation efficiency.

The load-displacement response of the beam under the load obtained using the present

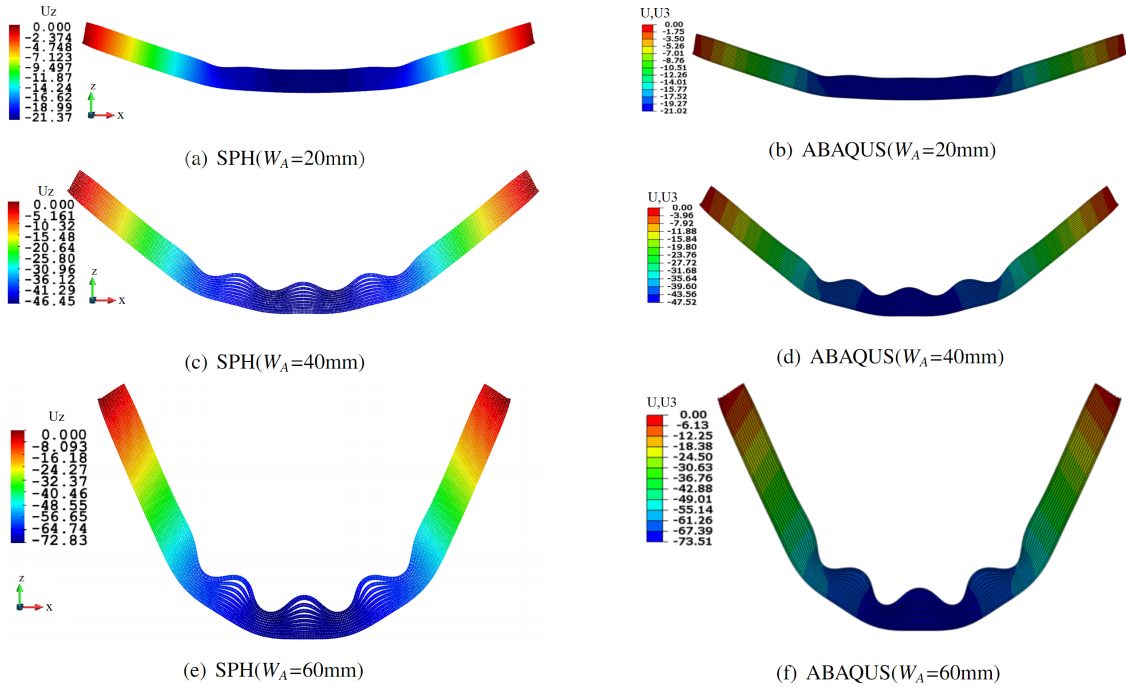


Figure 2.30: Deformed configuration of the sandwich beam

SPH model together with the solutions obtained using ABAQUS<sup>®</sup> implicit software are given in Figure 2.29. We can observe the linear behavior of the solution at the beginning of loading up to 20mm of deflection, where all three solutions are the same.

As we can see from Figure 2.30, after 20mm of deflection, a local buckling (wrinkling) appears at the vicinity of the load, this phenomenon continues amplifying while the load increases, involving the emergence of ears in the beam area located between the two forces. These wrinkles are accompanied locally with big alternating values of the stresses along the length direction ( $\sigma_{zz}, \sigma_{xz}$ ) which will cause the peeling of the faces from the core and therefore initiating the delamination.

From Figure 2.29, we can see that the beam behaves nonlinearly at 20mm of deflection, which corresponds to the wrinkling initiation. From 20mm until 60mm the nonlinear response of the structure given by models A1 and A2 is correctly predicted by the present SPH model with a small overestimation of the load. We can also observe that the solution obtained using the proposed SPH model with only 2 particles in the faces is closer to the FE solution obtained using the fine mesh A2.

A quantitative comparison between the in-plane stress distributions obtained using the SPH model and the FE method is given in Figure 2.31. As one can see, the predicted



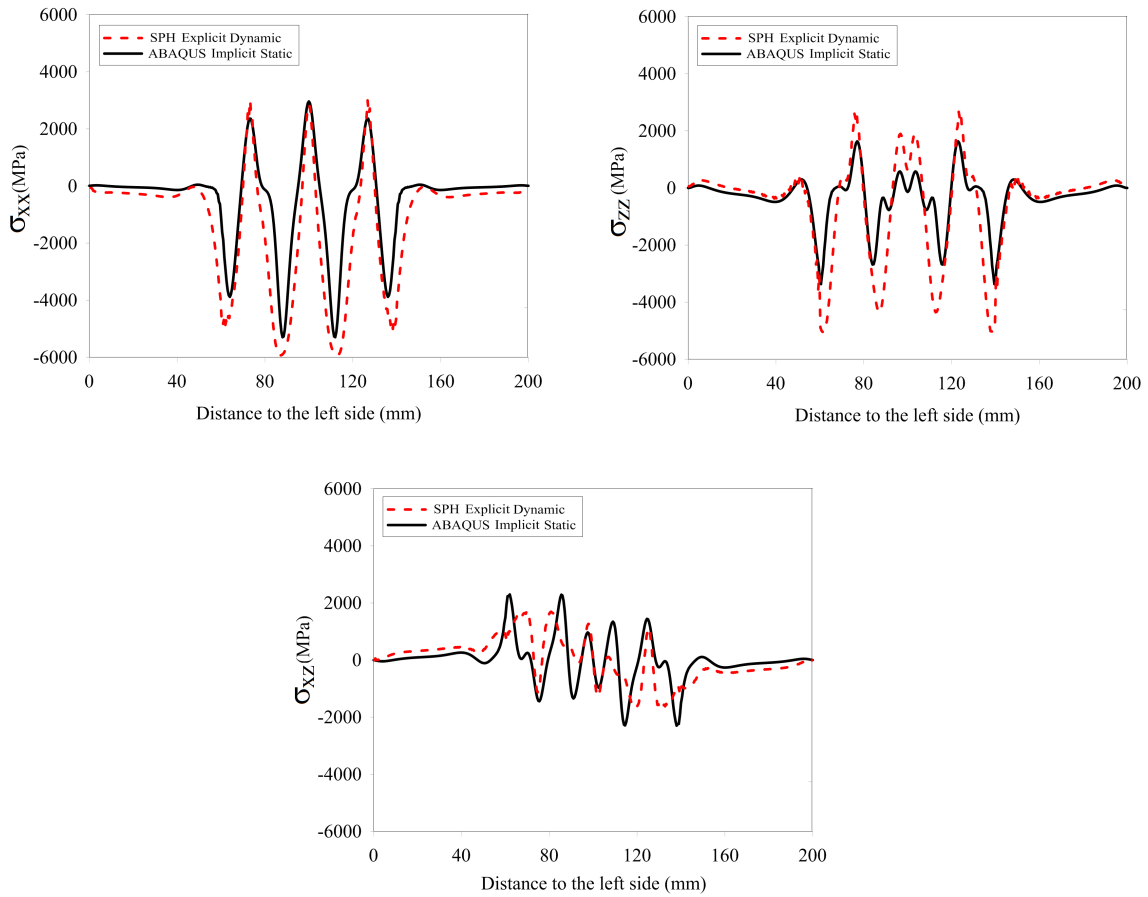


Figure 2.31: Stress distribution on the top face of the sandwich beam

longitudinal stress  $\sigma_{xx}$  variation is very close to the one obtained using the FE model. In this application, we can observe also that the transverse stress  $\sigma_{zz}$  is not neglectable compared to the longitudinal stress. We can remark that maximal values of the predicted transverse stress using the present SPH model are higher than the one obtained using the FE model. This can be explained by the fact that the FE model uses a reduced integration element with only one quadrature point at the centroid. This type of integration scheme is well-known to be not suitable for the stress estimation. An observation of the shear stress distribution (Figure 2.31), shows that the SPH solution is in a good agreement with the FE prediction obtained using ABAQUS<sup>®</sup> software. This demonstrates the robustness of the SPH model for the transverse stress prediction and therefore may constitute a good tool for the delamination prediction.

## 2.9 Conclusion

In this Chapter an efficient continuum SPH method for the analysis of 2D solids is presented. In the present model we adopted the constitutive material relations to link naturally the stresses and strains, which is original and differs from the classical SPH approaches commonly based using the state equation to determine the hydrostatic pressure. The boundary deficiency of the classical SPH method was eliminated by the use of the Corrective Smoothed Particle Method. Therefore, it is now easy to impose directly the prescribed displacements values on the boundaries, without the need of the so-called "*virtual*" or "*ghost*" particles as often used in the classical SPH method. The Total Lagrangian approach was investigated to alleviate the so-called tensile instability problem, allowing at the same time avoiding the updating procedure of the neighboring particles search and therefore reducing CPU usage. The resulting 2D continuum SPH model is fast and efficient tool for the geometrically linear and nonlinear analysis of thin or thick structures.

Several numerical applications involving solids and structures undergoing large transformations (displacements and rotations) have been successfully carried out using the proposed 2D continuum SPH model. The explicit dynamic scheme was used for time integration allowing a fast resolution algorithm even for highly nonlinear problems. The obtained results were compared to the reference solutions taken from the literature as well as with some numerical reference solutions of the FE using ABAQUS<sup>®</sup> commercial software. Through the numerical applications, the present 2D continuum SPH model appears to be fast and precise and therefore very suitable for the study of thin two-dimensional structures undergoing large transformations. The authors believe that the present 2D continuum SPH model can provide an alternative way for the analysis of the geometrically nonlinear structures.

# *SPH formulation for isotropic shell structures*

---

This chapter will present the generalization procedure of the 2D SPH for the modeling of shell structures. The Mindlin-Reissner shell theory suitable for thin/thick structures is chosen for describing the shell kinematics. Only the mid-surface of the structure is discretized using only one layer of particles to represent the behavior of the whole shell structure. The strong-form of the governing equilibrium equations of shell structures are discretized thanks to the Total Lagrangian SPH formulation and solved using the Explicit Dynamics time integration scheme. The treatment of large rotations of very thin shells is carried out using the vectorial parameterization of Rodrigues and also by using the quaternion representation. Finally, several numerical applications are settled using the proposed Shell-based SPH method to prove its capabilities.

## **3.1 Overview of shell modeling using meshless methods**

In structural modeling, it is well known that one of the most efficient models is the "*shell theory*". A shell structure is a three dimensional continuum which is bounded by two curved surfaces, where the distance between the surfaces is small in comparison with other remaining dimensions. A plate may be regarded as a special limiting case of a shell structure that has no curvatures. Due to their efficient load-carrying capabilities, shell-like structures are undoubtedly the most widely used structural components in modern engineering regions like roofs, cars, tanks, space vehicles, ship hulls, aircraft fuselages, *etc.* As mentioned in [92], modeling these structures with continuum elements would require a minimum of about five elements through the thickness and leads to extremely expensive computations. Furthermore, modeling thin-walled structures with continuum elements often causes elements with high aspect ratios, which would degrade the conditioning of the

equations and the accuracy of the solution. Vignjevic *et al.* [57] performed 3D simulations of hypervelocity impact on fuel tanks using the SPH method and revealed that a minimum of three particles is necessary to be used through the thickness to ensure a good quality of results. Li *et al.* [6] presented a 3D reproducing kernel particle method (RKPM) for large deformation analysis of thin shell structures and 2 or at most 3 particles were placed through the thickness direction to capture the gradient field in thickness.

Therefore, it becomes clear that there is a need for the development of a simple and efficient shell-based SPH method, by discretizing the mid-surface of the shell structure with only one particle through the thickness. To achieve this goal, two types of shell theories are widely used for the modeling of shell structures. One of them, called Kirchhoff-Love shell theory, which does not admit any transverse shear. The approximation functions requires to ensure  $C^1$  continuity. The other one, called Mindlin-Reissner shell theory, which takes into account of the transverse shear and requires only  $C^0$  continuous approximation functions which is generally easy to satisfy.

Experimental results [92] show that the behavior of thin shells ( $t/L \leq 1/20$ ) can be predicted accurately using the Kirchhoff-Love assumptions. But for thicker shells, the Mindlin-Reissner assumptions are more accurate because transverse shear effects become important. Thick shell theory can also be used for thin shells because in this case the transverse shears would approximately vanish.

Since the last twenty years, many meshless methods have been developed for applications involving shell structures by incorporating the above shell theories. The early work can be found in [7]. The EFG method has been applied into thin plates [16] and shells [58] based on Kirchhoff theory and background quadrilateral elements were necessary for the Gaussian numerical integration. The adopted Moving Least-Squares (MLS) approximations generally do not have the Kronecker-delta property which lead to an awkward essential boundary conditions, so that an additional Lagrange multiplier technique was introduced. Noguchi *et al.* [93] extended the original EFG method for the simulation of Mindlin shells and spatial structures. The Meshless Local Petrov-Galerkin (MLPG) method had been used for solving the bending problem of a thin plate based on the Kirchhoff plate theory [94] and numerical analysis of Mindlin shell [60].

First extension of SPH method for shell analysis was utilized for dynamic response analysis of shell structures under impact [95]. As mentioned in [96], MLS shape functions are not interpolation functions, but approximation functions. They do not verify Kronecker's

property which makes it difficult to apply the essential boundary conditions. Moreover the shape function maybe negative which may bring unphysical effect.

The Corrective Smoothed Particle Method (CSPM) [33,71] satisfy the zero and first order consistency conditions completely, which is essential for the Dirichlet and/or von Neumann types of boundary conditions. To our knowledge, this method has been not applied for shell analysis with Mindlin-Reissner theory.

### 3.2 Kinematics of shell structures using SPH discretization

The Reissner-Mindlin theory is adopted to establish an adaptive SPH formulation for shell structures. According to this theory, the shell structure behavior can be represented by using only one layer of particles at the mid-surface (see Figure 3.1). Each particle is endowed with five degrees of freedom: three translations  $\mathbf{u}_L = \{u, v, w\}^T$  and two rotations  $\boldsymbol{\theta}_L = \{\theta, \varphi\}^T$  expressed in the local framework tangent to the shell mid-surface. Passing through a particle, the straight transverse fiber normal to the mid-surface remains straight but not necessarily perpendicular to the mid-surface after deformation. This fiber is called as pseudo-normal vector generally indicated as  $\mathbf{n}$ , especially noted as  $\mathbf{n}_0$  in the initial configuration.

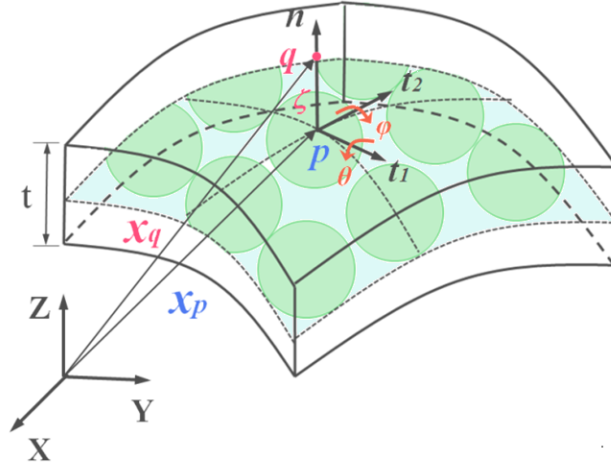


Figure 3.1: Discretization of a shell mid-surface using SPH particles

As for the shell structure of a uniform thickness of  $t$  shown in 3.1, considering any material point  $q$  located at a distance  $\zeta$  from the shell mid-surface, the position vector  $\mathbf{x} = \mathbf{x}_q$  can

be expressed as,

$$\mathbf{x}(\xi, \eta, \zeta) = \mathbf{x}_p(\xi, \eta) + \zeta \mathbf{n}(\xi, \eta) \quad (3.1)$$

where  $\mathbf{x}_p$  is the position vector of point  $p$  which is the perpendicular foot of the fiber on the mid-surface,  $\boldsymbol{\xi} = (\xi, \eta, \zeta)$  is the position vector described in the initial curvilinear coordinates. The displacement vector  $\mathbf{u} = \mathbf{u}_q$  of point  $q$  can be calculated by

$$\mathbf{u}(\xi, \eta, \zeta) = \mathbf{u}_p(\xi, \eta) + \zeta \Delta \mathbf{n}(\xi, \eta) \quad (3.2)$$

where  $\Delta \mathbf{n} = \mathbf{n} - \mathbf{n}_0$ .

Using the Equation (3.1), the particle spacing vector  $d\mathbf{x}$  can be expressed in terms of  $d\boldsymbol{\xi}$ ,

$$d\mathbf{x} = \mathbb{F} d\boldsymbol{\xi} \quad (3.3)$$

where  $\mathbb{F}$  is the deformation gradient tensor relative to initial and current position of the material point  $q$ . It is given by

$$\mathbb{F} = \{\mathbf{a}_{1\zeta}, \mathbf{a}_{2\zeta}, \mathbf{a}_{3\zeta}\} \quad (3.4)$$

in which  $\mathbf{a}_{1\zeta}$  and  $\mathbf{a}_{2\zeta}$  are the covariant basis vectors (see Figure 3.2) calculated from

$$\begin{cases} \mathbf{a}_{1\zeta} = \mathbf{x}_{p,\xi} + \zeta \mathbf{n}_{,\xi} \\ \mathbf{a}_{2\zeta} = \mathbf{x}_{p,\eta} + \zeta \mathbf{n}_{,\eta} \\ \mathbf{a}_{3\zeta} = \mathbf{n} \end{cases} \quad (3.5)$$

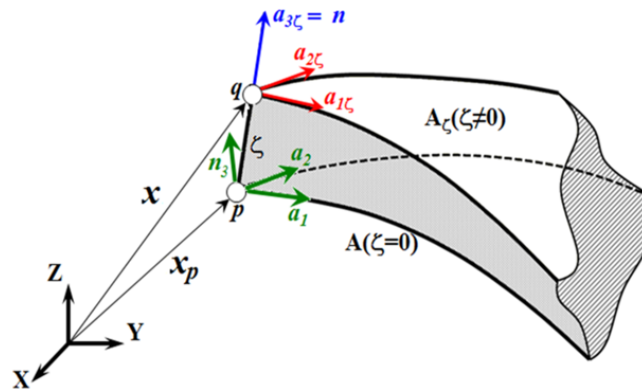


Figure 3.2: Position vectors and covariant basis in the deformed configuration

A local current curvilinear system for the point at the mid-surface ( $\zeta = 0$ ) can be described by an orthogonal matrix  $\mathbb{Q} = [\mathbf{t}_1; \mathbf{t}_2; \mathbf{n}_3]$ . The unit vector normal  $\mathbf{n}_3$  to the current covariant

basis  $\mathbf{a}_1 = \mathbf{a}_{1\zeta}(\zeta = 0)$  and  $\mathbf{a}_2 = \mathbf{a}_{2\zeta}(\zeta = 0)$  can be computed by

$$\mathbf{n}_3 = \frac{\mathbf{a}_1 \times \mathbf{a}_2}{|\mathbf{a}_1 \times \mathbf{a}_2|} \quad (3.6)$$

Therefore, the transformation orthogonal matrix from the global Cartesian framework to the local current coordinates is calculated following the book of Batoz and Dhatt [97]

$$\mathbb{Q} = \begin{bmatrix} \beta + \frac{1}{1+\beta}n_{3y}^2 & -\frac{1}{1+\beta}n_{3x}n_{3y} & n_{3x} \\ -\frac{1}{1+\beta}n_{3x}n_{3y} & \beta + \frac{1}{1+\beta}n_{3x}^2 & n_{3y} \\ -n_{3x} & -n_{3y} & n_{3z} \end{bmatrix} \quad (3.7)$$

where  $\beta = \mathbf{n}_3 \cdot \mathbf{k}$  and  $\mathbf{k}$  is the unit vector along the global  $z$ -axis. Particularly in the initial configuration, the transformation matrix is marked as  $\mathbb{Q}_0$ . Especially when  $1 + \beta = 0$ , in other word  $\mathbf{n}_3 = -\mathbf{k}$ ,

$$\mathbb{Q} = \begin{bmatrix} 1 & 0 & 0 \\ 0 & -1 & 0 \\ 0 & 0 & -1 \end{bmatrix} \quad (3.8)$$

Then the Green-Lagrangian (GL) strain tensor  $\mathbb{E}$  expressed in the initial curvilinear coordinate framework

$$\mathbb{E} = \frac{1}{2}(\mathbb{L} + \mathbb{L}^T + \mathbb{L}^T\mathbb{L}) \quad (3.9)$$

where  $\mathbb{L}$  is the displacement gradient tensor herein can be obtained by

$$\mathbb{L} = \frac{\partial \mathbf{u}}{\partial \boldsymbol{\xi}} = \begin{bmatrix} u_{p,\xi} + \zeta \Delta n_{x,\xi} & u_{p,\eta} + \zeta \Delta n_{x,\eta} & \Delta n_x \\ v_{p,\xi} + \zeta \Delta n_{y,\xi} & v_{p,\eta} + \zeta \Delta n_{y,\eta} & \Delta n_y \\ w_{p,\xi} + \zeta \Delta n_{z,\xi} & w_{p,\eta} + \zeta \Delta n_{z,\eta} & \Delta n_z \end{bmatrix} \quad (3.10)$$

In order to calculate the Euler strain tensor  $\varepsilon$  directly in the current curvilinear coordinate system, one has to define the following tensor

$$\mathbb{G} = \mathbb{F}^{-1} \mathbb{Q}_0 \quad (3.11)$$

hence we obtain

$$\varepsilon = \mathbb{Q}\mathbb{G}^T \mathbb{E} \mathbb{G}\mathbb{Q}^T \quad (3.12)$$

For the study of shell structures, it is often convenient to separate the GL strain components into three physical contributions: constant membrane strains  $\mathbf{E}_m$ , linear bending strains  $\zeta \mathbf{E}_b$  and constant shear strains  $\mathbf{E}_s$ . In the present investigation, thickness stretching is

not considered, therefore the remaining non-zero strains are the in-plane and the shearing strain components.

The constant membrane strain components can be expressed in function of the displacements by

$$\begin{aligned} \mathbf{E}_m &= \begin{Bmatrix} E_{m11} \\ E_{m22} \\ 2E_{m12} \end{Bmatrix} \\ &= \begin{Bmatrix} u_{p,\xi} + (u_{p,\xi}^2 + v_{p,\xi}^2 + w_{p,\xi}^2) / 2 \\ v_{p,\eta} + (u_{p,\eta}^2 + v_{p,\eta}^2 + w_{p,\eta}^2) / 2 \\ u_{p,\eta} + v_{p,\xi} + u_{p,\xi} u_{p,\eta} + v_{p,\xi} v_{p,\eta} + w_{p,\xi} w_{p,\eta} \end{Bmatrix} \end{aligned} \quad (3.13)$$

The GL curvature components of  $\mathbf{E}_b$  are

$$\begin{aligned} \mathbf{E}_b &= \begin{Bmatrix} E_{b11} \\ E_{b22} \\ 2E_{b12} \end{Bmatrix} \\ &= \begin{Bmatrix} \Delta n_{x,\xi} + u_{p,\xi} \Delta n_{x,\xi} + v_{p,\xi} \Delta n_{y,\xi} + w_{p,\xi} \Delta n_{z,\xi} \\ \Delta n_{y,\eta} + u_{p,\eta} \Delta n_{x,\eta} + v_{p,\eta} \Delta n_{y,\eta} + w_{p,\eta} \Delta n_{z,\eta} \\ \Delta n_{x,\eta} + \Delta n_{y,\xi} + u_{p,\xi} \Delta n_{x,\eta} + u_{p,\eta} \Delta n_{x,\xi} + v_{p,\xi} \Delta n_{y,\eta} + v_{p,\eta} \Delta n_{y,\xi} + w_{p,\xi} \Delta n_{z,\eta} + w_{p,\eta} \Delta n_{z,\xi} \end{Bmatrix} \end{aligned} \quad (3.14)$$

According to the Reissner-Mindlin shell theory, the transverse shear strain components are constant through the thickness, they are given by

$$\begin{aligned} \mathbf{E}_s &= \begin{Bmatrix} 2E_{s13} \\ 2E_{s23} \end{Bmatrix} \\ &= \begin{Bmatrix} \Delta n_x + w_{p,\xi} + u_{p,\xi} \Delta n_x + v_{p,\xi} \Delta n_y + w_{p,\xi} \Delta n_z \\ \Delta n_y + w_{p,\eta} + u_{p,\eta} \Delta n_x + v_{p,\eta} \Delta n_y + w_{p,\eta} \Delta n_z \end{Bmatrix} \end{aligned} \quad (3.15)$$

Consequently, the Euler strain  $\boldsymbol{\varepsilon}$  can also be separated into three parts: membrane strain  $\boldsymbol{\varepsilon}_m$ , bending strain  $\zeta \boldsymbol{\varepsilon}_b$  and transverse shearing one  $\boldsymbol{\gamma}$ . Thanks to the engineering notation, the strain is stated as

$$\boldsymbol{\varepsilon} = \boldsymbol{\varepsilon}_m + \zeta \boldsymbol{\varepsilon}_b + \boldsymbol{\gamma} \quad (3.16)$$



### 3.3 Constitutive relations and dynamic equilibrium equations

Based on the plane stress assumption built up in the current curvilinear basis, the membrane stress  $\boldsymbol{\sigma}_m$ , the bending stress  $\boldsymbol{\sigma}_b$  and the transverse shear stress  $\boldsymbol{\sigma}_s$  can be calculated using the elastic constitutive relationship

$$\begin{aligned} \boldsymbol{\sigma}_m &= \mathbb{H}\boldsymbol{\varepsilon}_m \\ \boldsymbol{\sigma}_b &= \zeta\mathbb{H}\boldsymbol{\varepsilon}_b \quad , \quad \mathbb{H} = \frac{E}{1-\nu^2} \begin{bmatrix} 1 & \nu & 0 \\ \nu & 1 & 0 \\ 0 & 0 & (1-\nu)/2 \end{bmatrix} \\ \boldsymbol{\sigma}_s &= kG\boldsymbol{\gamma} \end{aligned} \quad (3.17)$$

where  $G = E/2(1 + \nu)$  is the tangent shear modulus. A constant  $k$  has been added here to account for the fact that the shear stresses are not constant across the section. A value of  $k = 5/6$  is exact for a rectangular, homogeneous section and corresponds to a parabolic shear stress distribution [97,98]. Integrating these stress components through the thickness, one can get the resultant membrane force  $\mathbf{N}$ , bending moment  $\mathbf{M}$  and shear force  $\mathbf{T}$ .

$$\left\{ \begin{aligned} \mathbf{N} &= \int_{-t/2}^{t/2} \boldsymbol{\sigma}_m d\zeta = t\mathbb{H}\boldsymbol{\varepsilon}_m \\ \mathbf{M} &= \int_{-t/2}^{t/2} \boldsymbol{\sigma}_b d\zeta = \frac{t^3}{12}\mathbb{H}\boldsymbol{\varepsilon}_b \\ \mathbf{T} &= \int_{-t/2}^{t/2} \boldsymbol{\sigma}_s d\zeta = tkG\boldsymbol{\gamma} \end{aligned} \right. \quad (3.18)$$

The classical equilibrium equations for the shell-like structure, subjected to an external load  $\mathbf{b}_L = \{b_\xi, b_\eta, b_\zeta\}^T$ , can be expressed in a strong form using the previous generalized forces  $\mathbf{N}$ ,  $\mathbf{M}$  and  $\mathbf{T}$

$$\left\{ \begin{aligned} \rho_m \ddot{u} &= N_{\xi\xi,\xi} + N_{\xi\eta,\eta} + b_\xi \\ \rho_m \ddot{v} &= N_{\xi\eta,\xi} + N_{\eta\eta,\eta} + b_\eta \\ \rho_m \ddot{w} &= T_{\xi\zeta,\xi} + T_{\eta\zeta,\eta} + b_\zeta \\ \rho_b \ddot{\theta} &= -M_{\xi\eta,\xi} - M_{\eta\eta,\eta} + T_{\eta\zeta} \\ \rho_b \ddot{\varphi} &= M_{\xi\xi,\xi} + M_{\xi\eta,\eta} - T_{\xi\zeta} \end{aligned} \right. \quad (3.19)$$

in which

$$\rho_m = \int_{-t/2}^{t/2} \rho d\zeta = t\rho \quad \text{and} \quad \rho_b = \int_{-t/2}^{t/2} t\rho d\zeta = \frac{t^3}{12}\rho \quad (3.20)$$

The balance equations can be described in a simple matrix form

$$\left\{ \begin{aligned} \rho_m \ddot{\mathbf{u}}_L &= \text{div}_L \mathbb{N}_L + \mathbf{b}_L \\ \rho_b \ddot{\boldsymbol{\theta}}_L &= \text{div}_L \mathbb{M}_L + \mathbf{T}_L \end{aligned} \right. \quad (3.21)$$

where

$$\mathbb{N}_L = \begin{bmatrix} N_{\xi\xi} & N_{\xi\eta} & T_{\xi\zeta} \\ N_{\xi\eta} & N_{\eta\eta} & T_{\eta\zeta} \\ T_{\xi\zeta} & T_{\eta\zeta} & 0 \end{bmatrix}, \quad \mathbb{M}_L = \begin{bmatrix} -M_{\xi\eta} & -M_{\eta\eta} & 0 \\ M_{xx} & M_{\xi\eta} & 0 \\ 0 & 0 & 0 \end{bmatrix} \quad \text{and} \quad \mathbf{T}_L = \begin{Bmatrix} T_{\eta\zeta} \\ -T_{\xi\zeta} \\ 0 \end{Bmatrix}. \quad (3.22)$$

### 3.4 SPH implementation for shell structures

As mentioned in Chapter 2, in the Total Lagrangian SPH method, the search procedure for the neighboring particles and the determination of the kernel function  $W_0(\xi, \eta)$  are performed in the initial coordinate system. Then the derivatives of the kernel function with respect to the local basis  $\partial W_0 / \partial \boldsymbol{\xi} = (\partial W_0 / \partial \xi, \partial W_0 / \partial \eta, \partial W_0 / \partial \zeta \equiv 0)$  are calculated. Directly substituting the (3.4), (3.5), (3.13)-(3.15) into the Total Lagrangian SPH formulations, we can obtain the deformation gradient tensor  $\mathbb{F}$ , GL strain tensor  $\mathbb{E}$ . Therefore, the Eulerian strain tensor  $\boldsymbol{\varepsilon}$  and the generalized force vectors  $\mathbf{N}$ ,  $\mathbf{M}$  and  $\mathbf{T}$  can be evaluated using the (3.18).

To construct the discretized linear and angular momentum conservation equations by the Total Lagrangian SPH formulations, the Equation (3.21) needs to be firstly rewritten in the global coordinate system,

$$\begin{cases} \rho_{m0} \ddot{\mathbf{U}} = \text{DIV} \mathbf{N}_0 + \mathbf{b}_0 \\ \rho_{b0} \ddot{\boldsymbol{\Theta}} = \text{DIV} \mathbf{M}_0 + \mathbf{T}_0 \end{cases} \quad (3.23)$$

where

$$\begin{aligned} \mathbf{N}_0 &= J \mathbf{Q}^T \mathbb{N}_L \mathbf{Q} \mathbf{G}^T \\ \mathbf{M}_0 &= J \mathbf{Q}^T \mathbb{M}_L \mathbf{Q} \mathbf{G}^T \\ \mathbf{T}_0 &= J \mathbf{Q}^T \mathbf{T}_L \\ \mathbf{b}_0 &= J \mathbf{Q}^T \mathbf{b}_L \end{aligned} \quad (3.24)$$

and

$$\rho_{m0} = \int_{-t/2}^{t/2} \rho_0 d\zeta = t \rho_0, \quad \rho_{b0} = \int_{-t/2}^{t/2} t \rho_0 d\zeta = \frac{t^3}{12} \rho_0 \quad (3.25)$$

Therefore the discretized form for particle  $i$  is

$$\ddot{\mathbf{U}}_i = \sum_{j=1}^{N_j} \left( \frac{\mathbf{N}_{0i}}{\rho_{m0i}^2} + \frac{\mathbf{N}_{0j}}{\rho_{m0j}^2} \right) \nabla_0 W_{0ij} \rho_{m0j} A_{0j} + \frac{\mathbf{b}_{0i}}{\rho_{m0i}} \quad (3.26)$$

$$\ddot{\boldsymbol{\Theta}}_i = \sum_{j=1}^{N_j} \left( \frac{\mathbf{M}_{0i}}{\rho_{b0i}^2} + \frac{\mathbf{M}_{0j}}{\rho_{b0j}^2} \right) \nabla_0 W_{0ij} \rho_{b0j} A_{0j} + \frac{\mathbf{T}_{0i}}{\rho_{b0i}} \quad (3.27)$$

Noting that the original artificial viscosity is composed for the continuum mechanics, it has to be reconstituted for the shell modeling. The new viscosity is established for each particle link  $i - j$  and can be separated into two parts: membrane and shearing viscous forces [83]. The in-plane part is given by

$$\mathbb{S}_{vij} = \frac{-\alpha_{\Pi} \bar{c}_{ij} \phi_{ij} + \beta_{\Pi} \phi_{ij}^2}{\bar{\rho}_{mij}} \begin{bmatrix} 1 & 0 & 0 \\ 0 & 1 & 0 \\ 0 & 0 & 0 \end{bmatrix} \quad \phi_{ij} < 0 \quad (3.28)$$

and the transversal part is

$$\mathbb{T}_{vij} = \frac{-\gamma_{\Pi} \bar{c}_{ij} \psi_{ij}}{\bar{\rho}_{mij}} \begin{bmatrix} 0 & 0 & 1 \\ 0 & 0 & 1 \\ 1 & 1 & 0 \end{bmatrix} \quad \psi_{ij} < 0 \quad (3.29)$$

where

$$\begin{aligned} \phi_{ij} &= \frac{h_{ij} [(v_{xi} - v_{xj})(x_i - x_j) + (v_{yi} - v_{yj})(y_i - y_j)]}{|\mathbf{x}_{ij}|^2 + 0.01h_{ij}^2} \\ \psi_{ij} &= \frac{h_{ij}(v_{zi} - v_{zj})(z_i - z_j)}{|\mathbf{x}_{ij}|^2 + 0.01h_{ij}^2} \end{aligned} \quad (3.30)$$

and  $\gamma_{\Pi}$  is selected to be 0.1.

Then the viscous force acting from particle  $j$  on the particle  $i$  can be expressed with the respect to the global basis,

$$\mathbb{N}_{vij} = J_i \mathbb{Q}_i^T (\mathbb{S}_{vij} + \mathbb{T}_{vij}) \mathbb{Q}_i \mathbb{G}_i^T \quad (3.31)$$

Finally, the the linea rdynamic equilibrium equation Equation (3.26) including the artificial viscosity takes the following form

$$\ddot{\mathbf{U}}_i = \sum_{j=1}^{N_j} \left( \frac{\mathbb{N}_{0i}}{\rho_{m0i}^2} + \frac{\mathbb{N}_{0j}}{\rho_{m0j}^2} - \mathbb{N}_{vij} \right) \nabla_0 W_{0ij} \rho_{m0j} \mathbf{A}_{0j} + \frac{\mathbf{b}_{0i}}{\rho_{m0i}} \quad (3.32)$$

### 3.5 Treatment of large rotations of shells using the SPH method

One of the central issue in the development of nonlinear shell-based SPH algorithm is the treatment of 3D finite rotations. Normally, finite rotations are represented through an orthogonal tensor  $\mathbb{R}$  which is an element of the  $SO(3)$  rotation group. It can be described by a rotation vector  $\Theta$  thanks to the Rodrigues formula [97, 99],

$$\mathbb{R}(\Theta) = \exp[\hat{\Theta}] = \cos \Theta \mathbb{I}_3 + \frac{\sin \Theta}{\Theta} \hat{\Theta} + \frac{1 - \cos \Theta}{\Theta^2} \Theta \otimes \Theta \quad (3.33)$$

where  $\Theta$  is the norm of the rotation vector;  $\mathbb{I}_3$  is the identity matrix in three-dimension;  $\hat{\Theta}$  is the skew-symmetric matrix associated with the rotation vector  $\Theta$  defined by  $\hat{\Theta} = \Theta \times \mathbb{I}_3$ . This parameterization does not lead to a global acceptable solution, suffering from ill-conditioning problem when  $\Theta$  is in the neighborhood of  $2\pi$  [100].

Another popular rotation representation namely quaternion parameters  $\{q_0, \mathbf{q}\}$  [87, 100] are defined

$$q_0 = \cos \frac{\Theta}{2}, \quad \mathbf{q} = \frac{\Theta}{\Theta} \sin \frac{\Theta}{2} \quad (3.34)$$

The rotation tensor  $\mathbb{R}$  (3.33) is expressed in terms of  $\{q_0, \mathbf{q}\}$  as

$$\mathbb{R} = (2q_0^2 - 1)\mathbb{I}_3 + 2q_0\mathbf{q} \times \mathbb{I}_3 + 2\mathbf{q} \otimes \mathbf{q} \quad (3.35)$$

The update procedure of the quaternions and the rotation matrix is established on the base of the rotation increment vector  $\Delta\Theta$  which is obtained by integrating the angular accelerations (3.27) on time. The quaternion parametrization associated with the increment of rotations is computed

$$\{q_0^\Delta, \mathbf{q}^\Delta\} = \left\{ \cos \frac{\Delta\Theta}{2}, \frac{\Delta\Theta}{\Delta\Theta} \sin \frac{\Delta\Theta}{2} \right\} \quad (3.36)$$

If the quaternions  $\{q_0^{n-1}, \mathbf{q}^{n-1}\}$  at the last time step  $n-1$  has been known, the quaternions  $\{q_0^n, \mathbf{q}^n\}$  at the current time step  $n$  can be updated from

$$\{q_0^n, \mathbf{q}^n\} = \{q_0^{n-1}q_0^\Delta - \mathbf{q}^{n-1}\mathbf{q}^\Delta, q_0^{n-1}\mathbf{q}^\Delta + q_0^\Delta\mathbf{q}^{n-1} + \mathbf{q}^\Delta \times \mathbf{q}^{n-1}\} \quad (3.37)$$

Therefore, the rotation matrix  $\mathbb{R}^n$  at the next step can be renewed using the Equation (3.35). The pseudo-normal vector  $\mathbf{n}$  is updated using the novel rotation matrix

$$\mathbf{n}^n = \mathbb{R}^n \mathbf{n}^0 \quad (3.38)$$

In order to limit the irregular behavior of the pseudo-normal vectors of particles located on the shell edges, each normal needs to be regularized by a special filter [75].

$$\mathbf{n}'_i = \mathbf{n}_i + \alpha_n \left( \frac{\sum_{j=1}^{N_j} \mathbf{n}_j W_{0ij} A_{0j}}{\sum_{j=1}^{N_j} W_{0ij} A_{0j}} - \mathbf{n}_i \right) \quad (3.39)$$

where  $\mathbf{n}'$  is the regularized pseudo-normal vector and  $\alpha_n$  is a filter, where it has been shown that 0.01 is a suitable value.

As a summary, Figure 3.3 shows the flow chart of calculation procedure using the proposed shell-based SPH model.

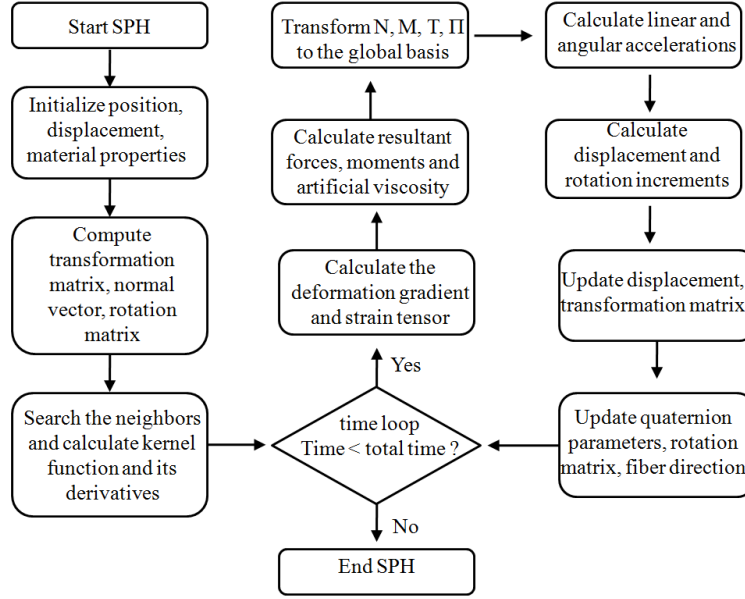


Figure 3.3: Flow chart of the present shell-based SPH method

## 3.6 Numerical applications

In this section, several numerical applications will be investigated using the present shell-based SPH formulation together with the explicit dynamics time integration scheme. The capabilities and efficiency will be shown by comparing the obtained results with the reference values taken from the literature and the solution of well-known FE softwares LS-DYNA<sup>©</sup> using its SPH module and ABAQUS<sup>©</sup> finite element code.

### 3.6.1 Large deflection of cantilever beam under transverse loads

This application deals with the geometrically nonlinear analysis of a clamped beam made of steel as shown in Figure 3.4. The geometric and the material properties are as follows: beam length  $L = 100mm$ , width/thickness  $b = t = 10mm$ , Young's modulus  $E = 210GPa$ , Poisson's ratio  $\nu = 0.3$ , density  $\rho = 7800kg/m^3$ . The beam left side is clamped while a set of transversal load increments are applied on the right free end starting from 0 to  $175kN$  (to satisfy the loading factor  $PL^2/EI$  ranging from 0 to 10).

The beam mid-surface is discretized using only one layer of  $50 \times 5$  particles in the shell-based SPH method, where intermediate deformed configurations are shown in Figure 3.4. The final deflection obtained using the present SPH method is of  $80.09mm$ , which is very close to the analytical solution of Timoshenko [82] with an error of only 1.25%.

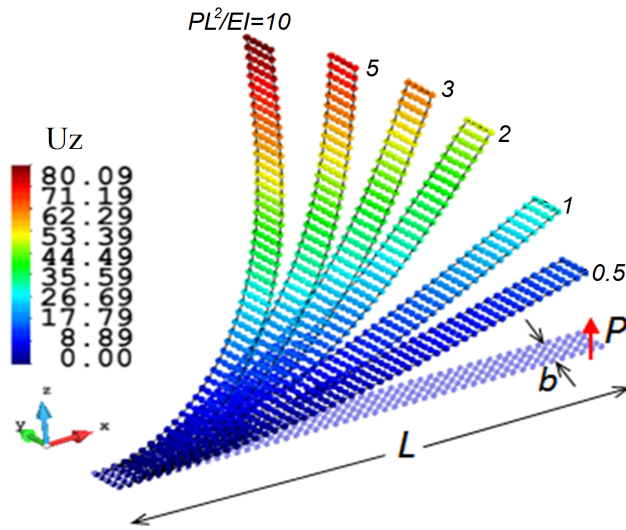


Figure 3.4: Initial and deformed configurations of the clamped beam

Table 3.1: Comparison of the SPH results with Timoshenko reference solution [82]

P (kN)	$PL^2/EI$	Analytical(mm)	SPH model(mm)	Error (%)
0	0	0	0	—
4.375	0.25	8.3	8.1	-2.41
8.75	0.5	16.2	15.94	-1.6
13.125	0.75	23.5	23.33	-0.72
17.5	1	30.2	30.1	-0.33
35	2	49.4	50.22	1.66
52.5	3	60.3	61.37	1.77
70	4	67.0	67.59	0.88
87.5	5	71.4	71.41	0.01
105	6	74.4	74.03	-0.5
122.5	7	76.7	76.01	-0.9
140	8	78.5	77.6	-1.15
157.5	9	79.9	78.94	-1.2
175	10	81.1	80.09	-1.25

The results of plate end deflection obtained using the present Shell-based SPH formulation are listed in Table 3.1 and compared to the analytical solution of Timoshenko [82].

As we can remark that the maximal error of the present SPH solution is less than 2.5%, even if with a coarse discretization of only one layer of  $50 \times 5$  particles. The load-deflection curve is also depicted in Figure 3.5, which shows the nonlinear character of the beam undergoing very large displacement 80% of its length. We can observe that the obtained loading path is in very good agreement with the analytical solution of Timoshenko.

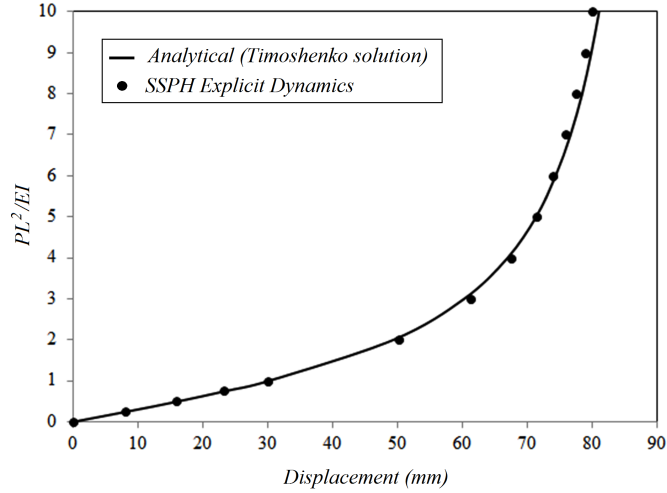


Figure 3.5: Comparison of load-displacement curve (Present SPH model vs. Analytical solution)

In order to evaluate the efficiency and the accuracy of the proposed shell-based SPH method, the same structure has been modeled using the classical continuum SPH available in LS-DYNA<sup>©</sup> code [85]. The analysis is conducted using the Explicit Dynamics scheme for the numerical resolution in both methods (LS-DYNA<sup>©</sup> and the present shell-based SPH), and the total time is fixed to  $5ms$  while the load is increased linearly until reaching its maximum value of  $175kN$ . Different SPH continuum models exist in LS-DYNA<sup>©</sup> and the one which has been used is based on the TLF (Form 7).

In order to achieve the quasi-static solution, a mass damping has been included as  $\mathbb{C} = 4\mathbb{M}$ . Three discretizations of the beam in three dimensions are used in LS-DYNA<sup>©</sup> corresponding to:  $50 \times 5 \times 5$ ,  $80 \times 8 \times 8$ ,  $100 \times 10 \times 10$ . A summary of the computation time for all models using a personal computer with a CPU of  $2.5Ghz$  and a RAM of  $6Gb$  is listed in Table 3.2.

From Table 3.2, we can observe that the proposed shell-based SPH method is more efficient in computing time when compared to the classical continuum SPH model. The evolution

Table 3.2: Comparison of CPU time for analysis of the beam (Present SPH vs. Continuum SPH)

Model	Present SPH model	LS-DYNA <sup>©</sup>		
	$50 \times 5$	$50 \times 5 \times 5$	$80 \times 8 \times 8$	$100 \times 10 \times 10$
CPU time (s)	21	55	425	1131

of the deflection at the right end central point are depicted in Figure 3.6, where we can remark that convergence of the classical continuum SPH is very slow compared to the proposed SPH method.

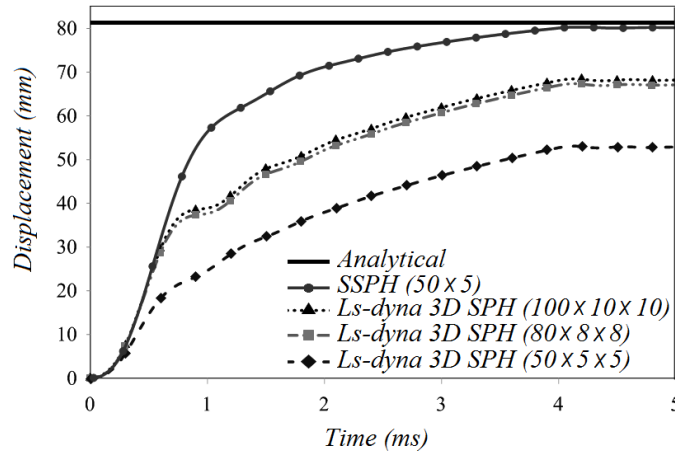


Figure 3.6: Evolution of the deflection over time at the right end section

As we can observe, the maximal deflections obtained using the classical 3D SPH models of LS-DYNA<sup>©</sup> correspond to:  $52.96mm$ ,  $67.15mm$  and  $68.12mm$  respectively, which are far from the analytical reference value given by Timoshenko  $81.1mm$ , with the errors of 34.7%, 17.2% and 16%. The present comparison shows that the proposed SPH method is more accurate than the classical 3D SPH method. Figure 3.7 shows comparison of the final deformed shape of the structure obtained by the classical continuum SPH models of LS-DYNA<sup>©</sup> and the one-layer particles at the mid-surface using the shell-based SPH method.

### 3.6.2 Roll-up of a clamped plate

This benchmark represents a clamped plate under a bending moment applied at its free end. The analytical solution is given by the classical Euler formula [101]  $\kappa = M/EI$ , where  $\kappa$  is curvature and  $M$  is the bending moment. The plate geometrical and material



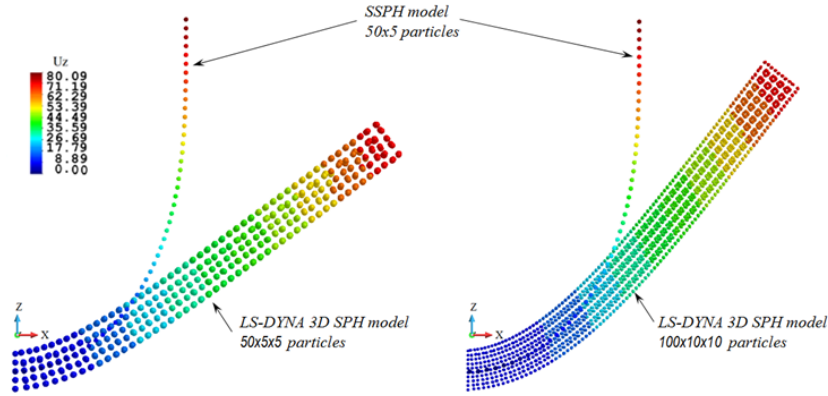


Figure 3.7: Comparison of deformed configurations of the beam at maximum load(present SPH vs. LS-DYNA<sup>®</sup>)

properties are as follows: length  $L = 10cm$ , width/thickness  $b = t = 1cm$ , Young’s modulus  $E = 1200N/cm^2$ , Poisson’s ratio  $\nu = 0$ . For the chosen properties, the values of the bending moment which transforms the plate into a full-circle shape is  $M = 2\pi EI/L = 20\pi$ .

The plate has been discretized using only one layer of  $50 \times 5$  particles in the Shell-based SPH method, where intermediate deformed configurations are shown in Figure 3.8. For comparison purpose, the same plate has been modeled using ABAQUS<sup>®</sup> code with a FE mesh of  $50 \times 5$  S4R shell elements.

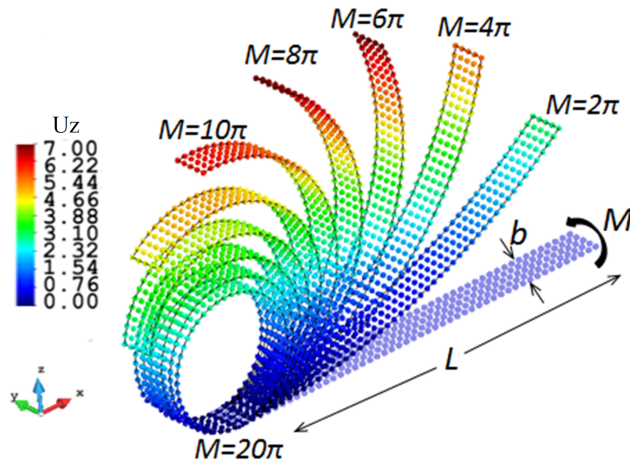


Figure 3.8: Initial and intermediate configurations.using the present SPH method

The results of beam free end vertical  $W$  and horizontal  $U$  displacements obtained using the present shell-based SPH formulation are depicted in Figure 3.9 and compared to the FE

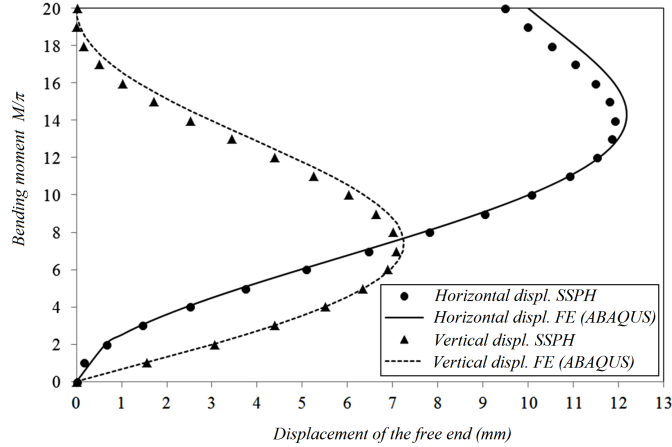


Figure 3.9: Comparison of load-displacement curve (Present SPH *vs.* FEM)

solution of ABAQUS<sup>®</sup>. As we can observe, the loading path obtained using the present SPH method shows the very nonlinear behavior of the solution due to the very large rotation up to  $2\pi$ . The predicted solution using the developed Shell-based SPH formulation is very close to the FE loading path predicted using ABAQUS<sup>®</sup> code, even if we use a coarse discretization of one layer of  $50 \times 5$  particles. This demonstrates the capability and the efficiency of the present method compared to the FEM and we can clearly say that the proposed Shell-based SPH method can represent a promising alternative to the classical FEM.

### 3.6.3 Large deformation of a square plate under uniform load

This application concerns a square plate subjected to a uniform transverse pressure with various boundary conditions. The geometry of the structure is shown in Figure 3.10(a) with the following material properties: Young's modulus  $E = 53779.1 \text{ MPa}$ , Poisson's ratio  $\nu = 0.3$  and material density of  $1600 \text{ kg/m}^3$ . The plate supports a uniformly distributed load of intensity  $q_0$  as shown in Figure 3.10(a).

Two types of boundary conditions denoted by *SS1* and *SS3* are considered :

- *SS1* :  $u = w = \theta_y = 0$  for edges parallel to  $x$ -axis  
 $v = w = \theta_x = 0$  for edges parallel to  $y$ -axis
- *SS3* :  $u = v = w = 0$  for all edges

Due to symmetry of the problem, only a quarter of the plate was modeled using a uniform discretization of  $21 \times 21$  SPH particles. The loading control technique was employed to solve the nonlinear deflection problem and the total distributed load was applied gradually fol-

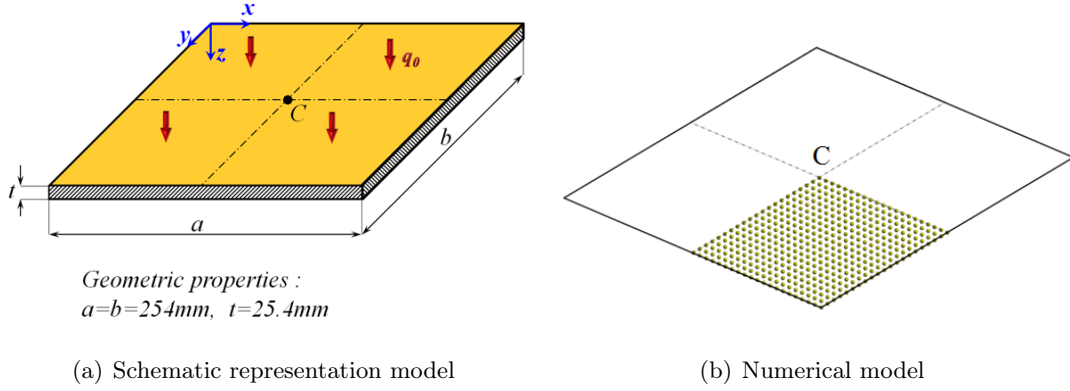


Figure 3.10: Geometry of the square plate under a uniform load

lowing the formula:  $q_0 = \bar{P}E(h/a)^4$ , where the loading factor  $\bar{P}$  was increased linearly from 0 to 200 according to the following values  $\{6.25, 12.5, 25, 50, 75, 100, 125, 150, 175, 200\}$ .

The nonlinear analysis was carried out using the explicit dynamics scheme with a total time of 10 ms. The deflection  $w_C$  at the central point  $C$  of the plate is analyzed as a non-dimensional form of  $\bar{w} = w_C/t$  for both two cases. Figure 3.11 shows the normalized deflection variation in function of the loading factor  $\bar{P}$ , where we can observe the good quality of the predicted results using the present shell-based SPH model when compared to the reference solution [102]. The second case ( $SS3$ ) presents more restrained edges than in  $SS1$ , consequently the produced deflection is lower. A first analysis of the  $SS1$  configuration shows that the maximum error of the present model is about 2.24% at the maximal applied load. While in the second configuration ( $SS3$ ), the error is increased to 9.27% compared to the reference solution. This increase of error in the second configuration can be explained by the presence of more membrane effects because all edges are pinned in 3 directions, and hence more particles will be needed to capture local variations of curvatures in the plate especially close to the plate edges.

From Figure 3.11, one can also remark that the plate behavior starts linearly for low applied loads ( $\bar{P} < 12.5$ ) where pure bending behavior applies, in this branch of the curve the predicted solution of the present shell-based SPH model is identical to the reference solution [102]. As the load increases, the nonlinearities involved became more important, which implies that the bending-stretching coupling effects turns to be more pronounced. Therefore, the stiffness of the plate increases and the deflection augments slowly in contrast with the classical one predicted by the linear theory.

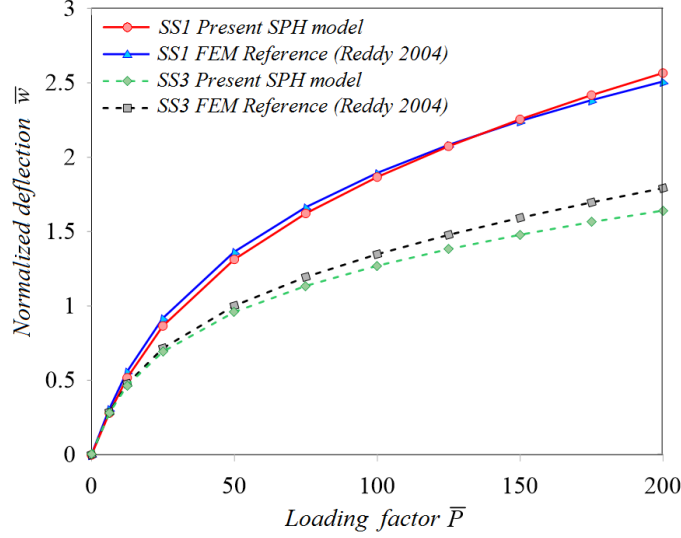


Figure 3.11: Load-deflection curves of the square plate

### 3.6.4 Post-buckling of the Euler column

The application herein considers the popular benchmark of Euler column buckling where an analytical solution is available which will be used to evaluate the performance of the present shell-based SPH model. The geometrical data of the Euler column are: column length  $L = 200mm$ , column width  $b = 10mm$  and column thickness  $t = 5mm$  (Figure 3.12(a)). The column is made of an elastic material with a Young's modulus  $E = 210GPa$ , a Poisson's ratio  $\nu = 0.3$  and a density  $\rho = 7800kg/m^3$ . The boundary conditions of the present structure, corresponds to a built-in column where both translational and rotational degrees are restrained (see Figure 3.12(a)).

Under a large enough compressive axial loading (in the  $x$ -direction), this ideal straight column will buckle when a small transverse perturbation force is applied at the central point of the column in  $z$ -direction (see Figure 3.12(a)). This elastic buckling (Euler buckling) phenomenon is a famous instability problem in classical elasticity. The critical buckling load for this problem was firstly derived by Euler [103]  $P_{cr}^{Exact} = 4\pi^2 EI/L^2 = 21.59kN$ . For clarity reasons, in what follows, all numerical values obtained for critical buckling loads will be normalized using the Euler exact buckling value ( $\bar{P}_{cr} = P_{cr}/P_{cr}^{Exact}$ ), therefore the normalized exact critical load will be  $\bar{P}_{cr}^{Exact} = 1$ .

For symmetry reason, only one-half of the column was modeled, using a uniform  $51 \times 5$  particles distribution (see Figure 3.12(b)). A displacement control technique was applied during a total simulation time of  $30ms$  to reach a maximum axial displacement of  $u_x =$

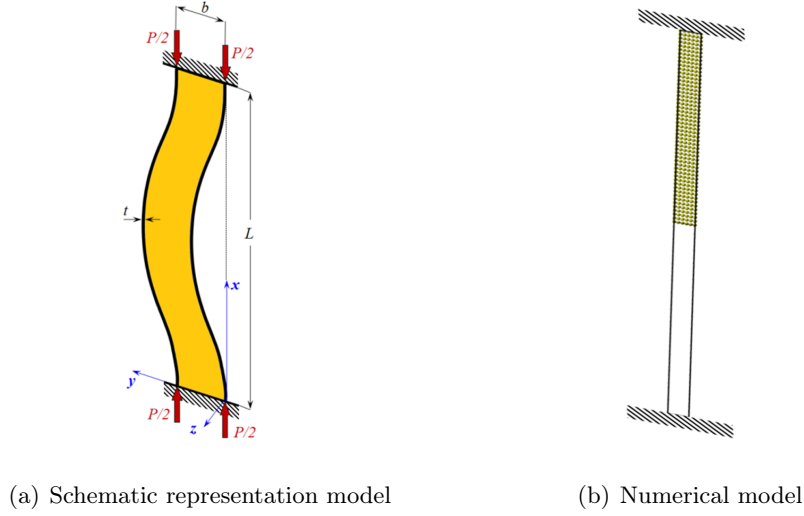


Figure 3.12: Built-in Euler column buckling

–150mm on the loaded edge of the column. A small perturbation load of  $P_z = 5N$  is applied initially at the central point of the column in the transversal  $z$ -direction; this perturbation force is decreased gradually in time until it vanished at the end of calculation. The numerical resolution of the nonlinear resulting problem is done using the explicit dynamics scheme without considering the self-contact effect. The same half-column was also analyzed by the FEM, where a uniform shell mesh of  $50 \times 5$  S4R elements were used in ABAQUS<sup>©</sup> and the Static Implicit scheme is employed for the nonlinear resolution. The FEM solution was considered as a reference for the evaluation of the post-buckling response of the proposed shell-based SPH model. Because the shell FE models are sensitive to the mesh density and in order to perform an objective comparison, the Bernoulli exact nonlinear beam theory was also derived and used for the present application in order to assess the performance of the proposed shell-based SPH model. The numerical results regarding the variation of the normalized axial compression load in function of the transversal deflection of the central point of the column are reported in Figure 8.

The normalized critical buckling load predicted using the present shell-based SPH model is  $\bar{P}_{cr}^{Exact} = 0.901$ , while the corresponding normalized buckling load obtained by the S4R shell element of ABAQUS<sup>©</sup> is  $\bar{P}_{cr}^{FEM} = 1.072$ . The exact beam theory gave a normalized critical buckling value  $\bar{P}_{cr}^{Beam} = 0.945$ . From Figure 3.13, we can observe that the nonlinear post-buckling response of the column has been predicted accurately by the present shell-based SPH model, where the overall SPH solution is closer to the exact beam theory than the shell FEM solution. A summary of the predicted normalized critical values with their

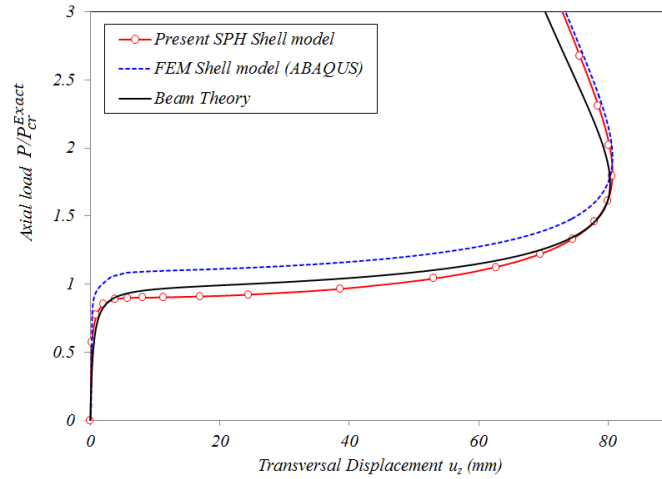


Figure 3.13: Evolution of the normalized axial load in function of the mid column transversal displacement

corresponding errors with respect to the analytical solution are given in Table 3.3.

Table 3.3: Summary of the principal results of the built-in Euler column

	Exact	Beam theory	Shell FEM	Shell SPH
Normalized Critical load	1.000	0.945	1.072	0.901
Error (%)	—	-5.51	7.23	-9.91

As we can observe from Table 1, the present shell-based SPH model underestimates the critical buckling load with a small error of 9.91%. As expected the exact beam theory predicts the solution with good accuracy with 5.51% error. The amount of error of the shell-based SPH model is reasonable since it presents an error of the same range as the one of FEM solution (7.23%). The amount of error depends on the density of particles used. Several numerical tests using different finer discretizations showed that this error decreases when particle density increase.

A generalized analysis of the post-buckling response of the Euler built-in column is given in Figure 3.14, where three deformed configurations are shown at three different times (Axial displacement  $u_x$  are  $-30$ ,  $-90$ ,  $-150$ mm respectively). As we can see from Figure 3.14 the kinematics of deformed column is captured accurately by the present shell-based SPH model. We can observe also the highly nonlinear character of the post-buckling solution which has been predicted appropriately even with the presence of very large rotations (see Figure 3.14).

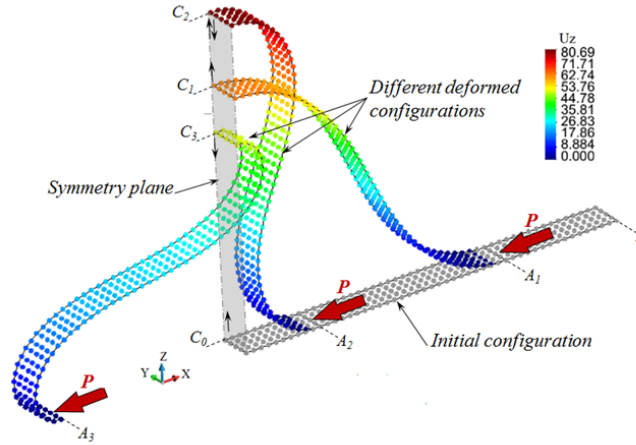


Figure 3.14: Three different deformed configurations of the Euler column using the present SPH model

The good quality of results obtained through this application, proves that the present shell-based SPH model can be used as a real alternative to the FEM for the nonlinear post-buckling analysis of shell structure.

### 3.6.5 Nonlinear analysis of a clamped circular arch

The example of a deep circular arch shell structure is shown in the Figure 3.15 of which two ends are fully clamped and the load  $F$  is applied on the middle point of the arch. It has geometry (see Figure 3.15) with the following parameters  $R = 100mm$ ,  $b = 20mm$ ,  $t = 5mm$  and  $\phi = 215^\circ$ . The material of the arch is assumed to be steel with Young's modulus  $E = 210GPa$ , Poisson's rate  $\nu = 0.3$  and density  $\rho = 7800kg/m^3$ . An example of the clamped-clamped deep arch in 2D was investigated by Wriggers and Simo [90] using beam elements.

For the present application, the full arch is modeled using a uniform discretization of  $95 \times 5$  SPH particles. The nonlinear analysis was conducted using the Explicit Dynamics scheme with a total simulation time corresponding to  $10ms$ . As in the previous application, the displacement control technique was applied at the centroid line of the arch where a maximal displacement of  $W = 250mm$  was targeted. The displacement under the loading points was increased quadratically during the first  $5ms$ , and then its maximal was maintained constant until the end of simulation in order to reach the quasi-static solution.

In order to assess the validation of the present SPH model, the same structure was modeled

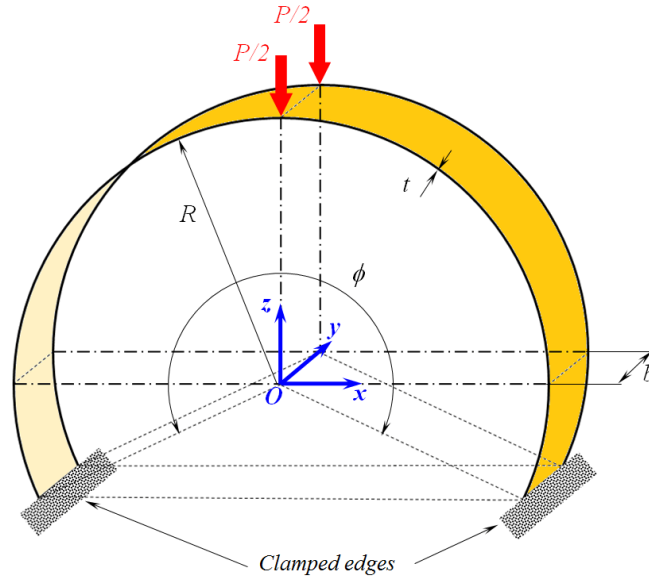


Figure 3.15: Geometry of the deep arch

using ABAQUS<sup>®</sup> Standard code to achieve a reference solution. A mesh of  $94 \times 5$  S4R shell elements were used to model the arch.

Figure 3.16 presents the evolution of the load in function of the transversal displacement  $W$  at the centroid of the deep arch, where a load parameter  $\lambda = PR^2/EI$  is used. The present shell-based SPH model predicted the first limit point with a load parameter of  $\lambda_{cr}^{SPH} = 9.243$ , while the reference solution of Wriggers and Simo [90] indicated  $\lambda_{cr}^{Reference} = 9.729$  and the one obtained using ABAQUS<sup>®</sup> was  $\lambda_{cr}^{ABAQUS} = 10.160$ . The displacement at the central line of the arch obtained using the present SPH model was  $W_{cr}^{SPH} = 73mm$ , while the reference solution of Wriggers and Simo [90] gave  $W_{cr}^{Reference} = 72.13mm$ , and the one using ABAQUS<sup>®</sup> was  $W_{cr}^{ABAQUS} = 72.5mm$ .

The principal obtained results with their corresponding errors with respect to reference solutions are summarized in Table 3.4.

Table 3.4: Summary of the principal results of the arch

	Wriggers and Simo	ABAQUS	Present Shell SPH
Critical load parameter $\lambda$	9.729	10.160	9.243
Error (%)	—	4.43	-5.00

As we can observe from Table 3.4, the critical buckling load is estimated with 5% which is of the same amount of error as the FEM using ABAQUS 4.43%. Again, this result proves



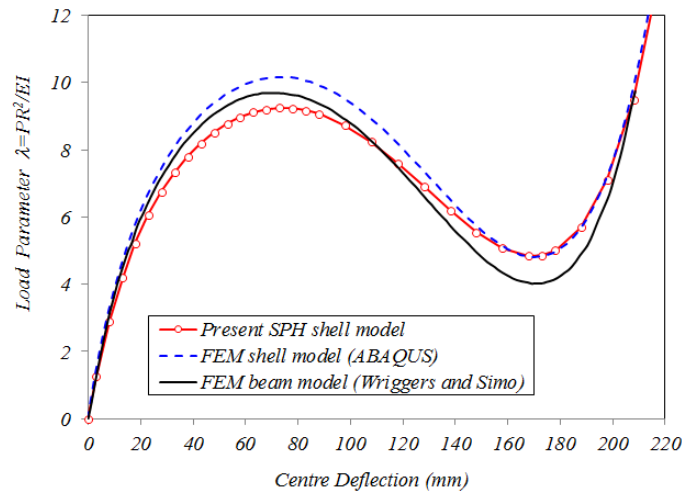


Figure 3.16: Comparison of the load-displacement at the centroid of the arch

that the present shell-based SPH method has a great potential compared to the FEM when dealing the post-buckling analysis of shell structures.

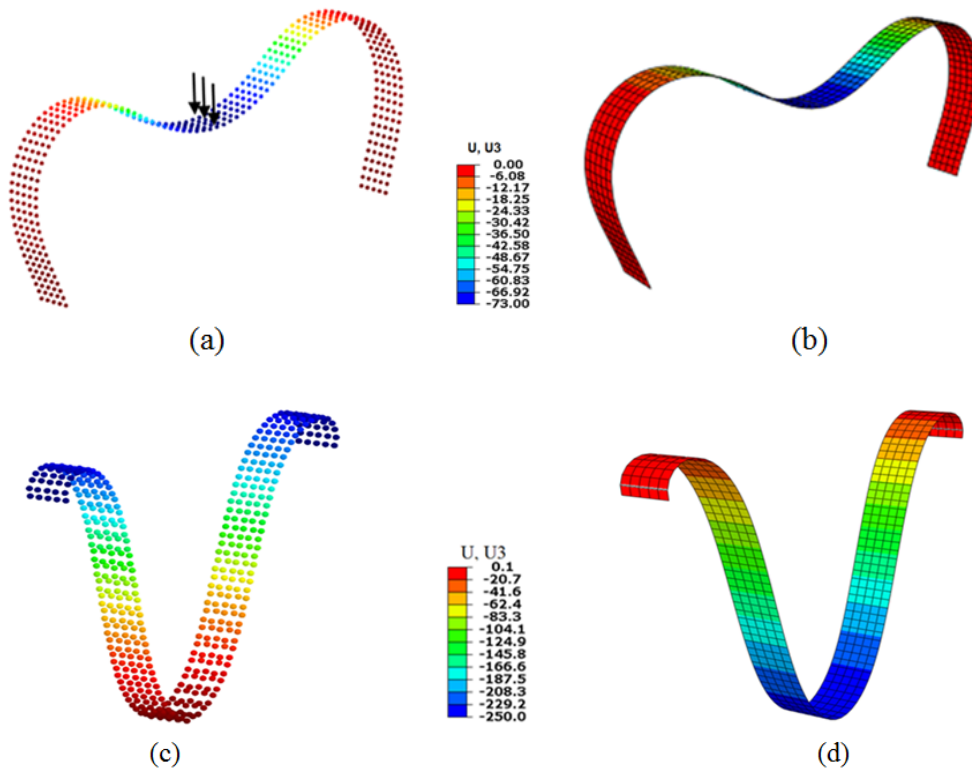


Figure 3.17: Different deformed configurations of the arch: (a) Limit point SPH (b) Limit point ABAQUS (c) Maximal displacement SPH (d) Maximal displacement ABAQUS

Figure 3.17 shows the deformed configurations of the deep arch obtained using the present

SPH model and the one of ABAQUS, at two different times: first limit point time and maximal displacement time. As one can observe, the deformed configurations captured at the same time are of very close shape. Figure 15-c shows a very large deformation of the arch performed by the shell-based SPH model, which indicates its capability of handling large transformations of shell-like structures using only one layer of particles in the mid-surface contrarily to the commonly used continuum based SPH model found in the literature or available in commercial softwares.

### 3.6.6 Nonlinear Analysis of a Plate Buckling

Herein we deal with a rectangular plate buckling using a geometrically nonlinear analysis. This interest of this example is the existence of an analytical solution which will allow evaluating precisely the efficiency of the Shell-based SPH method. The studied plate is simply supported on its four edges and submitted to an equal uniform compression load  $P$  on two opposite edges  $b$  as shown in Figure 3.18. Due to the problem symmetry, only a quarter of the plate is modeled and discretized using only one layer of  $25 \times 25$  particles through the plate mid-surface.

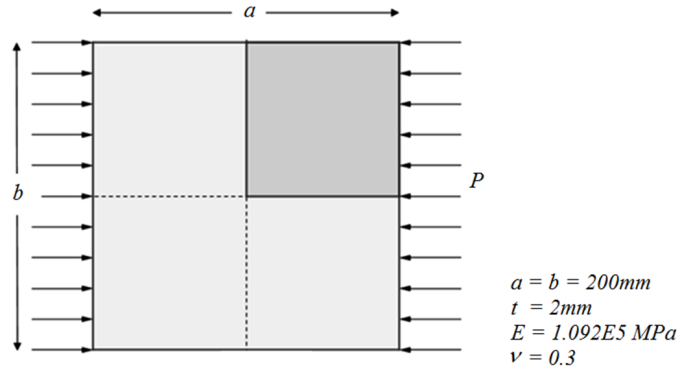


Figure 3.18: Geometry and Material characteristics of the plate

The analytic solution of the critical buckling load can be retrieved in [104], it is given by:  $P_{cr} = \pi^2 Et^2 / 3a^2 (1 - \nu^2)$  which corresponds numerically to  $P_{cr} = 78.96 \text{ N/mm}$ . The geometrically nonlinear analysis is carried out using the plate edge displacement control method. Therefore different horizontal edge displacements are applied until a maximal load  $P = 100 \text{ N/mm}$  is achieved. In order to compare the shell-based SPH solution to the FEM result, the plate is modeled using ABAQUS<sup>®</sup> code with  $25 \times 25$  S4R shell elements. The central plate load-displacement curve is then extracted and a comparison is made between

the different solutions as shown in Figure 3.19.

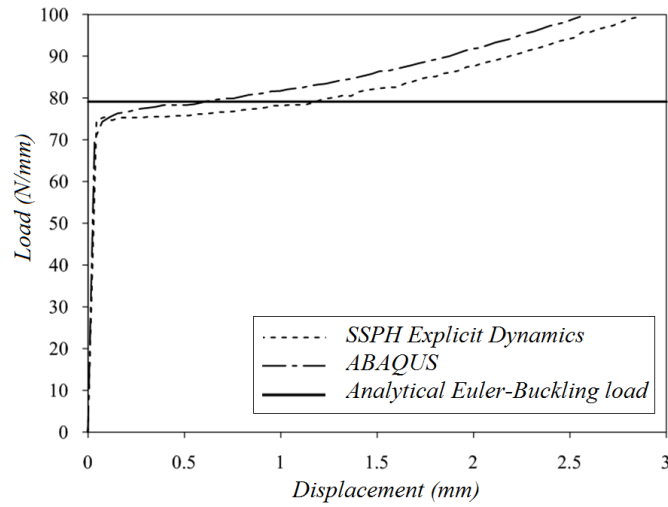


Figure 3.19: Load-Deflection curve at the central plate

As we can observe from Figure 3.19, the Shell-based SPH solution is in a very good agreement with FEM solution, at the first loading phase up to the buckling load value. After buckling emergence the obtained nonlinear loading path slightly underestimates (error of 6.25%) the FE solution of ABAQUS<sup>®</sup> code. The critical buckling load obtained using the geometrically nonlinear analysis based on SPH shell formulation is  $P_{cr}^{SPH} = 75.5 N/mm$ , with a small error of 4.38% with respect to the analytical solution. This critical buckling load is very close to the one obtained using ABAQUS<sup>®</sup> code. Figure 3.20 shows the final deformed configuration obtained using our in-house developed code using the Shell-based SPH method, this final configuration is very close to the one obtained using FEM with ABAQUS<sup>®</sup> code.

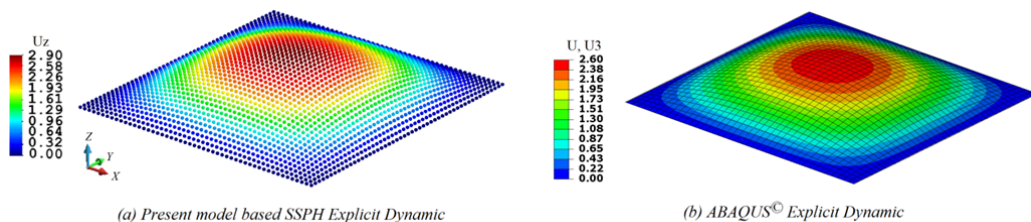


Figure 3.20: Comparison of the deformed plate configurations for  $P = 100 N/mm$  (Present SPH vs. FEM)

### 3.6.7 Geometrically Nonlinear Analysis of a cylindrical roof

The second application investigates the post-buckling analysis of a hinged cylindrical roof subjected to a central pinching load as shown in Figure 3.21. This benchmark has interested many researchers due to the presence of snapping behavior [105]. Owing to the tangential global stiffness matrix singularity near the limit point, the classical load controlled method is not suitable in the present case. The displacement control method [88] is adopted for this application to achieve a complete equilibrium loading path.

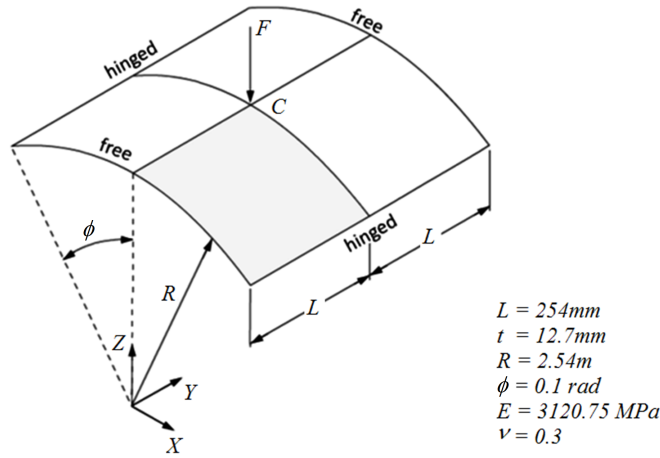
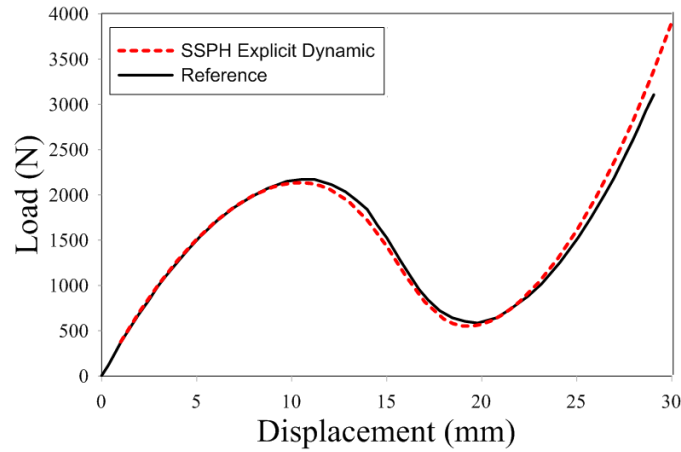


Figure 3.21: Hinged cylindrical roof (geometry and material data)

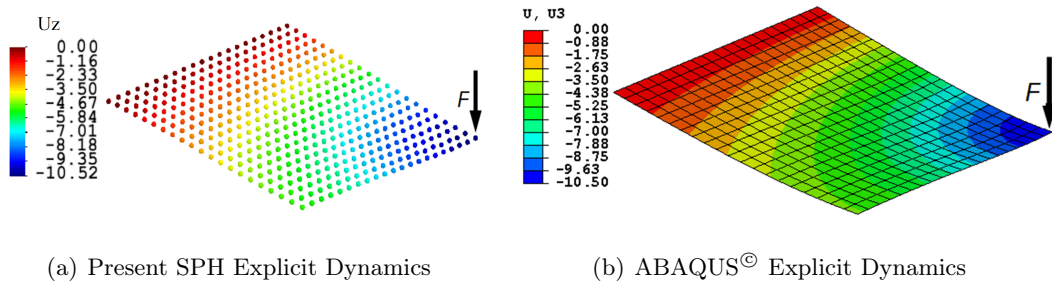
Due to symmetry, only a quarter of the roof is modeled using only one layer of  $21 \times 21$  particles in the Shell-based SPH method. In our simulation the displacement  $W_C$  at the central point  $C$ , is controlled starting from  $0\text{mm}$  to  $30\text{mm}$ , which grows linearly until 100% in a total time of  $3\text{ms}$ .

The load-displacement curve obtained using the Shell-based SPH explicit dynamics method is given in Figure 3.22 and compared to the reference solution by Klinkel [105]. As we can observe from Figure 3.22, the shell-based SPH loading path solution is in a very good agreement with the reference solution with an error globally less than 2.5% during all loading path and even in the post-buckling phase. The critical displacement value obtained using shell-based SPH method is  $W_C = 10.5\text{mm}$ , which is only 1.78% error compared to the reference value of Klinkel [105].

We depicted in Figure 3.23(a), the deformed configuration at the vicinity of the limit point obtained using the Shell-based SPH method. This deformed configuration is identical to the one obtained by the FEM using S4R shell elements of ABAQUS<sup>®</sup> Explicit code, as

Figure 3.22: Curve of Load-Displacement at point  $C$ 

indicated in Figure 3.23(b).

Figure 3.23: Deformed configuration at the vicinity of the limit point ( $W_C = 10.5mm$ )

### 3.6.8 Snap-through of a shallow spherical shell

This application deals with the snap-through nonlinear analysis of a shallow spherical shell, presented in Figure 3.24(a). The radius of the spherical segment is  $2540mm$ , thickness= $99.45mm$  and  $a = 784.9mm$ . The segment is made of aluminum with material properties  $E = 68.95GPa$ ,  $\nu = 0.3$  and  $\rho = 2700kg/m^3$ . The shell structure is hinged at all edges and a concentrated load  $P$  is applied at its centroid  $C$ . This example has been investigated by Leicester *et al.* [106] and Bucalem and Bathe [107] due to the large displacement nature of the structure.

For symmetry reason, only a quarter of the structure was modeled using a uniform  $21 \times 21$  SPH particles (see Figure 3.24(b)). The nonlinear analysis was conducted using the Explicit Dynamics scheme with a total simulation time corresponding to  $25ms$ . Due to the presence of a limit point of the structure response, the displacement control technique was applied

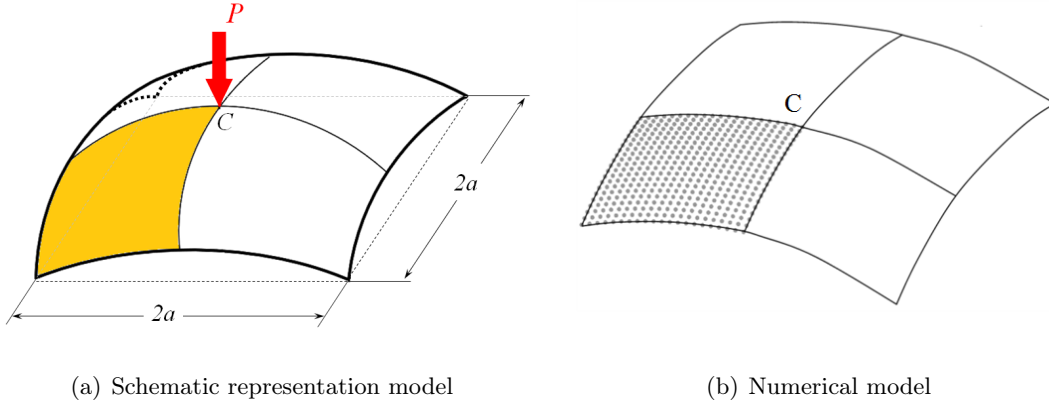


Figure 3.24: Geometry and material data of the shallow shell

at point  $C$  where a maximal displacement of  $W = 300\text{mm}$  was targeted. In order to reduce the loading oscillations, the displacement of point  $C$  was increased quadratically during the first  $10\text{ms}$ , and then the maximal value of displacement was maintained constant until the end of simulation in order to reach the quasi-static solution.

The load displacement response of the structure obtained using the present shell-based SPH model is depicted in Figure 3.25, where a load parameter  $\lambda = PR^2/Eat^3$  is used. As a first remark, we can observe the nonlinear character of the solution with the presence of a limit point corresponding to a predicted buckling load parameter of  $\lambda_{cr}^{SPH} = 6.043$ , while the reference solution of Leicester *et al.* [106] indicated  $\lambda_{cr}^{Leicester} = 6.216$  and the one given by Bucalem and Bathe [107]  $\lambda_{cr}^{Bucalem} = 5.917$ .

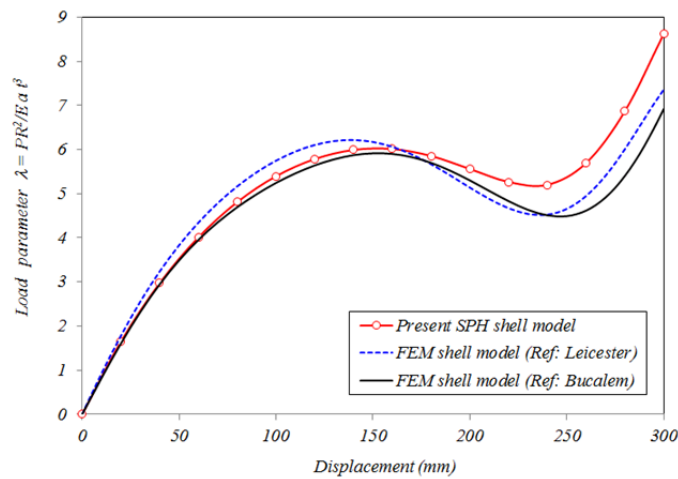


Figure 3.25: Comparison of the load-displacement at the centroid of the shallow shell

A comparison of the displacement at point  $C$ , at the same time when the critical buckling

started, showed that the shell-based SPH model allowed an estimation  $W_{cr}^{SPH} = 152mm$ , while the reference solution of Leicester *et al.* [106] gave  $W_{cr}^{Leicester} = 138.5mm$ , and the one found by Bucalem and Bathe [107] was  $W_{cr}^{Bucalem} = 152.6mm$ .

An analysis of the three curves depicted in Figure 3.25 showed that the present shell-based SPH model allows a good prediction of the structure response up to the critical buckling point with an overall error about 2% compared to the mean reference solution. However for the post-buckling phase the present SPH model overestimated the solution to a certain extent.

For comparison purpose, a summary of principal obtained results with their corresponding errors with respect to reference solutions are given in Table 3.5.

Table 3.5: Comparison of CPU time for analysis of the beam (Present SPH vs. Continuum SPH)

	Buckling load parameter		Displacement	
	$\lambda$	SPH error (%)	$W$ (mm)	SPH error (%)
FEM(Leicester [106])	6.216	-2.78	138.5	9.75
FEM(Bucalem and Bathe [107])	5.917	2.13	152.6	-0.39
Mean reference solution	6.067	-0.39	145.55	4.43

As we can observe from Table 3.5, the results obtained using the present shell-based SPH model are very close to the mean reference solution (The average solution of Leicester *et al.* [106] and Bucalem and Bathe [107]). The critical buckling load is estimated with 0.39% of error while the displacement predicted at the starting of buckling presents an error of 4.43%. These values are very small which indicates that the present SPH model can be used as a powerful tool for the nonlinear analysis of shell structures.

Figure 3.26 shows the deformed configuration of the spherical shell obtained for the maximal transversal displacement. Together with the deformed structure, one-half of the initial structure is plotted to show the magnitude of deflection of the spherical shell under the load.

### 3.7 Conclusion

In this Chapter, the classical SPH method used for 3D solids, has been extended using the Total Lagrangian to build-up a new shell-based SPH formulation for the geometrically

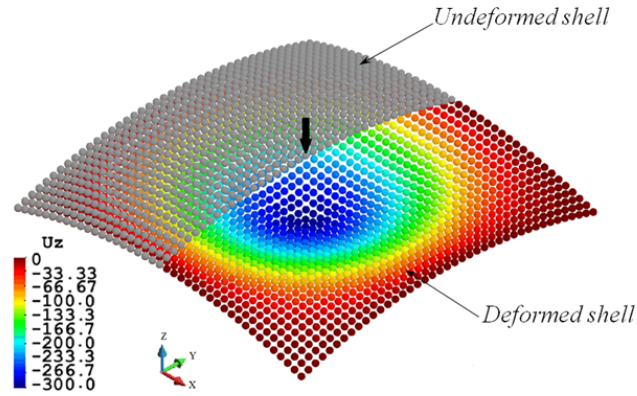


Figure 3.26: Initial and deformed configuration of the shallow shell for  $W = 300mm$  using the present SPH model

nonlinear analysis of shell-like structures. The shell-based SPH method has been developed using the Mindlin-Reissner shell theory which is valid for thin and thick shell structure. This combination allows only one layer of particles located in the shell mid-surface to reproduce the whole shell behavior. Moreover, the Rodrigues formula associated with quaternion parameterization was introduced to update the pseudo-normal vector. This allows the method to be very efficient in dealing with structures undergoing very large three dimensional rotations.

To validate the reliability and accuracy of the newly developed shell-based SPH method in solving shell-like structure problems, several numerical applications including geometrically nonlinear behavior were performed and the results were compared with analytical solutions and also with numerical reference solutions available from the literature or obtained using the Finite Element method by means of ABAQUS<sup>®</sup> commercial software. While keeping a good level of accuracy, the present shell-based SPH model presents promising potentials as a new alternative numerical method.



---

# *Shell-based SPH method for thin multilayered structures*

---

In this chapter, the constitutive relations of composite laminates will be incorporated into the above mentioned efficient shell-based SPH method, to build-up a SPH model for multilayered composite shell structures. Equivalent single-layer theories for analyzing composite plates/shells are presented briefly. As a best compromise of solution accuracy, economy and simplicity, the first-order shear deformation theory is employed and a suitable shear correction factor is introduced. This will ensure that the strain energy provided by the constant transverse shear stress is equal to the energy due to 3D stress distribution, which is in the elastic case quadratically distributed through the layer thickness. The resulting strong-form governing dynamic equations of composites are discretized using the shell-based SPH method with respect to the material coordinates. At the end, several numerical applications are presented to validate the proposed SPH method.

## **4.1 Overview of laminates modeling using mesfree methods**

Composite structural parts are often very thin and made up of complex anisotropic materials which are usually produced by pultrusion [108]. Nowadays with the establishment of compulsory environmental protection and safety standards, laminated composite structures are intensively used in various engineering areas, involving aerospace, automotive, marine, civil, sport, *etc.* This is due to their numerous desirable characteristics compared to traditional isotropic structures, such as high strength and stiffness to weight ratio, strong energy absorption, long fatigue life, good corrosion resistance and often low production cost.

Generally multilayered thin structures are often designed to support heavy loads or severe loading impacts, they usually present a nonlinear behavior which consist in large displacements (due to lightweighting) accompanied with small elastic strains. Therefore

the nonlinear analysis of flexure, buckling and post-buckling of thin to thick multilayered composite structures becomes firmly necessary in order to better control their behavior.

Many theories have been proposed in the literature to handle laminated structures, such as the Equivalent Single Layer (ESL) theories which are well developed. They are derived from the 3D elastic continuum theory by making suitable assumptions concerning the kinematics of deformation or the stress state through the thickness of the laminate and render a 3D problem reduced to a 2D problem.

Such theories include the Classical Laminated Plate Theory (CLPT), the First-order Shear Deformation Theory (FSDT), the Higher-order Shear Deformation Theory (HSDT) [102]. The simplest one therein, the CLPT originates from the Kirchhoff plate theory, in which the normal vectors to the mid-surface remain straight and normal in the deformation process. Therefore, the transverse shear deformation is ignored and good results can be obtained only for thin isotropic shell structures.

As it is well known, transverse shear effects are important for multilayered composite structures, even if they are thin [102]. The FSDT based on Mindlin-Reissner shell theory, assumes the transverse shear strains to be constant along the thickness. This assumption violates the zero-shear stress condition on the bounding layers of the laminate, while it is well-known that the exact shear stress distribution through the thickness is a piece-wise parabolic function for the case of elastic materials. Therefore it is important to take into account the shearing effects by introducing the so-called shear correction factor [102, 109, 110] to avoid the dominance of shear strain energy compared to the flexural one in the case of very thin structures. This makes the FSDT capable of providing accurate physical response of the laminated composite structures.

In HSDT usually high order polynomial functions in normal direction are used for the definition of the shell displacement field, with the introduction of additional degrees of freedom (dof). The later are often difficult to interpret in physical terms and solved using the equilibrium conditions on the shell layers. The displacement description accommodates quadratic distribution of transverse shear strains and hence stresses, and vanishing of transverse shear stresses on the top and bottom plies. However, these methods require more additional computational efforts and therefore may become not convenient for the modeling of complex industrial structures. On the other side, the simplicity of the FSDT has peaked the interest of researchers and has been the subject of extensive investigations since last few decades to improve constantly its performance. As a result, nowadays the

FSDT is widely used and implemented in most of FE commercial codes.

Since their introduction, laminate theories have been developed using the FE method, due to its simplicity and good accuracy. Many efficient FE models have been proposed by authors for the modeling of composite multilayered structures. Based on CLPT, Sleight and Knight [111] studied the progressive failure of composite plates subjected to shear and compressive loading under geometrically nonlinear deformations. Based on FSDT, several phenomenological failure criteria were used in FE laminate structure models to capture linear and nonlinear first-ply failure loads of composite laminates subjected to in-plane and transverse loads [112]. For instance Zhang and Kim [113] proposed a simple displacement-based 3-node triangular element LDT18 for the study of geometrically nonlinear behavior of thin and thick laminated composite plates using the FSDT. Based on the HSDT, Moita *et al.* [114] proposed a discrete FE model based on an 8-node isoparametric element with 10 degrees of freedom per node, for the buckling analysis of laminated composite plate-shell structures.

Recently, a considerable work has been done for the modeling of composite multilayered structures using meshless methods. Liew *et al.* [115] used a Moving Least Squares Differential Quadrature method for the bending and buckling analysis of moderately thick plates based on the FSDT. Xiao *et al.* [116] studied static infinitesimal deformations of thick laminated composite elastic plates under different boundary conditions using the Meshless Local Petrov-Galerkin (MLPG) method combined with Radial Basis Functions (RBF) and the higher order normal and shear deformable plate theory. The Multiquadric Radial Basis Functions with a third-order shear deformation theory were developed by Ferreira *et al.* [117] to study static deformations of functionally graded square plates of different aspect ratios. The same authors also addressed the buckling analysis of isotropic and laminated plates subjected to partial in-plane edge loads using the FSDT based on wavelet collocation technique. Perhaps Wang *et al.* [118] were the first to investigate the reproducing kernel particle meshless method (RKPM) combined with the FSDT. They successfully used the RKPM for the modeling of flexural and buckling analysis of laminated composite plates. Nonlinear flexural analysis of laminated composite plates have been studied by Singh *et al.* [119] using RBF mesh free method. The same authors [120] investigated the buckling analysis of laminated composite plates subjected to thermo-mechanical loading, using Gaussian and multiquadric radial basis functions incorporating two different higher order shear deformation theories. A detailed review on applications using meshfree methods for

the analysis of composite structures can be retrieved in [121].

As for Smoothed Particle Hydrodynamics (SPH) method, high-even hyper-velocity impact and damage problems in different laminates have been investigated using 3D continuum SPH models [122–124]. However, based to our knowledge, large deflection and buckling analysis of composite multilayered structures using shell-based SPH technique with an equivalent single layer theories have not been studied.

In the following sections we will present the derivation of SPH composite shell model based on FSDT. The kinematics assumptions of multilayered shells are similar to the one used for the isotropic shells which has been detailed in Chapter 3, and are not repeated in this chapter. The deformation process is also expressed by the variation of five dofs  $\{\mathbf{u}_L, \boldsymbol{\theta}_L\} = \{u, v, w, \theta, \varphi\}^T$  of mid-surface particles written in the tangent mid-plan of the shell. The stress-strain relation of the composite material is more complex than that of isotropic material, which will be seen in section 2.

## 4.2 Constitutive relations of a multilayered shell structure

A lamina or ply is a typical sheet (flat or curved) of composite material and many laminae well bonded together by curing procedure to compose a laminate. The mechanical response of a laminate depends on the properties of each lamina, as well as the order in which the laminae are stacked. Therefore constitutive relations of lamina have to be introduced at first.

A typical unidirectional fiber-reinforced composite lamina is inherently heterogeneous from the microscopic point of view, but assumed to be homogeneous at the macroscopic level because of its weighted average of the constituent materials (fiber and matrix). A lamina is always treated as an orthotropic, linear elastic continuum [102] whose material symmetry planes are parallel and transverse to the fiber direction. Hence the constitutive relation is conveniently expressed in the principle material coordinates system  $\{L; T; Z\}$  in which axes  $L$  and  $T$  are taken to be parallel and transverse to the fiber direction in the plane of the lamina (see Figure 4.1). Axis  $Z$  is perpendicular to the plane of the lamina, coinciding with the global thickness direction of the synthetic laminate.

Most laminae are typically thin and experience a plane state of stress (Figure 4.2). FSDT employed here neglects the transverse normal stress  $\sigma_{ZZ}$  and reduce the generalized Hooke's

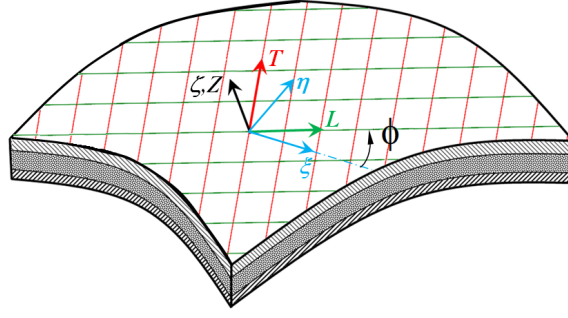


Figure 4.1: Fiber-reinforced lamina orientation axes

law to be

$$\boldsymbol{\sigma}_L = \mathbb{H}_L \boldsymbol{\varepsilon}_L \quad \text{and} \quad \boldsymbol{\tau}_L = \mathbb{H}_{\tau L} \boldsymbol{\gamma}_L \quad (4.1)$$

$$\text{with } \boldsymbol{\sigma}_L = \begin{Bmatrix} \sigma_{LL} \\ \sigma_{TT} \\ \tau_{LT} \end{Bmatrix}; \boldsymbol{\varepsilon}_L = \begin{Bmatrix} \varepsilon_{LL} \\ \varepsilon_{TT} \\ \gamma_{LT} \end{Bmatrix}; \boldsymbol{\tau}_L = \begin{Bmatrix} \tau_{LZ} \\ \tau_{TZ} \end{Bmatrix}; \boldsymbol{\gamma}_L = \begin{Bmatrix} \gamma_{LZ} \\ \gamma_{TZ} \end{Bmatrix}.$$

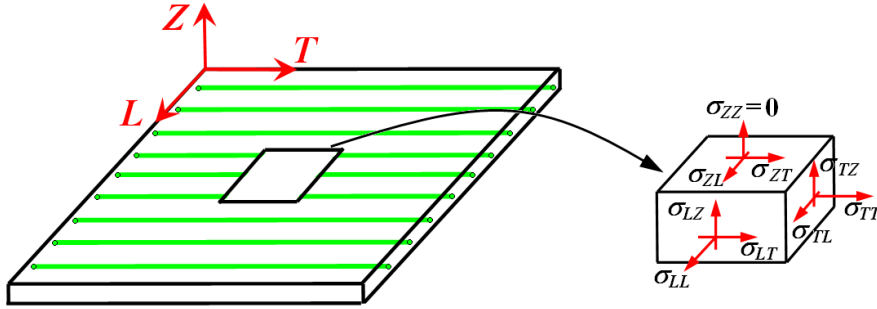


Figure 4.2: A lamina in a plane state of stress.

$$\mathbb{H}_L = \begin{bmatrix} H_{LL} & H_{LT} & 0 \\ H_{TL} & H_{TT} & 0 \\ 0 & 0 & G_{LT} \end{bmatrix}; \mathbb{H}_{\tau L} = \begin{bmatrix} G_{LZ} & 0 \\ 0 & G_{TZ} \end{bmatrix} \text{ are called plane stress-reduced}$$

stiffnesses. The components of the stiffness matrices are related to the engineering constants as follows:

$$H_{LL} = \frac{E_L}{1 - \nu_{LT}\nu_{TL}}, \quad H_{LT} = H_{TL} = \frac{\nu_{TL}E_L}{1 - \nu_{LT}\nu_{TL}} = \frac{\nu_{LT}E_T}{1 - \nu_{LT}\nu_{TL}}, \quad H_{TT} = \frac{E_T}{1 - \nu_{LT}\nu_{TL}}.$$

For unidirectional fiber composite lamina, the plane normal to the fiber direction  $L$  can be considered as the isotropic plane, which signifies transversely isotropy. Therefore, there are only five independent engineering elastic constants:  $E_L$ ,  $E_T = E_Z$ ,  $\nu_{LT}$ ,  $G_{LT} = G_{LZ}$  and

$G_{TZ} = \frac{E_T}{2(1 + \nu_{TZ})}$ . These constants can be determined experimentally using appropriate test specimens made up of the material.

The principal material directions  $\{L; T; Z\}$  of orthotropy often do not coincide with curvilinear coordinate directions that are geometrically natural to the solution of the problem. Further, composite laminates have several layers, each with different fiber orientation. Thus, it is necessary to establish the stress-strain relations in the local curvilinear direction  $\{\xi; \eta; \zeta\}$  in which the  $\zeta$ -axis is parallel to  $Z$ -direction. Considering the material fiber orientation angle  $\phi = \phi(\xi, L)$  counterclockwise from the  $\xi$ -axis, the in-plane and transverse shear stress components can be written with relation to the correspondent strain components which are directly computed from the displacement assumption of FSDT

$$\boldsymbol{\sigma} = \mathbb{H} \boldsymbol{\varepsilon} = \mathbb{T}_1^T \mathbb{H}_L \mathbb{T}_1 \boldsymbol{\varepsilon} \quad \text{and} \quad \boldsymbol{\tau} = \mathbb{H}_\tau \boldsymbol{\gamma} = \mathbb{T}_2^T \mathbb{H}_{\tau L} \mathbb{T}_2 \boldsymbol{\gamma} \quad (4.2)$$

in which we have the transformation matrix between  $\{\xi; \eta; \zeta\}$  and  $\{L; T; Z\}$  coordinate system

$$\mathbb{T}_1 = \begin{bmatrix} C^2 & S^2 & CS \\ S^2 & C^2 & -CS \\ -2CS & 2CS & C^2 - S^2 \end{bmatrix}; \quad \mathbb{T}_2 = \begin{bmatrix} C & S \\ -S & C \end{bmatrix}; \quad \text{and } C = \cos\phi; S = \sin\phi.$$

Considering constant over the thickness, the membrane strains  $\boldsymbol{\varepsilon}_m$ , the curvatures  $\boldsymbol{\varepsilon}_b$  and the shearing strains  $\boldsymbol{\gamma}$ , and integrating their conjugated stresses in each ply, one can get the membrane forces  $\mathbf{N}$ , the bending moments  $\mathbf{M}$ , and the transverse shearing forces  $\mathbf{T}$  as follows

$$\mathbf{N} = \begin{Bmatrix} N_{\xi\xi} \\ N_{\eta\eta} \\ N_{\xi\eta} \end{Bmatrix} = \int_{-\frac{t}{2}}^{\frac{t}{2}} \boldsymbol{\sigma} d\zeta = \mathbb{A} \boldsymbol{\varepsilon}_m + \mathbb{B} \boldsymbol{\varepsilon}_b \quad (4.3)$$

$$\mathbf{M} = \begin{Bmatrix} M_{\xi\xi} \\ M_{\eta\eta} \\ M_{\xi\eta} \end{Bmatrix} = \int_{-\frac{t}{2}}^{\frac{t}{2}} \zeta \boldsymbol{\sigma} d\zeta = \mathbb{B} \boldsymbol{\varepsilon}_m + \mathbb{D} \boldsymbol{\varepsilon}_b \quad (4.4)$$

$$\mathbf{T} = \begin{Bmatrix} T_{\xi\zeta} \\ T_{\eta\zeta} \end{Bmatrix} = \int_{-\frac{t}{2}}^{\frac{t}{2}} \mathbb{H}_\tau \boldsymbol{\gamma} d\zeta = \mathbb{C} \boldsymbol{\gamma} \quad (4.5)$$

Finally the generalized constitutive relation for a lamina can be expressed in a more condensed form

$$\begin{Bmatrix} \mathbf{N} \\ \mathbf{M} \\ \mathbf{T} \end{Bmatrix} = \begin{bmatrix} \mathbb{A} & \mathbb{B} & 0 \\ \mathbb{B} & \mathbb{D} & 0 \\ 0 & 0 & \mathbb{C} \end{bmatrix} \begin{Bmatrix} \boldsymbol{\varepsilon}_m \\ \boldsymbol{\varepsilon}_b \\ \boldsymbol{\gamma} \end{Bmatrix} \quad (4.6)$$

with

$$\mathbb{A} = \int_{-\frac{t}{2}}^{\frac{t}{2}} \mathbb{H} d\zeta = \sum_{k=1}^{NL} (\zeta_k - \zeta_{k-1}) \mathbb{H}_k \quad (4.7)$$

$$\mathbb{B} = \int_{-\frac{t}{2}}^{\frac{t}{2}} \zeta \mathbb{H} d\zeta = \sum_{k=1}^{NL} \frac{1}{2} (\zeta_k^2 - \zeta_{k-1}^2) \mathbb{H}_k \quad (4.8)$$

$$\mathbb{D} = \int_{-\frac{t}{2}}^{\frac{t}{2}} \zeta^2 \mathbb{H} d\zeta = \sum_{k=1}^{NL} \frac{1}{3} (\zeta_k^3 - \zeta_{k-1}^3) \mathbb{H}_k \quad (4.9)$$

$$\mathbb{C} = \int_{-\frac{t}{2}}^{\frac{t}{2}} \mathbb{H}_\tau d\zeta = \sum_{k=1}^{NL} (\zeta_k - \zeta_{k-1}) \mathbb{H}_{\tau k} \quad (4.10)$$

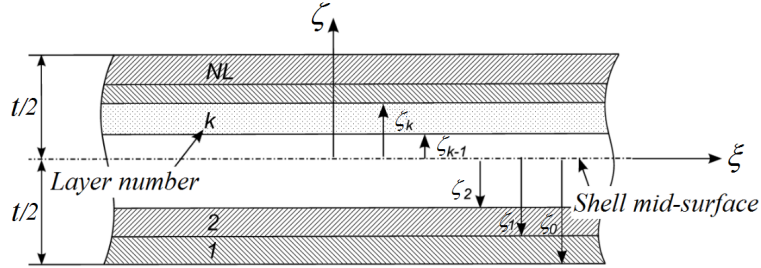


Figure 4.3: Stacking of  $NL$  material layers within the shell thickness

In the constitutive relation of Equation (4.6),  $NL$  is noted as the number of layers of laminae.  $k$  signifies the  $k$ -th lamina which is bounded in coordinates  $[\zeta_{k-1}, \zeta_k]$  in the thickness direction, showed in Figure 4.3. Sub-matrix  $\mathbb{A}$ , expressed in Equation (4.7) and involved with the in-plane response of the laminate, is denoted as extensional stiffness. Detailed in Equation (4.9), the sub-matrix  $\mathbb{D}$  is related to the out-of-plane bending response of the laminate, hence it is called bending stiffness. The sub-matrix  $\mathbb{B}$  in the Equation (4.8) is called bending-extension coupling matrix who relates to the interaction between the membrane and the bending deformations. The sub-matrix  $\mathbb{C}$  documented in Equation (4.10) is the transverse shear stiffness. For isotropic shell structures and symmetric stacking  $\mathbb{B}$  is null which means no coupling of extension and bending effects occurs.

### 4.2.1 Shear correction factor

As mentioned above, FSDT for mulatylayered composite shells results in a constant transverse shear stress through each lamina and consequently a piece-wise constant transverse shear stress distribution through the laminate thickness. However, the exact 3D elasticity solution for laminated shell structures exhibits a piece-wise higher order variation of these types of stresses through the thickness and vanishing at the two external bounding surfaces normal to the thickness. This discrepancy between the actual and predicted stress state is often corrected by a coefficient called *shear correction factor* [102, 109, 110].

A recall of Equation (4.2) and rewriting the equation of transverse shear stress explicitly, gives

$$\begin{Bmatrix} \tau_{\xi\zeta} \\ \tau_{\eta\zeta} \end{Bmatrix} = \begin{bmatrix} H_{\tau 11} & H_{\tau 12} \\ H_{\tau 12} & H_{\tau 22} \end{bmatrix} \begin{Bmatrix} \gamma_{\xi\zeta} \\ \gamma_{\eta\zeta} \end{Bmatrix} \quad (4.11)$$

By introducing two coefficients  $\kappa_1$  and  $\kappa_2$ , the new transverse shear stresses in a lamina take the following form

$$\begin{Bmatrix} \tau'_{\xi\zeta} \\ \tau'_{\eta\zeta} \end{Bmatrix} = \begin{bmatrix} \kappa_1^2 H_{\tau 11} & \kappa_1 \kappa_2 H_{\tau 12} \\ \kappa_1 \kappa_2 H_{\tau 12} & \kappa_2^2 H_{\tau 22} \end{bmatrix} \begin{Bmatrix} \gamma_{\xi\zeta} \\ \gamma_{\eta\zeta} \end{Bmatrix} \quad (4.12)$$

It is possible to define one correction factor for a given cross section or several ones with one factor per ply and these two methods are equivalent [109]. In this chapter, the way that all plies have the same factor is employed. Therefore, the resultant transverse forces can be reobtained by integrating the correspondent shearing stresses through the thickness

$$\mathbf{T} = \begin{Bmatrix} T_{\xi\zeta} \\ T_{\eta\zeta} \end{Bmatrix} = \begin{bmatrix} \kappa_1^2 C_{11} & \kappa_1 \kappa_2 C_{12} \\ \kappa_1 \kappa_2 C_{12} & \kappa_2^2 C_{22} \end{bmatrix} \begin{Bmatrix} \gamma_{\xi\zeta} \\ \gamma_{\eta\zeta} \end{Bmatrix} \quad (4.13)$$

At first, we present the procedure for determining the factor  $\kappa_1$ . Considering a laminated beam based on the FSDT, the resultant stresses  $N_{\eta\eta}, N_{\xi\eta}, M_{\eta\eta}, M_{\xi\eta}, T_{\eta\zeta}$  are assumed to be zero [110]. The in-plane strains can be computed by inverting the stiffness matrix in the Equation (4.6):

$$\begin{Bmatrix} \varepsilon_m \\ \varepsilon_b \end{Bmatrix} = \begin{bmatrix} \mathbb{A}' & \mathbb{B}' \\ \mathbb{B}' & \mathbb{D}' \end{bmatrix} \begin{Bmatrix} \mathbf{N} \\ \mathbf{M} \end{Bmatrix} \quad (4.14)$$

The transverse shear strains can be given by solving the Equation (4.13) and  $\gamma_{\xi\zeta}$  is explicitly expressed as

$$\gamma_{\xi\zeta} = \frac{C_{22} T_{\xi\zeta}}{\kappa_1^2 (C_{11} C_{22} - C_{12}^2)} \quad (4.15)$$



#### 4.2. CONSTITUTIVE RELATIONS OF A MULTILAYERED SHELL STRUCTURE 85

Consequently, the transverse shear strain energy per unit length evaluated from the predicted constant transverse strain  $U_{shell}$  can be computed as

$$U_{shell} = \frac{1}{2} T_{\xi\zeta} \gamma_{\xi\zeta} = \frac{C_{22} T_{\xi\zeta}^2}{2\kappa_1^2 (C_{11} C_{22} - C_{12}^2)} \quad (4.16)$$

True transverse shear stress  $\tau_{\xi\zeta}$  is obtained from the resolution of static equilibrium equation for the stresses acting in the  $\xi\zeta$ -plane in the absence of body forces:

$$\sigma_{\xi\xi,\xi} + \tau_{\xi\zeta,\zeta} = 0 \quad (4.17)$$

Hence

$$\tau_{\xi\zeta} = - \int_{-\frac{t}{2}}^{\zeta} \sigma_{\xi\xi,\xi} d\zeta \quad (4.18)$$

where  $\sigma_{\xi\xi}$  is linked with the in-plane strains by Equation (4.2)

$$\begin{aligned} \sigma_{\xi\xi} &= H_{11}\varepsilon_{\xi\xi} + H_{12}\varepsilon_{\eta\eta} + H_{13}\varepsilon_{\xi\eta} \\ &= H_{11}\varepsilon_{m\xi\xi} + H_{12}\varepsilon_{m\eta\eta} + H_{13}\varepsilon_{m\xi\eta} \\ &\quad + \zeta(H_{11}\varepsilon_{b\xi\xi} + H_{12}\varepsilon_{b\eta\eta} + H_{13}\varepsilon_{b\xi\eta}) \end{aligned} \quad (4.19)$$

Substituting the in-plane strains calculated from Equation (4.14) into the expression of  $\sigma_{\xi\xi}$ , yields

$$\begin{aligned} \sigma_{\xi\xi} &= H_{11}(A'_{11}N_{\xi\xi} + B'_{11}M_{\xi\xi}) + H_{12}(A'_{12}N_{\xi\xi} + B'_{12}M_{\xi\xi}) + H_{13}(A'_{13}N_{\xi\xi} + B'_{13}M_{\xi\xi}) + \\ &\quad \zeta \left[ H_{11}(B'_{11}N_{\xi\xi} + D'_{11}M_{\xi\xi}) + H_{12}(B'_{12}N_{\xi\xi} + D'_{12}M_{\xi\xi}) + H_{13}(B'_{13}N_{\xi\xi} + D'_{13}M_{\xi\xi}) \right] \\ &= H_{1\alpha}(A'_{1\alpha}N_{\xi\xi} + B'_{1\alpha}M_{\xi\xi}) + \zeta H_{1\alpha}(B'_{1\alpha}N_{\xi\xi} + D'_{1\alpha}M_{\xi\xi}) \end{aligned} \quad (4.20)$$

in which  $\alpha = 1, 2, 3$ .

Replacing the  $\sigma_{\xi\xi}$  in Equation (4.17) by above expression and considering the static equilibrium condition  $N_{\xi\xi,\xi} = 0$ ,  $M_{\xi\xi,\xi} = T_{\xi\zeta}$ , results in

$$\begin{aligned} \tau_{\xi\zeta} &= - \int_{-\frac{t}{2}}^{\zeta} \left\{ H_{1\alpha}(A'_{1\alpha}N_{\xi\xi} + B'_{1\alpha}M_{\xi\xi}) + \zeta \left[ H_{1\alpha}(B'_{1\alpha}N_{\xi\xi} + D'_{1\alpha}M_{\xi\xi}) \right] \right\}_{,\xi} d\zeta \\ &= - \int_{-\frac{t}{2}}^{\zeta} H_{1\alpha}(B'_{1\alpha} + \zeta D'_{1\alpha}) M_{\xi\xi,\xi} d\zeta \\ &= - \int_{-\frac{t}{2}}^{\zeta} H_{1\alpha}(B'_{1\alpha} + \zeta D'_{1\alpha}) T_{\xi\zeta} d\zeta \end{aligned} \quad (4.21)$$

The correspondent transverse shear strain  $\gamma_{\xi\zeta}$  is obtained from Equation (4.11)

$$\gamma_{\xi\zeta} = \frac{H_{\tau 22} \tau_{\xi\zeta}}{H_{\tau 11} H_{\tau 22} - H_{\tau 12}^2} \quad (4.22)$$

The exact transverse shear strain energy per unit length  $U_{3D}$  is a product of the mutually-conjugated stress and strain

$$\begin{aligned}
U_{3D} &= \frac{1}{2} \int_{-\frac{t}{2}}^{\frac{t}{2}} \tau_{\xi\zeta} \gamma_{\xi\zeta} d\zeta \\
&= \frac{1}{2} \int_{-\frac{t}{2}}^{\frac{t}{2}} \frac{H_{\tau 22} \tau_{\xi\zeta}^2}{H_{\tau 11} H_{\tau 22} - H_{\tau 12}^2} d\zeta \\
&= \frac{1}{2} \int_{-\frac{t}{2}}^{\frac{t}{2}} \frac{H_{\tau 22} T_{\xi\zeta}^2}{H_{\tau 11} H_{\tau 22} - H_{\tau 12}^2} \left[ \int_{-\frac{t}{2}}^{\zeta} H_{1\alpha} (B'_{1\alpha} + \zeta D'_{1\alpha}) d\zeta \right]^2 d\zeta
\end{aligned} \tag{4.23}$$

Finally, the factor  $\kappa_1$  is computed such that the strain energy due to the transverse shear stresses predicted by FSDT equals the one due to the true transverse stresses predicted by the three-dimensional elasticity theory, *i.e.*  $U_{shell} = U_{3D}$ .  $\kappa_2$  is evaluated in the similar way. For the shell structure with isotropic material,  $\kappa_1 = \kappa_2 = 5/6$ .

### 4.3 SPH implementation for multilayered shell structures

Using the continuum SPH formulation for derivatives of a function detailed in the Chapter 2, the deformation gradient and the GL strain tensor can be evaluated. Then, the generalized force vectors are determined via Eq.(4.6). The rest task of SPH implementation for multilayered shell structures, is to discretize the governing equilibrium equations using the SPH particles in its shell formulation (with only one layer of particles).

The classical dynamic equilibrium equations of a laminated composite shell structure, subjected to surface loading vector  $\mathbf{b}_L = \{b_\xi, b_\eta, b_\zeta\}^T$  are given by [102]

$$\left\{ \begin{array}{l}
\rho_m \ddot{u} + \rho_{mb} \ddot{\varphi} = N_{\xi\xi,\xi} + N_{\xi\eta,\eta} + b_\xi \\
\rho_m \ddot{v} + \rho_{mb} \ddot{\theta} = N_{\xi\eta,\xi} + N_{\eta\eta,\eta} + b_\eta \\
\rho_m \ddot{w} = T_{\xi\zeta,\xi} + T_{\eta\zeta,\eta} + b_\zeta \\
-\rho_{mb} \ddot{v} + \rho_b \ddot{\theta} = -M_{\xi\eta,\xi} - M_{\eta\eta,\eta} + T_{\eta\zeta} \\
\rho_{mb} \ddot{u} + \rho_b \ddot{\varphi} = M_{\xi\xi,\xi} + M_{\xi\eta,\eta} - T_{\xi\zeta}
\end{array} \right. \tag{4.24}$$

in which,

$$\rho_m = \sum_{k=1}^{NL} (\zeta_k - \zeta_{k-1}) \rho_k, \quad \rho_{mb} = \sum_{k=1}^{NL} \frac{1}{2} (\zeta_k^2 - \zeta_{k-1}^2) \rho_k, \quad \rho_b = \sum_{k=1}^{NL} \frac{1}{3} (\zeta_k^3 - \zeta_{k-1}^3) \rho_k. \tag{4.25}$$

As  $\rho_{mb}$  is often very small compared to  $\rho_m$  and  $\rho_b$ , therefore by neglecting this term, Equation (4.24) takes a simple form, which can be written in matrix form as follows

$$\rho_m \ddot{\mathbf{u}}_L = \text{div}_L(\mathbb{N}_L) + \mathbf{b}_L \quad (4.26)$$

$$\rho_b \ddot{\boldsymbol{\theta}}_L = \text{div}_L(\mathbb{M}_L) + \mathbf{T}_L \quad (4.27)$$

in which,

$$\mathbb{N}_L = \begin{bmatrix} N_{\xi\xi} & N_{\xi\eta} & T_{\xi\zeta} \\ N_{\xi\eta} & N_{\eta\eta} & T_{\eta\zeta} \\ T_{\xi\zeta} & T_{\eta\zeta} & 0 \end{bmatrix}, \quad \mathbb{M}_L = \begin{bmatrix} -M_{\xi\eta} & -M_{\eta\eta} & 0 \\ M_{xx} & M_{\xi\eta} & 0 \\ 0 & 0 & 0 \end{bmatrix} \quad \text{and} \quad \mathbf{T}_L = \begin{bmatrix} T_{\eta\zeta} \\ -T_{\xi\zeta} \\ 0 \end{bmatrix}. \quad (4.28)$$

One can find the reduced equations of motion for laminate is similar to ones of isotropic shell given in Chapter 3. So the successive derivation process for the discretized equilibrium equations is omitted, and the results appear to be

$$\begin{cases} \ddot{\mathbf{U}}_i = \sum_{j=1}^{N_j} \left( \frac{\mathbb{N}_{0i}}{\rho_{m0i}^2} + \frac{\mathbb{N}_{0j}}{\rho_{m0j}^2} - \mathbb{N}_{vij} \right) \nabla_0 W_{0ij} \rho_{m0j} A_{0j} + \frac{\mathbf{b}_{0i}}{\rho_{m0i}} \\ \ddot{\boldsymbol{\Theta}}_i = \sum_{j=1}^{N_j} \left( \frac{\mathbb{M}_{0i}}{\rho_{b0i}^2} + \frac{\mathbb{M}_{0j}}{\rho_{b0j}^2} \right) \nabla_0 W_{0ij} \rho_{b0j} A_{0j} + \frac{\mathbf{T}_{0i}}{\rho_{b0i}} \end{cases} \quad (4.29)$$

where  $\mathbb{N}_v$  is the viscous forces written in the global coordinates.

## 4.4 Numerical applications

In this section, some numerical applications of multilayered composite shell involving geometrically nonlinear behavior are presented and the obtained results using the shell-based SPH method are compared with those of reference (analytical and FE results obtained using ABAQUS<sup>®</sup>).

### 4.4.1 A clamped square plate under uniform pressure load

As a first application, an example of a clamped multilayered square plate is studied. The plate is subjected to a uniform pressure  $q_0 = 1.2 \text{MPa}$ . Its geometrical data correspond to a side length of  $a = b = 200 \text{mm}$  and a thickness of  $t = 2.69 \text{mm}$  (see Figure 4.4). Each ply is made of the unidirectional fiber-reinforced composite with the following properties:

$$E_L = 25 E_T, \quad E_T = E_Z = 6894.95 \text{MPa}, \quad G_{LT} = G_{LZ} = 0.5 E_T,$$

$$G_{TZ} = 0.2 E_T, \quad \nu_{LT} = 0.25, \quad \rho = 1600 \text{kg/m}^3.$$

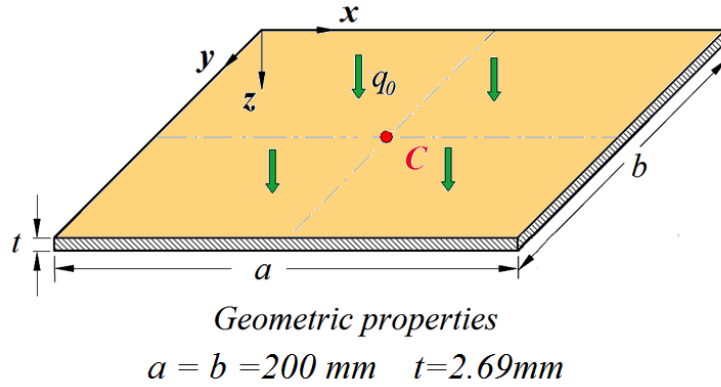


Figure 4.4: Geometry of the square plate

Three symmetric cross-plyes such as:  $(0^\circ)$ ,  $(0^\circ/90^\circ/0^\circ)$ ,  $(0^\circ/90^\circ/0^\circ/90^\circ/0^\circ)$  and three antisymmetric stack sequences:  $(0^\circ/90^\circ)$ ,  $(0^\circ/90^\circ/0^\circ/90^\circ)$ ,  $(0^\circ/90^\circ/0^\circ/90^\circ/0^\circ/90^\circ)$  are studied.

This example has been studied by Mavel [125] using a geometrically linear analysis by means of semi-analytical solution based on the Fourier series decomposition. In the following geometrically nonlinear effects are taken into account and the obtained results of the present shell-based SPH model are compared with the reference solution of ABAQUS<sup>®</sup>. Due to the symmetry, a quarter of the plate neutral surface is modeled using  $21 \times 21$  SPH particles while the FE mesh used in ABAQUS<sup>®</sup> corresponds to  $20 \times 20$  quadrilateral shell elements of various types (S4, S4R and S8R) in implicit static and explicit dynamics formulations. The vertical displacement  $W_C$  at the centroid of the plate is taken as a criterion for comparison. A summary of results obtained at point  $C$  is given in Table 5.2.

Table 4.1: Vertical displacement of the central point  $W_C$  (mm)

Stack sequence	SPH	FEM(S4)	FEM(S4R)	FEM(S8R)
$(0^\circ)$	5.329	5.159	5.159	5.146
$(0^\circ/90^\circ)$	6.077	5.955	5.958	5.937
$(0^\circ/90^\circ/0^\circ)$	5.661	5.560	5.562	5.541
$(0^\circ/90^\circ/0^\circ/90^\circ)$	5.895	5.812	5.815	5.790
$(0^\circ/90^\circ/0^\circ/90^\circ/0^\circ)$	5.769	5.675	5.678	5.654
$(0^\circ/90^\circ/0^\circ/90^\circ/0^\circ/90^\circ)$	5.857	5.768	5.771	5.746

After a first analysis of Table 5.2, one can observe the very good overall solutions obtained

using the proposed shell-based SPH model. FE results obtained using either implicit static (S8R) or explicit dynamics (S4R, S4), show almost the same stable deflection values. We can also remark the very good accuracy of solutions obtained using the developed SPH model, even for a high number of layers, with a maximum error less than 3.5%.

#### 4.4.2 A hinged multilayered square plate under uniform load

The second application deals with a hinged 4-layer symmetric cross-ply ( $0^\circ / 90^\circ / 90^\circ / 0^\circ$ ) square plate. Different ratios of length to thickness  $L/t$  of 40, 20, 10 are considered [126–128]. A pressure load  $q_0$  is controlled using the factor  $q_0 L^4 / E_T t^4$  of 50, 100, 150, 200, 250 and imposed uniformly on the plate. The length remains fixed to  $L = 200\text{mm}$ , and the material data of each ply is assumed to be the same as in the previous application.

For simplicity reason, a  $21 \times 21$  particles' distribution is used to model a quarter of the plate. The non-dimensional central deflections  $W_C/t$  are listed in the Table 4.2 and compared with the FE results using high-order element HOST [127] and with analytical solutions [128].

Table 4.2: Non-dimensional deflection of the centroid of the plate  $W_C/t$

$\frac{q_0 L^4}{E_T t^4}$	L/t=40			L/t=20			L/t=10		
	SPH	HOST	Analytical	SPH	HOST	Analytical	SPH	HOST	Analytical
50	0.313	0.293	0.293	0.329	0.320	0.320	0.371	0.360	0.356
100	0.486	0.464	0.464	0.500	0.493	0.486	0.535	0.520	0.510
150	0.603	0.582	0.582	0.614	0.592	0.592	0.644	0.624	0.610
200	0.692	0.658	0.664	0.701	0.680	0.680	0.728	0.696	0.689
250	0.765	0.738	0.738	0.773	0.752	0.752	0.798	0.760	0.747

As in the first application, results given in Table 4.2 show a very good agreement between results obtained using the proposed SPH model and those of reference. This remark remain valid for thin as well as thick structure, which proves the robustness of the shell-based SPH technique.

#### 4.4.3 Laminated strip under three-point bending

The structure presented here is a seven-layer, composite, orthotropic, rectangular strip that is simply supported on its supports on A and B and subjected to a line load of  $10\text{N/mm}$

at  $C$  onto the top surface, showed in Figure 4.5.

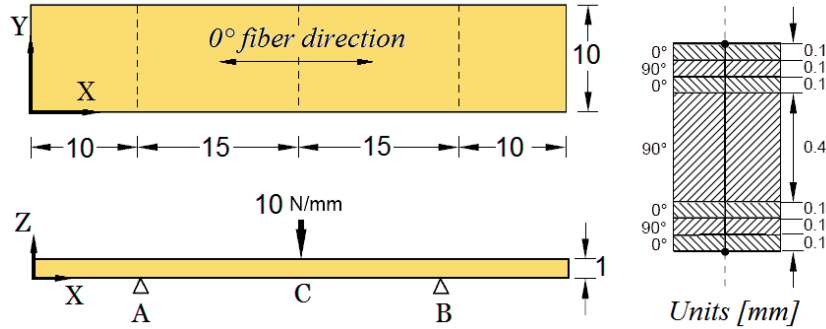


Figure 4.5: Geometry and loading of the laminated strip

The layers are oriented at  $(0^\circ/90^\circ/0^\circ/90^\circ/0^\circ/90^\circ/0^\circ)$  sequentially with respect to AB edge.

Each ply has the material properties given by

$$E_L = 100000 \text{ MPa}, E_T = E_Z = 5000 \text{ MPa}, G_{LT} = G_{LZ} = 3000 \text{ MPa},$$

$$G_{TZ} = 2000 \text{ MPa}, \nu_{LT} = 0.4, \rho = 1600 \text{ kg/m}^3.$$

The whole laminated strip is modeled using mapped discretizations with the same space between particles (nodes) in both  $X$  and  $Y$  directions. Our numerical results are compared with the reference solution given by NAFEMS [129] and a second verification is done using a comparison with the results obtained thanks to the S4R shell element of ABAQUS<sup>®</sup> explicit dynamics. Table 4.3 summarizes the deflection of the central point  $C$  using different discretizations.

Table 4.3: Convergence of the laminated strip deflection  $W_C$

Number of particles or nodes in the width direction	$W_C$ (mm)	$W_C$ (mm)
	Present model	ABAQUS <sup>®</sup> Explicit (S4R)
3	-1.435	-1.024
4	-1.219	-1.042
6	-1.159	-1.050
8	-1.130	-1.053
10	-1.112	-1.055
20	-1.077	-1.059
40	-1.068	-1.063
NAFEMS	-1.060	-1.060

The deformed configurations of which the width is discretized using 10 particles or nodes by SPH method and FEM are presented in Figure 4.6.

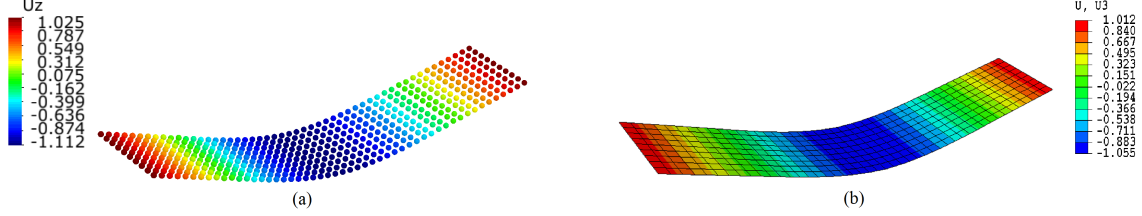


Figure 4.6: Deformed configuration of the laminated strip : (a) SPH model (b) FE model (ABAQUS<sup>©</sup>)

As we can observe from Figure 4.6, the overall deformed shape of the laminated strip obtained using the developed SPH model is very similar to the one obtained using the S4R shell FE model of ABAQUS<sup>©</sup>. From Table 4.3 we can also remark that the predicted values of the strip deflection using refined discretization (40 particles) are in good agreement with the reference solution of NAFEMS. However for this structure, we observed also a relatively slower convergence of the present SPH model when compared with the FE convergence process of the S4R shell element of ABAQUS<sup>©</sup>.

#### 4.4.4 Composite shallow cylindrical shell with a central point load

In the present application, we investigate the buckling behavior of a composite flat cylindrical segment subjected to a central pinching force. The shallow shell is hinged along its straight edges and free on the other edges as shown in Figure 4.7.

The geometric data are:  $L = 254mm$ ,  $R = 2540mm$ ,  $t = 12.6mm$ ,  $\phi = 0.1rad$ . This problem has been studied by Laschet and Jeusette [130], Brank *et al.* [131], Balah and Al-Ghamedy [132]. The roof is built up by a layer-up of 12 plies with ply thickness  $t_P = 1.05mm$ . In order to investigate the layer-up effects on the solution, two stacking sequences are studied: (i)  $(90_4^{\circ}/0_4^{\circ}/90_4^{\circ})$  and (ii)  $(0_4^{\circ}/90_4^{\circ}/0_4^{\circ})$ , where the  $0^{\circ}$  means that the fiber orientation is in the circumferential direction. The carbon-epoxy layer owns the following properties:

$$E_L = 3300MPa, E_T = E_Z = 1100MPa, G_{LT} = G_{LZ} = 660MPa,$$

$$G_{TZ} = 660MPa, \nu_{LT} = 0.25, \rho = 1400kg/m^3.$$

Due to the symmetry of the problem, only one quarter of the shell is modeled using  $21 \times 21$  SPH particles. The numerical results concerning the deflection at the central point load

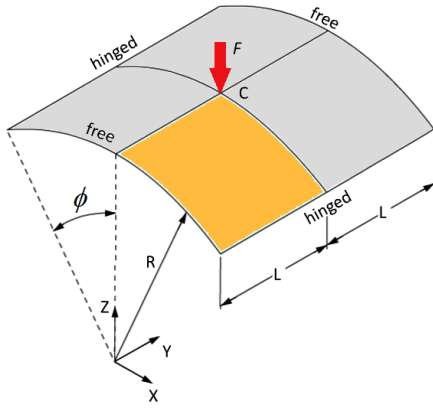


Figure 4.7: Composite shallow cylindrical shell

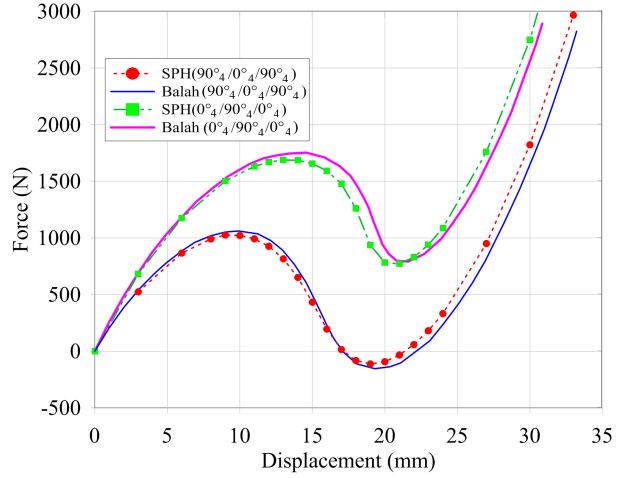


Figure 4.8: Load-displacement curve

location are reported in Figure 4.8, together with the solution from [132] using a four-node isoperimetric laminated shell element based on a cubic displacement field over the shell thickness.

For the case (i), the critical buckling load predicted using the present SPH model is  $F_{cr} = 1022.27N$  with a deflection corresponding to  $W_C = 9.9mm$ , while the reference critical buckling load is  $F_{cr} = 1061.18N$  obtained for the same deflection [132]. A first comparison of the buckling load values, shows that the proposed SPH model underestimates the solution with an error less than 3.7% which is very acceptable. From Figure 4.8, a comparison of the whole load-displacement history shows that the SPH solution is very close to the reference, even for large deformations.

For the case (ii), the predicted critical buckling load obtained using the SPH model is  $F_{cr} = 1684.83N$  while the reference solution corresponds to  $F_{cr} = 1753.16N$ , both obtained for a deflection of  $W_C = 14mm$ . As for the previous case, the error of the predicted buckling load by the SPH model presents a small error which remains less than 3.8% which is very satisfactory.

A general analysis of the post-buckling response of the composite shallow cylindrical shell given in Figure 4.8, shows that the structure of case (ii) possess higher resistance to buckling than the case (i). This can be explained simply by the number of fibers orientated in the  $0^\circ$  direction, much greater in case (ii) than in case (i). The good agreement of the solution predicted by the SPH model and the reference, proves that the SPH method may be used



as a good technique for the post-buckling analysis of nonlinear behavior of composite shells.

#### 4.4.5 Laminated dome under concentrated load

In the last application, nonlinear analysis of a thin spherical shell segment is carried out using the proposed SPH model. The studied laminated dome is depicted in Figure 4.9 in which the shell is simply supported at all four edges. The geometrical properties are: radius  $R = 10m$ , the side length of the projected plane consisted of the four vertex  $a = b = 0.9996m$  and the total thickness of the laminated composite shell structure  $t = 0.01m$ . This problem has been investigated by To and Wang [133].

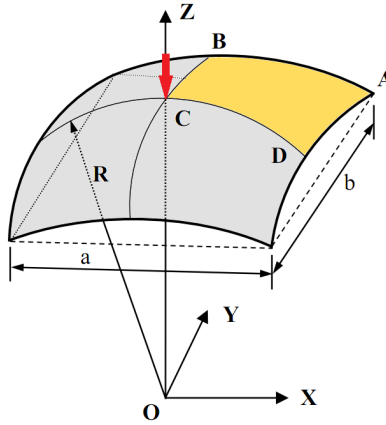


Figure 4.9: Geometry of the spherical shell segment

The spherical shell is composed of two equal thickness layers oriented at  $(-45^\circ / +45^\circ)$ . Each layer has the following material properties

$$E_L = 2.5 \times 10^{11} Pa, E_T = E_Z = 1.0 \times 10^{10} Pa, G_{LT} = G_{LZ} = 0.5 \times 10^{10} Pa, \\ G_{TZ} = 2.5 \times 10^{10} Pa, \nu_{LT} = 0.25, \rho = 10^3 kg/m^3 .$$

For simplicity reasons, one quarter of the shell is modeled using  $21 \times 21$  SPH particles. The same structure is analyzed using a FE model of ABAQUS<sup>©</sup> which will constitute a reference solution for comparison purpose. The FE model consists of  $20 \times 20$  S4R shell elements using the implicit static analysis. The loading condition corresponds to a concentrated force applied in the negative  $z$ -direction on the top point  $C$  of the dome.

Figure 4.10 shows the nonlinear response of the dome represented by the load-deflection curve at point  $C$ . As we can observe the nonlinear behavior of the dome is captured accurately and the predicted deflection is in a good agreement when compared to the FE solution obtained using S4R shell element of ABAQUS<sup>©</sup>. The final deformed dome is

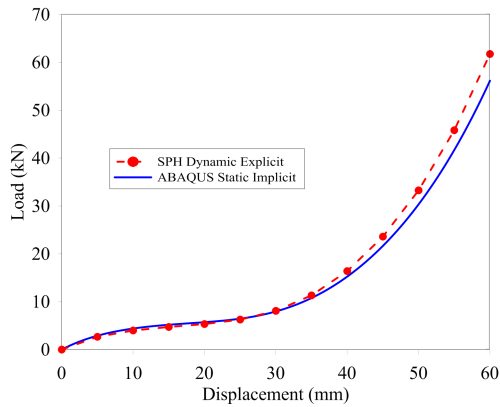


Figure 4.10: Load-displacement curve at point C

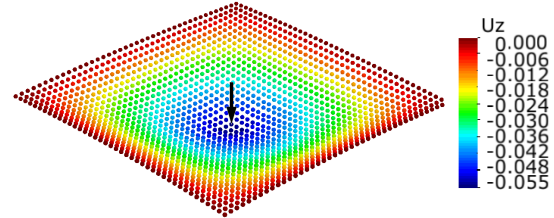


Figure 4.11: Deformed configuration

shown in Figure 4.11 where only one layer of SPH particles are capable of representing the nonlinear behavior of the structure.

## 4.5 Conclusion

In this Chapter we presented a new shell-based SPH model for the study of thin multilayered composites structures. The present model is based on the First-Order Shear Deformation Theory which has been proven to be efficient in solving problems involving thin/thick shell structures. Based on the Mindlin-Reissner assumption, the classical SPH method has been modified to reproduce the laminated shell behavior, by modeling the stacking of a thin shell structure with only one layer of particles located into the shell mid-surface.

Several numerical benchmarks involving bending and buckling of laminated structures have been treated successfully using the developed shell-based SPH model. The obtained results were compared to the reference solutions taken from the literature as well as to numerical reference solution of the FE using ABAQUS<sup>®</sup> software. It has been shown, through the numerical applications that the shell-based SPH method using only one layer of particles is very suitable for the study of laminated composite structures undergoing large transformations and therefore the present approach may constitute a good alternative to the classical FE method.

# *Low velocity impact and failure modeling of composite shells using the SPH method*

---

In this chapter, the nonlinear shell-based SPH method detailed in the previous two chapters is extended to investigate the dynamic response of the isotropic and laminated shell structures, subjected to low velocity impacts by rigid spherical projectiles. A simplified contact force between the projectile and the shell structure is estimated thanks to the Hertzian law. The transient response of the system (projectile and the structure) are evaluated using the developed shell-based SPH method incorporating first-order shear deformation theory. The effects of the shell thickness, stacking sequence, the projectile mass and velocity on the global impact solution are studied by virtue of some standard benchmarks with available reference solutions from literature. The progressive failure analysis is also conducted by using the popular Tsai-Wu failure criterion.

## **5.1 Brief overview on shell impact modeling**

Multilayered shell structures are very susceptible to low velocity transverse impacts caused by various foreign objects, which still restrains their use in the engineering applications. Such impact events can cause significant devastations in thin composite shell structures, such as the intralaminar damage (matrix cracks, fiber/matrix debonding and fiber breakage) and interlaminar failure, which develops at the interface between adjacent plies in the form of debonding between layers which is known as *delamination*. Therefore, there is a strong need to clearly understand their dynamic response to transient dynamic loading. Through the literature, we find a large number of studies that have been conducted to determine the dynamic properties of laminated structures, in terms of experimental investi-

gations [134,135], or analytical [136,137], and numerical works [138,139]. For instance, Yang and Sun [134] presented the experimental indentation law through static indentation tests on composite laminates. Pierson and Vaziri [140] proposed an analytical model based on the combined effects of shear deformation, rotary inertia and the nonlinear Hertzian contact law. Hertzian contact was modified by Sun [141] for low velocity impact response analysis of composite laminates. Choi *et al.* [138] proposed a linearized contact law and compared low velocity impact response on composite laminates to modified Hertzian contact law. Based on the Rayleigh-Ritz method, Nallim and Grossi [142] presented the free transverse vibration analysis of symmetrically laminated solid and annular elliptic and circular plates. Two simple and improved models, namely the energy-balance model and the spring-mass model [144, 145, 152] are popularly applied to calculate impact force and duration during low velocity impact of circular composite plates. Olsson [146] presented an approximate solution for wave-controlled impacts, similar to impact on infinite plates.

A FE model of the higher-order shear deformation theory is used to study the response of graphite/epoxy laminated composite non-prismatic folded plates subjected to impacting loads [147]. Low velocity impact analyses of general fiber reinforced laminated composites was carried out using the FE method based on three-dimensional elasticity coupling with layerwise laminated plate theory [139].

In this chapter, the proposed shell-based SPH method is developed for the analysis of low velocity impact of multilayered composite shell structures based on the first-order shear deformation theory. The projectile is assumed to be a spherical rigid body, and the contact force is estimated using the Hertzian law. Both kinematics and deformation of the impacted shell structures are studied and compared to reference solution to show the effectiveness of the present SPH method.

## 5.2 Modeling of contact force and indentation

In the following we assume that the projectile is a rigid body of a spherical shape. If two solid bodies enter in contact between each other, deformation takes place at the contact zone and a contact force emerges. If the contact force can be estimated a priori, then the conventional stress-strain analysis presented in the previous chapters can be used to describe the deformation process of a shell structure. Due to this fact, the contact *force-indentation* relationship has gained lots of interests from researchers.

The most famous contact law was developed by Hertz [148] for the contact of two deformable spheres of elastic isotropic materials. As showed in Figure 5.1, an elastic sphere of radius  $R_1$  impacts on another elastic one with radius  $R_2$ , and contact occurs in a circle zone of radius  $a$  where the normal pressure  $p$  varies as

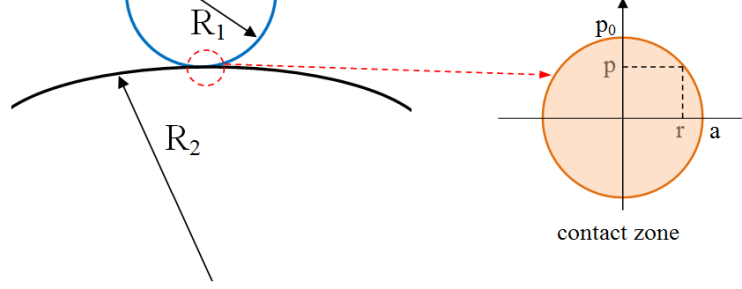


Figure 5.1: Impact problem of two deformable spherical bodies

$$p = p_0 \left( 1 - \left( \frac{r}{a} \right)^2 \right)^{1/2} \quad (5.1)$$

where  $p_0$  is the maximum contact pressure at the center of the contact zone and  $r$  is the radial position of the point in the contact zone. The contact force  $F$  can be obtained by integrating the contact force  $p$  in the contact area

$$F = \int_A p dA = \int_0^a p \, 2\pi r dr = \frac{2}{3} \pi a^2 p_0 \quad (5.2)$$

Following the derivation from [149], the radius of the contact zone is related to the contact force by

$$a = \left( \frac{3RF}{4E} \right)^{1/3} \quad (5.3)$$

where  $R$  and  $E$  are defined by

$$\frac{1}{R} = \frac{1}{R_1} + \frac{1}{R_2} \quad (5.4)$$

$$\frac{1}{E} = \frac{1 - \nu_1^2}{E_1} + \frac{1 - \nu_2^2}{E_2} \quad (5.5)$$

and  $E_1$ ,  $\nu_1$  and  $E_2$ ,  $\nu_2$  are Young's modulus and Poisson's ratios of the two colliding bodies respectively.

The difference between the displacement of the projectile and the one at the back face of the shell surface, is the *indentation*  $h_c$  (see Figure 5.2), which is calculated using

$$h_c = \frac{a^2}{R} = \left( \frac{9}{16R} \left( \frac{F}{E} \right)^2 \right)^{1/3} \quad (5.6)$$

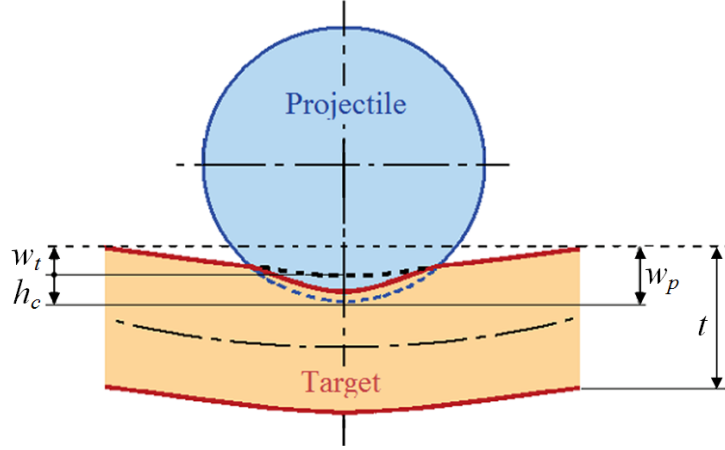


Figure 5.2: Indentation produced by the impact

Correspondingly, the contact force-indentation relationship can be written as

$$F = k_c h_c^{3/2} \quad (5.7)$$

where  $k_c$  is defined as Hertzian contact stiffness and  $k_c = \frac{4}{3}ER^{1/2}$  for two isotropic bodies. For the impact problem of a spherical projectile on laminated composite plate, the contact stiffness is modified by Sun *et al.* [141],

$$k_c = \frac{4}{3} \frac{R_p^{1/2}}{(1 - \nu_p^2)/E_p + 1/E_T} \quad (5.8)$$

where  $R_p$ ,  $E_p$  and  $\nu_p$  are local radius, Young's modulus and Poisson's ratio of the projectile, respectively.  $E_T$  is the transverse Young's modulus of the fiber-reinforced composite.

Considering a normal impact on a shell structure with a spherical projectile of a mass  $m_p$  and an initial velocity  $\dot{W}_p^0$  (along  $z$ -axis), the dynamic equilibrium equations of the structure can be solved by the developed Shell-based SPH method detailed previously. The motion of the projectile controlled by the Hertzian contact force can be stated as

$$m_p \ddot{W}_p(T) + F(T) = 0 \quad (5.9)$$

where  $T$  is time,  $W_p$  is the displacement of the projectile in the normal direction to the shell structure.

Recalling the central difference time integration method exposed in Chapter 2, the updating procedure for the projectile displacement by assuming the absence of any damping forces, can be written as

$$W_p^{n+1} = 2W_p^n - W_p^{n-1} + \Delta T^2 \ddot{W}_p^n \quad (5.10)$$

which can be self-started using

$$W_p^{-1} = W_p^0 - \Delta T \dot{W}_p^0 + \frac{\Delta T^2}{2} \ddot{W}_p^0 \quad (5.11)$$

### 5.3 Modeling of progressive failure modeling using SPH

Generally, the impact modeling of composite structures can be categorized into low and high velocity impact [150]. However, there exist no clear and defined transition frontier between low and high velocity, which is dependent on several parameters (material properties, projectile mass, shape,...). Following the literature, usually a limited velocity is known to be within the range of  $[10 - 100]m/s$ . Different damage models can be introduced within this family of impact events [143, 151]. In the high velocity impact, the incident energy is dissipated in a small zone resulting of a localized damage. Hence, high velocity impact is characterized by penetration and perforation induced by fiber breakage. However, damage produced in the low velocity impacts is generally initialed by matrix cracks which induce delamination at the interfaces between plies with different orientations. Fiber breakage is generally confined into the region under and near the contact zone between the projectile and the laminate [153]. Such damages are very difficult to detect by visual inspections and can cause significant reductions in the strength and stiffness of the materials.

Through the literature, numerous research publications have been devoted to the damage prediction of composite laminates subjected to low velocity impacts. For instance, based on experimental observations [154] and 3D finite element analysis [155], Choi *et al.* concluded that intraply matrix cracking constitute the initial damage mode and delamination starts initiating when the matrix crack reaches the interface between the ply groups having different fiber orientations. They also reported in their work expressions of the degenerated material properties of the matrix after cracking.

Choi and Chang [156] found that the delamination can result from the point-nose impact that appears in a peanut shape. They proposed a double failure criterion identifying separately, the matrix rupture and delamination. The main limitation of these criteria is the use of a parameter obtained only from experimental results. Ganapathy and Rao [157] used a 4-noded and 48 degree-of-freedom double curved quadrilateral shell element for predicting the damage of laminated composite panels of cylindrical/spherical shapes subjected to low-velocity impacts. The damage at each integration point within an element is predicted using the Tsai-Wu quadratic failure criterion. The mode of the damage is identified using

the maximum stress criterion and the corresponding reduced material properties are then included.

The classical Fourier series was also used in the investigation of the impact response and damage modeling in laminated composite cylindrical shells [158]. Based on Tsai-Wu quadratic failure criterion, Zhao and Cho [159] used the Tsai's criterion together with an additional delamination model evaluated at all of the quadrature points, of a three-dimensional eight-node non-conforming element, for the prediction of the three damage modes and progressive failure of curved laminates.

In the present investigation, the quadratic Tsai-Wu failure criterion [160, 161] will be adopted in the context of SPH modeling. This choice may be justified by the fact that Tsai-Wu failure criterion, still one of the most popularly failure criteria that are used for orthotropic materials and gives satisfactory results for brittle failure. This macroscopic failure criterion presents a form of scalar function of two strength tensors and takes into account the difference in strengths due to positive and negative stresses.

For example in particular case of unidirectionally reinforced lamina in a plane stress state, the Tsai-Wu criterion can be formulated for each ply as follows

$$F_1\sigma_{LL} + F_2\sigma_{TT} + F_{11}\sigma_{LL}^2 + F_{22}\sigma_{TT}^2 + F_{33}\tau_{LT}^2 + 2F_{12}\sigma_{LL}\sigma_{TT} \leq 1 \quad (5.12)$$

where  $\sigma_{LL}, \sigma_{TT}, \tau_{LT}$  are the in-plane stress described in the principle material direction. For each ply, they are obtained by the linear elastic constitutive relationship.  $F_i$  and  $F_{ij}$  ( $i, j = 1, 2, 3$ ) are strength parameters, which have to be determined by tensile, compressive and shear experimental tests,

$$\begin{aligned} F_1 &= \frac{1}{X_t} - \frac{1}{X_c}, & F_2 &= \frac{1}{Y_t} - \frac{1}{Y_c} \\ F_{11} &= \frac{1}{X_t X_c}, & F_{22} &= \frac{1}{Y_t Y_c} \\ F_{33} &= \frac{1}{S^2}, & F_{12} &= -\frac{1}{2\sqrt{F_{11}F_{22}}} \end{aligned} \quad (5.13)$$

where  $X_t, X_c$  are the strength of the lamina in the fiber direction in tension and compression,  $Y_t, Y_c$  are the strength of the lamina in the transverse direction in tension and compression and  $S$  is the shear strength of the lamina.

However, Tsai-Wu failure criterion is just a phenomenological failure criterion because only the occurrence of failure is predicted, not the mode of failure. Since the propagation of impact-induced damage strongly depends on the damage modes, an additional criterion for differentiating the damage types is needed. Hou *et al.* [162] summarized the stress-based



failure criteria for matrix cracking, matrix crushing, fiber failure and delamination along with the corresponding strategy of updating stresses. An equivalent strategy for updating elastic constants was proposed by Li *et al.* [163] to simulate the low-velocity impact damage in a composite lamina by using a 9-node Lagrangian Mindlin plate element.

In the present investigation, matrix cracking and fiber breakage but delamination are considered and identified through the use of maximum stress criteria as suggested in [157, 159]. The originality will reside in the coupling between the former failure model with the context of composite SPH-shell modeling. Therefore the material properties at the SPH particles where failure is detected, are degraded during the calculation and the modified properties are updated during the nonlinear analysis.

After the Tsai-Wu failure criterion is saturated *i.e.* reaches the value 1, the damage mode would be identified:

- For tensile stress:

$$\sigma_{LL} > X_t \text{ fiber failure}$$

$$\sigma_{TT} > Y_t \text{ matrix cracking (transverse tension splitting)}$$

$$|\tau_{LT}| > S \text{ matrix cracking (shear splitting)}$$

- and for compressive stress:

$$\sigma_{LL} < -X_c \text{ fiber failure (crushing)}$$

$$\sigma_{TT} < -Y_c \text{ matrix cracking (crushing)}$$

When matrix cracked, degraded material properties at failed layer point are set by the zero elastic constants  $E_{TT}$ ,  $G_{LT}$  and  $\nu_{LT}$ . On the other hand, when fiber breakage occurs, the elastic constants  $E_{LL}$ ,  $E_{TT}$ ,  $G_{LT}$ , and  $\nu_{LT}$  are nullified.

## 5.4 Low-velocity impact analysis

### 5.4.1 Impact of a clamped isotropic plate by a steel sphere

The first application studied here is an isotropic square plate subjected to an impact induced by a steel ball at its center (Figure 5.3). The plate is clamped at all edges. The geometrical and material parameters of the projectile and target plate are summarized in Table 5.1.

The transient solution of this problem, in terms of the impacting force, displacements and velocity at the centroid of the plate and projectile were given by Karas [164]. This problem

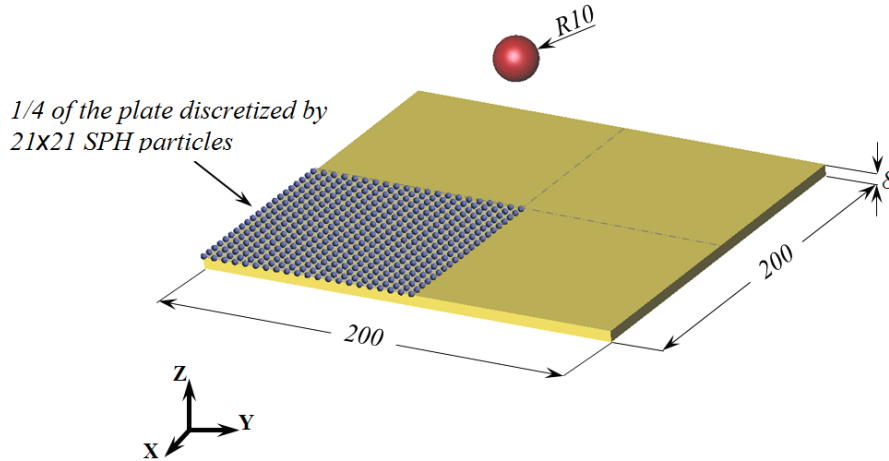


Figure 5.3: Impact of a clamped isotropic plate by a steel sphere

Table 5.1: Geometrical and material parameters of the projectile and target plate

Parameters	
Target	Steel plate, clamped
	Dimensions: $200\text{mm} \times 200\text{mm} \times 8\text{mm}$
	Material properties: $E_t = 210\text{GPa}$ , $\nu_t = 0.3$ , $\rho_t = 7800\text{kg/m}^3$
Projectile	Steel ball
	Radius: $R_p = 10\text{mm}$
	Mass: $M_p = 32.67\text{g}$ (full solid)
	Impact velocity: $1\text{m/s}$
	Material properties: $E_p = 210\text{GPa}$ , $\nu_p = 0.3$ , $\rho_p = 7800\text{kg/m}^3$
	Hertzian contact stiffness: $k_c = \frac{\frac{4}{3}\sqrt{R_p}}{(1 - \nu_p^2)/E_p + 1/E_t} = 4.636 \times 10^5 \text{N/m}^{3/2}$

has also been investigated by Mahajana and Dutta [165] using three different FE mesh discretizations (9, 208 and 569 eight-noded degenerate shell finite elements for a quarter part of the laminate) to conduct the convergence test. In the present investigation, we considered the finest mesh of [165] as a reference solution for comparison purpose. It has to be noticed that another study of this problem, using 8-node brick element and direct Gauss quadrature integration scheme, has been conducted by Wu and Chang [166] but not covered here.

In the present shell-based SPH impact model, and due to the symmetry of the problem, only a quarter of the plate is modeled using a uniform discretization of  $21 \times 21$  particles

(see Figure 5.3). The total simulation time for this problem has been fixed to  $100\mu s$ . The nonlinear transient analysis has been carried out using our shell-SPH model with the explicit dynamics for the time integration scheme as described in the previous chapters. The impact load predicted using our shell-SPH model is depicted in Figure 5.4 and compared to the reference solutions of Karas [164] and Mahajana and Dutta [165].

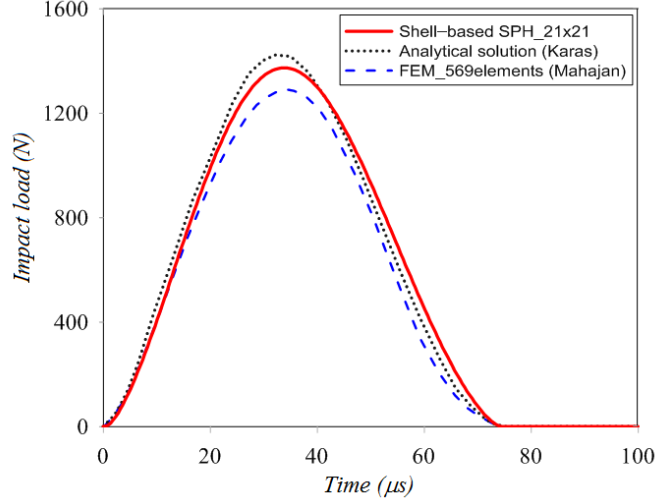


Figure 5.4: Evolution of the impact load vs. time

The analytical solution given in [164] predicts a maximum impact load of  $1383.99N$  occurring at  $33\mu s$  and a total duration of contact between the ball and the target of approximately  $73\mu s$ . The present shell-based SPH model predicts a maximum impact load of  $1373.7N$  at  $34\mu s$ , while the FE model of Mahajana and Dutta [165] gives an impact load of  $1291.1N$  at  $33.7\mu s$ . Therefore by comparing the accuracy of the SPH model to the analytical solution, we conclude that the present SPH model provides a more precise solution than the FE model of Mahajana and Dutta [165] for almost the same discretization. The solution error of the present shell-SPH model is very small about 0.74% in the prediction of the maximum impacting force and about 3.03% and 2.05% in the prediction of impacting time and total duration of contact respectively.

Figure 5.5 shows the evolution of the velocity of the projectile and the centroid of the target *vs.* time. As one can observe, the velocity of the centroid of the plate starts from 0 (resting at initial conditions) and then increases until reaching a maximum value of  $0.21m/s$  at  $34\mu s$  of time which is the same as the projectile velocity, precisely when the contact force reaches its maximum. Starting from this moment, the projectile starts to slow down to

Table 5.2: Comparison of the impact load (SPH vs. FE and Analytical solutions)

	Analytical [164]	FEM [165]	Shell-SPH
Maximum impact load ( $N$ )	1383.99	1291.1	1373.7
Error on load (%)	–	-6.71	-0.74
Time at maximum load ( $\mu s$ )	33	33.7	34
Error on time (%)	–	2.12	3.03
Total duration of impact ( $\mu s$ )	73	74.8	74.5
Error on total duration (%)	–	2.47	2.05

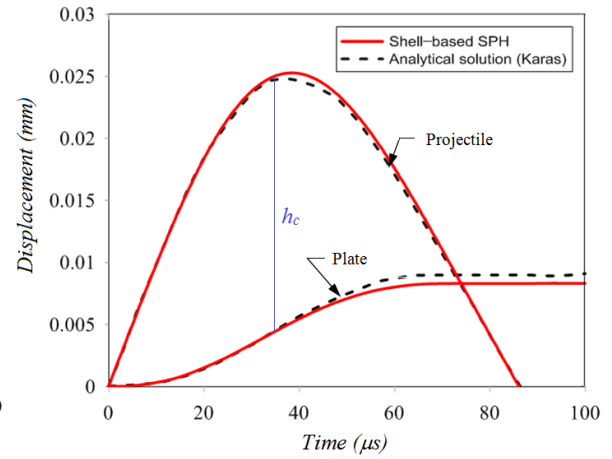
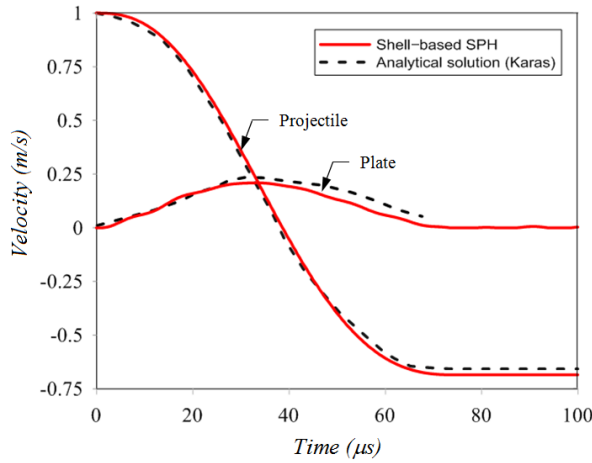


Figure 5.5: Evolution of the velocity of the projectile and the plate centroid). Figure 5.6: Evolution of the projectile stroke and the target centroid deflection.

change the sign of it's movement, resulting a maximum indentation (see Figure 5.6) and a maximum impact load predicted using the Hertzian contact law.

The contact between the projectile and the target, ends at  $74.5\mu s$  when the projectile and the centroid of the plate experienced the same displacement. After the impact, the projectile returns back with a constant velocity of  $0.685m/s$ , which implies that the final kinetic energy of the projectile is only 47% of its kinetic energy before impact, therefore 53% of its energy has been absorbed by the plate. The plate undergoes free vibrations after contact ceases (see Figure 5.7), and a continuous exchange is introduced between the kinetic energy and the strain energy with the sum remaining constant.

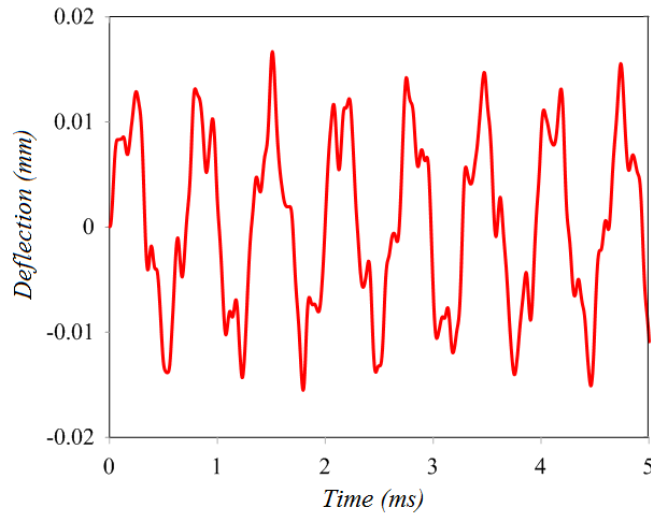


Figure 5.7: Evolution of the target deflection *vs.* time at the impact point.

#### 5.4.2 Impact of a T300/934 carbon-epoxy plate by a steel sphere

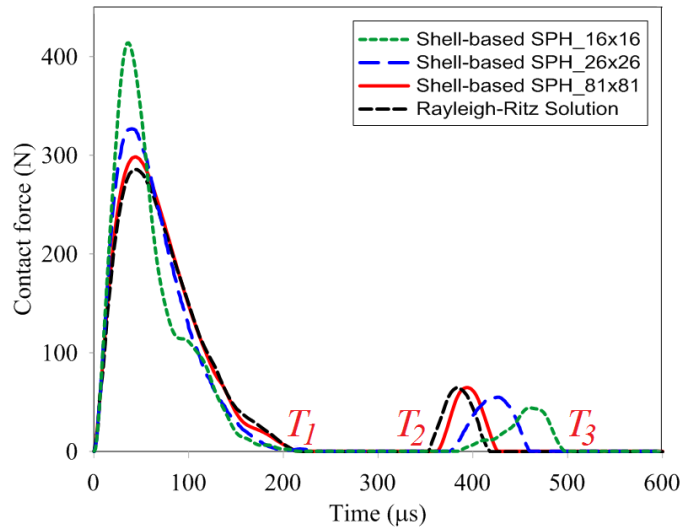
The second application consists of center impact of a simply supported composite plate made of T300/934 carbon-epoxy, by a spherical ball made of steel. This problem was investigated initially by Qian and Swanson [167] using the Rayleigh-Ritz method coupled to the Newmark algorithm for the time integration. Abrate [144] proposed a procedure starting by a infinite plate assumption and solving a single nonlinear, ordinary differential equation which governs the non-dimensional indentation. Both techniques are based on the nonlinear Hertzian contact law. The material and geometrical properties of the projectile and the plate are summarized in Table 5.3.

The first task is to explore the prediction of the impact force between the projectile and the plate with a thickness  $t = 2.69\text{mm}$ . A quarter of the target plate was discretized using three types of particle sizes:  $6.67\text{mm}$ ,  $5\text{mm}$  and  $4\text{mm}$ . The number of particles are  $16 \times 16$ ,  $21 \times 21$  and  $26 \times 26$  respectively. The total simulation time for the impact modeling was fixed to  $600\mu\text{s}$ . As in the previous application, the nonlinear transient analysis has been carried out using our shell-SPH model with the explicit dynamics scheme for the time integration. The obtained impact load using our shell-SPH model is shown in Figure 5.8 and compared to the reference solution of Qian and Swanson [167].

As a first observation of Figure 5.8, the impact force history predicted using our shell-SPH model is in good agreement with the semi-analytic solution [167]. Two impacts occur between the projectile and the plate. The results of the maximum impact force  $F_{max}$ , the

Table 5.3: Geometrical and material parameters of the projectile and the target

Parameters	
Target	$[0/90/0/90/0]_s$ T300/934 carbon-epoxy plate, simply supported Plate size: $200mm \times 200mm$ Plate thickness: (A) $t = 2.69mm$ (B) $2t = 5.38mm$ (C) $4t = 10.76mm$ Material properties: $E_{11} = 120GPa, E_{22} = 7.9GPa, G_{12} = G_{23} = 5.5GPa$ $\nu_{12} = \nu_{23} = 0.3, \rho = 1580kg/m^3$
-----	
Projectile	Steel ball Radius: $R_p = 6.35mm$ Mass: $M_p = 8.537g$ (full solid) Impact velocity: $3m/s$ Material properties: $E_p = 210GPa, \nu_p = 0.3, \rho_p = 7960kg/m^3$ Hertzian contact stiffness: $k_c = 8.394 \times 10^8 N/m^{3/2}$

Figure 5.8: Evolution of the impact load *vs.* time (plate of thickness  $t$ )

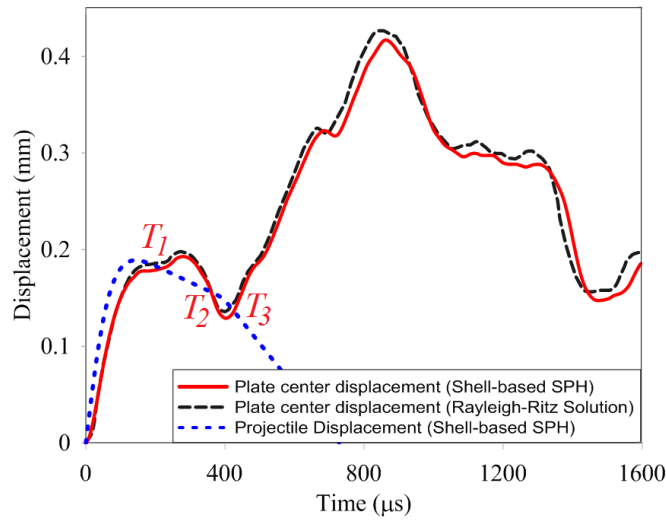
total duration time  $T_1$  of the first impact, the starting time  $T_2$  and the ending time  $T_3$  of the second impact are summarized in Table 5.4.

From Table 5.4, we can observe that the result of the finest SPH discretization is close to the semi-analytical solution given in [167], with an error of 13.91% on the maximum

Table 5.4: Comparison of the impact load (SPH *vs.* semi-analytical solution)

	Semi-analytical [167]	Shell-SPH $16 \times 16$	Shell-SPH $26 \times 26$	Shell-SPH $81 \times 81$
Maximum impact load $F_{max}(N)$	286.8	413.8	326.7	298.5
Error on $F_{max}$ (%)	–	44.28	13.91	4.09
Duration of first impact $T_1(\mu s)$	219.1	215.3	232.4	215.9
Error on $T_1$ (%)	–	-2.80	4.92	-1.46
Start time of 2 <sup>nd</sup> impact $T_2(\mu s)$	352.1	385.1	375.4	363.2
End time of 2 <sup>nd</sup> impact $T_3(\mu s)$	417.9	498.4	461.1	426.9

impact load and only 4.92% of error of on the duration of the first impact. Therefore, the finest discretization using  $26 \times 26$  SPH particles is used in the following investigation.

Figure 5.9: Evolution of the plate deflection and projectile stroke *vs.* time.

The deflection at the centroid of the plate shown in Figure 5.9, presents a good evolution *vs.* time when compared to the semi-analytical solution based on the Rayleigh-Ritz technique [167]. At the time  $T_1 = 232.4\mu s$ , the displacement is equal to the one of the projectile, and the first impact ends. Then the deflection of the plate increases and becomes larger than the projectile displacement, and two objects move in the opposite direction. When the centroid of the plate reaches its extreme position, it starts moving backwards. When it encounters the projectile at time  $T_2 = 375.4\mu s$ , the second impact takes place. The second

colliding comes to an end at time  $T_3 = 461.1\mu s$ , after which the plate centroid had turned around.

In what follows, the next task is to study the influence of the thickness on the maximum impact load. Thus, we performed the impact modeling for three different thicknesses  $t$ ,  $2t$  and  $4t$  of the plate. As mentioned by Abrate [144], the disturbance initiated by the impact at the centroid of the plate would travel around in the plate. After the disturbance reaches the boundary, it is reflected back, but does not have sufficient time to travel back to the point of impact. Therefore, the proposed infinite plate model is valid for these problems and this problem was classified as wave controlled impact one.

Figure 5.10 shows a comparison of the result in impact force history obtained using the present shell-SPH model and the two reference solutions: semi-analytical model of Qian and Swanson [167] and infinite plate model of Abrate [144]. One can observe from 5.10, that our results are very close to the reference solutions for all three different thicknesses. The maximum impact force  $F_{max}$  and contact duration  $T_1$  are summarized in Table 5.5.

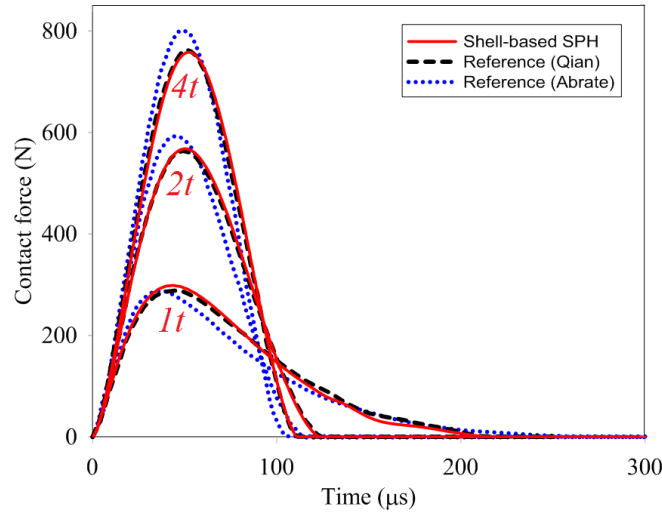


Figure 5.10: Comparison of predicted impact force for the  $t$ ,  $2t$  and  $4t$  plate thickness

The first view of Figure 5.10 indicates that, Abrate's solution (assumption of impact on infinite plate) agrees well with Qian's solution (Rayleigh-Ritz technique) when the thickness is  $t$ , but SPH solution becomes closer to Qian's solution as the thickness increases compared to the solution of Abrate. The errors of SPH model in contrast with Qian's solution are 13.9%, 6.32% and 2.27% when the plate thickness is  $t$ ,  $2t$  and  $4t$  respectively. The predicted contact duration from SPH computation are always of excellent agreement with Qian's



Table 5.5: Maximum impact force and contact duration for the  $t$ ,  $2t$  and  $4t$  plate thickness

Models	$t$		$2t$		$4t$	
	$F_{max}(N)$	$T_1(\mu s)$	$F_{max}(N)$	$T_1(\mu s)$	$F_{max}(N)$	$T_1(\mu s)$
Shell-based SPH	326.7	232.1	598.4	119.3	776.6	110.6
Reference (Qian)	286.8	219.1	562.8	124.7	759.3	111.2
Reference (Abrate)	285.4	257.4	591.7	116.5	802.7	105.5

solution. We also can remark from Table 5.5 that, the maximum impact force produced by the  $2t$ -thickness plate is nearly two times of that by  $t$ -thickness plate and the contact duration is approximately half. This observation is no longer valid when comparing the responses of the  $4t$ -thickness plate and  $2t$ -thickness plate. This implies that the effects of geometrical nonlinearities become more and more dominant.

### 5.4.3 Impact of a clamped graphite-epoxy laminate by a rigid sphere

In this application, a four-edge clamped square composite plate made of graphite-epoxy is impacted by a spherical projectile. Relative information of the plate and the projectile are detailed in Table 5.6.

Choi and Hong [168] investigated the frequency characteristics of the impact force history of this impact problem, using a FE program. Infinite plate model was also used to analyze this problem by Abrate [144]. During the predicted contact duration, the waves introduced by the impact reach the boundaries and are reflected back for many time in this finite size plate. This problem is categorized into boundary controlled impact and can not be modeled by infinite plate assumption. Then the author used a single-degree-of-freedom spring-mass model with a spring constant calculated by assuming that the plate is circular. However, higher order fluctuation of impact force history cannot be obtained. The FE solution given in [168] is employed for comparison purpose.

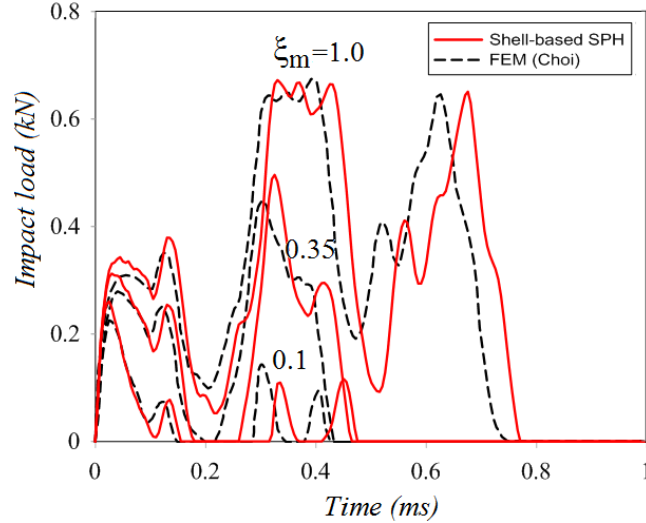
In the present investigation our developed shell-based SPH model is used for the modeling of a quarter of the plate using  $26 \times 26$  particles.

The first task is to explore the impact analysis of a spherical projectile with different masses on the laminated plate. The initial velocity of the projectile  $v$  is fixed to  $5m/s$  and the mass is controlled by a mass ratio variable  $\xi_m = M_p/M_t$  between projectile and the laminate masses. Geometrical nonlinear effects are not considered here. The results corresponding to

Table 5.6: Geometrical and material parameters of the projectile and the target

Parameters	
Target	[0/90] <sub>4s</sub> graphite-epoxy plate, fully clamped Plate size: 100mm × 100mm × 1.8mm Mass: $M_t = 28.5g$ Material properties: $E_{11} = 135.4GPa$ , $E_{22} = 9.6GPa$ , $G_{12} = 4.8GPa$ $G_{23} = 3.2GPa$ , $\nu_{12} = 0.31$ , $\rho = 1580kg/m^3$
Projectile	Sphere Radius: $R_p = 6mm$ Mass: $M_p = \xi_m M_t$ Material properties: $E_p = 207GPa$ , $\nu_p = 0.3$ Hertzian contact stiffness: $k_c = 9.513 \times 10^8 N/m^{3/2}$

$\xi_m = \{0.1, 0.35, 1\}$  are shown in Figure 5.11 and those of  $\xi_m = \{1, 3.5, 10, 35\}$  are depicted in Figure 5.12.

Figure 5.11: Evolution of the impact load *vs.* time, for  $\xi_m < 1.0$  and  $v = 5m/s$ 

From Figure 5.11, we can remark that the contact between the projectile and the plate repeats three times when  $\xi_m = 0.1$ , twice when  $\xi_m = 0.35$  and only once for the case  $\xi_m = 1$ . When  $\xi_m = 0.35$ , the maximum impact force is produced in the second impact process.

We can observe from Figure 5.12 that, just one time impact occurs between the projectile

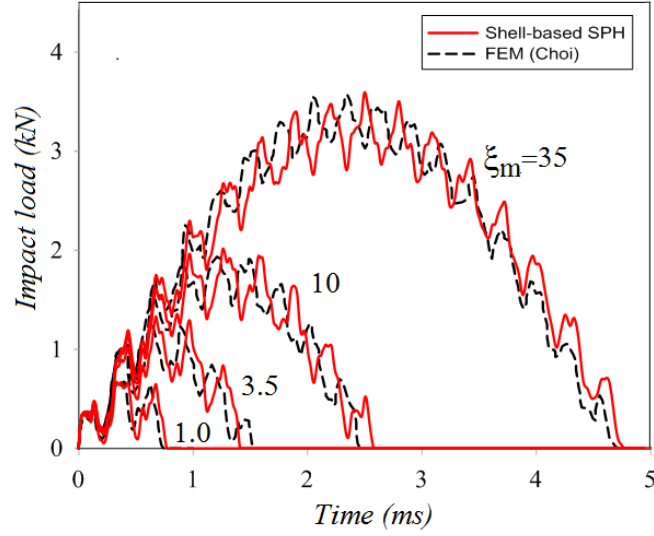


Figure 5.12: Evolution of the impact load *vs.* time, for  $\xi_m > 1.0$  and  $v = 5m/s$

and the laminated plate when  $\xi_m = \{3.5, 10, 35\}$ . Generally we can conclude that when  $\xi_m \geq 1$  contact happens only once. Figure 5.12 shows that the impact force and the contact duration become larger and longer as the mass ratio  $\xi$  increases. Also when  $\xi$  raises, the secondary fluctuations of the force history curve become smaller in comparison to the full shape of the curve. And the whole shape of the impact force history becomes increasingly similar to a sine wave. The maximum impact force  $F_{max}$  and the contact duration  $T_2$  of the impact events induced by different projectile masses are summarized in Table 5.7.

Table 5.7: Maximum impact force (N) and contact duration (ms) using different projectile masses

Models	$\xi_m = 1$		$\xi_m = 3.5$		$\xi_m = 10$		$\xi_m = 35$	
	$F_{max}$	$T_2$	$F_{max}$	$T_2$	$F_{max}$	$T_2$	$F_{max}$	$T_2$
Shell-SPH	672.7	0.78	1331.9	1.64	2017.1	2.58	3591.4	4.76
FEM (Choi)	673.5	0.75	1246.9	1.54	1997.6	2.46	3571.4	4.71

First view of Table 5.7 gives a good agreement between the SPH solution and the reference values obtained by the FE method. After computation, we find that the maximum impact force and the contact duration is roughly proportional to the square root of the projectile mass.

The second task is to perform the numerical analysis of dynamic response of the laminate impacted by the same projectile with different velocities. The mass of the projectile is

fixed  $M_p = 35M_t$  and the impact velocities are  $1m/s$ ,  $3m/s$  and  $5m/s$ . The corresponding impact force histories are shown Figure 5.13. The maximum impact force  $F_{max}$  at time  $T_1$  and the contact duration  $T_2$  are listed in Table 5.8.

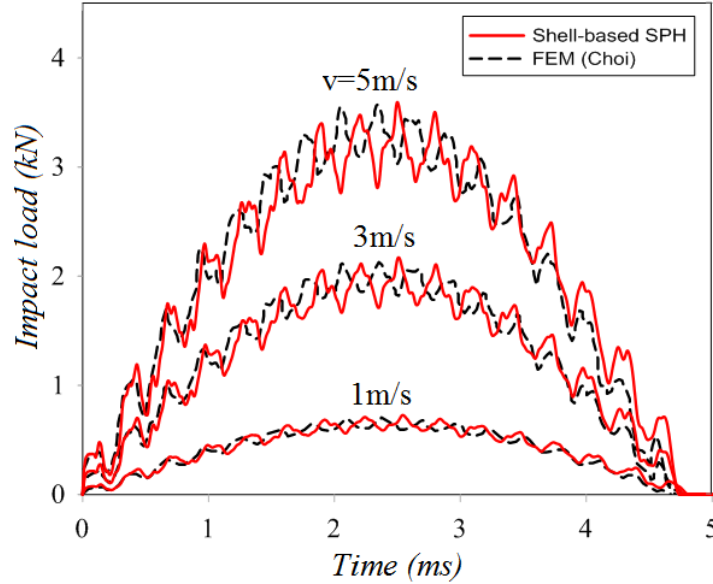


Figure 5.13: Comparison of the impact load function of the initial velocity, for  $\xi_m = 35$ .

Table 5.8: Comparison of the maximum impact load (N) and contact duration (ms) function of the initial velocity

Models	$v = 1m/s$			$v = 3m/s$			$v = 5m/s$		
	$F_{max}$	$T_1$	$T_2$	$F_{max}$	$T_1$	$T_2$	$F_{max}$	$T_1$	$T_2$
Shell-based SPH	707.7	2.24	4.81	2119.9	2.21	4.75	3473.5	2.21	4.76
FEM (Choi)	701.5	2.37	4.67	2129.2	2.35	4.78	3571.4	2.34	4.71

From Figure 5.13 and Table 5.8, we can see that the overall evolutions of the impact force for three cases are similar. As the velocity increases, the impact force history enlarges in proportion to the magnitude of the velocity. The contact duration are almost the same. Therefore, we can summarize that the contact duration and the shape of the impact force history are not dependent on the initial velocity but on the mass ratio between the projectile and the structure. Coupling the conclusion obtained from the impact responses of different mass ratios, the maximum impact force is proportional to the the square root of the initial kinetic energy of the projectile.

The third task is to consider the effects of geometric nonlinearities due to the large

deflection of the plate. To this end, all problem parameters have been fixed and only the nonlinearities are activated or not. The projectile is assumed having an initial velocity of  $2.76m/s$  and a mass  $M_p = 35M_t$ . The geometrically linear and nonlinear analysis of the impact problem were carried out, the corresponding obtained results are drawn in Figure 5.14.

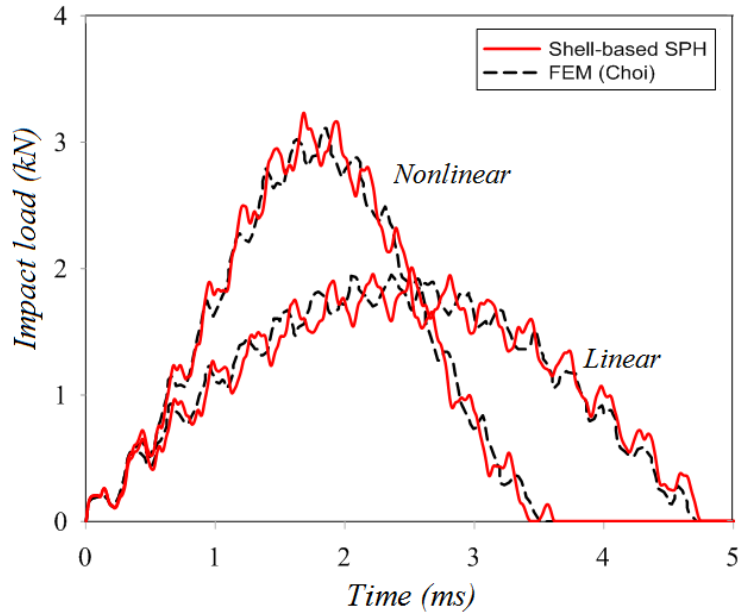


Figure 5.14: Evolution of the impact load *vs.* time for  $\xi_m = 35$  and  $v = 2.76m/s$

From Figure 5.14, we can observe the good agreement between the present shell-SPH model and the FE model used in [168]. The maximum displacement of the plate center were  $4.08mm$  and  $3.12mm$  for linear and nonlinear impact response respectively. The deflections are larger than the thickness of a plate and geometrical nonlinearities play an important role as rule of thumb. Comparing the two curves in Figure 5.14, the linear analysis underestimates the impact force and overestimates the contact duration!

## 5.5 Progressive failure analysis

### 5.5.1 Damage analysis of a carbon/epoxy square plate impacted by a point-nose projectile

In this application, we consider a laminate plate made of graphite/bismaleimide, submitted to an impact of a point-nose projectile at its center. The laminate is simply supported along all edges. The corresponding material and geometric properties of the plate and projectile

are summarized in Table 5.9.

Damage growth and distributions induced by impact were studied by Razi and Kobayashi [169] using both experimental testing and three-dimensional linear elastic FE analysis. Ganapathy and Rao [157] have also investigated this problem using a 4-noded, 48 degree-of-freedom double curved quadrilateral shell element.

Table 5.9: Parameters of the projectile and target

Parameters	
Target	$[0_4/90_4]_s$ Hitex 46/F650 graphite/bismaleimide plate, simply supported Plate size: $76.2mm \times 76.2mm$ Plate thickness: $t = 2mm$ Material properties: $E_{11} = 177.8GPa, E_{22} = 12.4GPa, G_{12} = G_{23} = 4.62GPa$ $\nu_{12} = \nu_{23} = 0.39, \rho = 1580kg/m^3$ $X_t = X_c = 1500MPa, Y_t = 40MPa$ $Y_c = 246MPa, S = 68MPa$
Projectile	Steel projectile Point-nose radius: $R_p = 3.175mm$ Mass: $M_p = 590g$ Impact velocity: $V_p = 1.931m/s$ Material properties: $E_p = 207GPa, \nu_p = 0.3, \rho_p = 7960kg/m^3$ Hertzian contact stiffness: $k_c = 8.834 \times 10^8 N/m^{3/2}$

Due to symmetry, only a quarter of the plate was modeled using the proposed shell-SPH model. Different particle distributions of  $16 \times 16$ ,  $21 \times 21$ ,  $26 \times 26$  and  $41 \times 41$  were used to model the quarter part. The damaged area of laminate from experimental tests was ultrasonic C-scanned by Razi and Kobayashi [169], which is reproduced in Figure 5.15(a). For damage analysis by numerical simulation using the Tsai-Wu criterion, the region where Tsai-Wu criterion is greater or equal to unity represents the location of the critical matrix cracking. By virtue of  $40 \times 40$  FE to discretize a quarter of the plate, Ganapathy and Rao [157] obtained the outer most damage contour by superposing the damaged area contours of all plies as shown in Figure 5.15(b). The damage area and location predicted by present shell-SPH model are depicted in Figure 5.15(c) to Figure 5.15(f) with different

particle sizes. We can observe that the damage shape predicted here coincide well to that of experimental result and FE solution. We can observe that the failure contour is much wider along the fiber direction than in the direction normal to the fiber direction. The impact energy of the projectile is  $1.1J$ , which produces only matrix cracking and no fiber fracture.

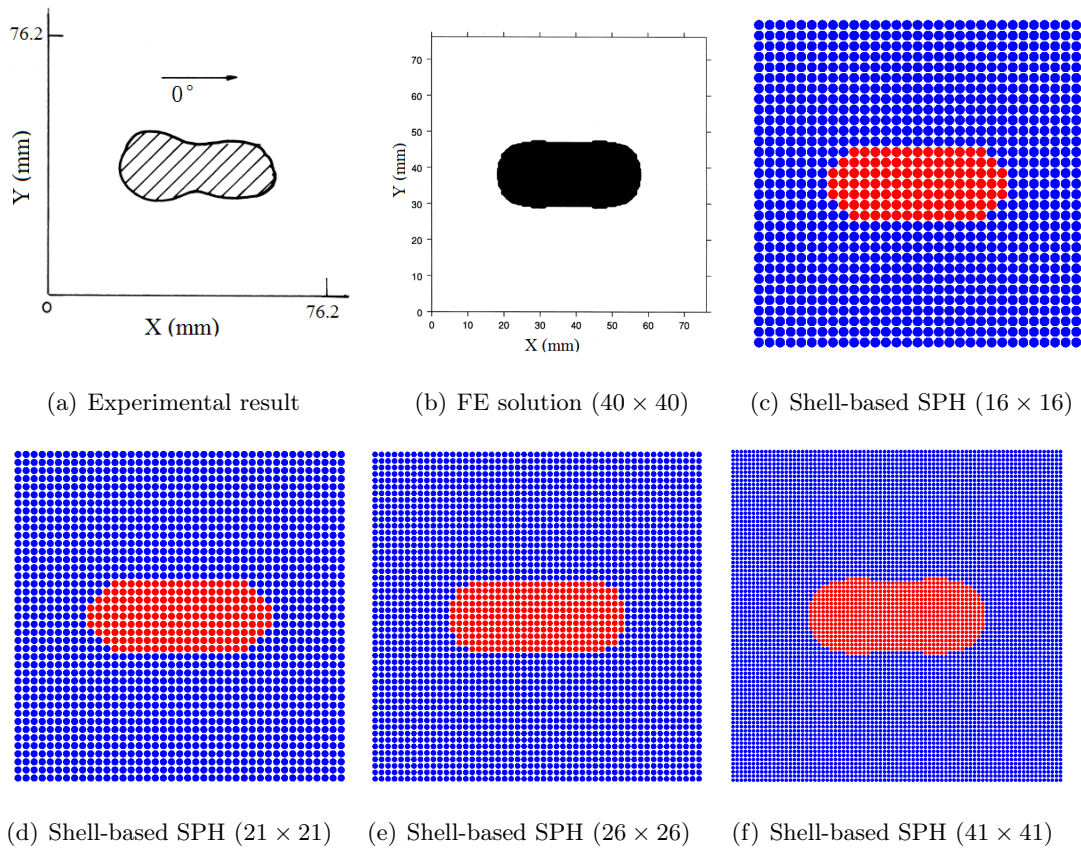


Figure 5.15: Superposed damage area and location

The approximate maximum length and width of the damage area are presented in Table 5.11 along with the experimental results and FE solution. We can remark that all shell-SPH models can predict accurately the damaged area, while comparing with FE and experimental data. Overall, the  $41 \times 41$  shell-SPH model reproduced the closest result and it is considered as a valid mesh for the following investigations.

The approximate final damaged region in each layer is presented in Figure 5.16, from bottom up. The damage of matrix crack initialed in top layer (layer No. 16) corresponding to the impact position. Then the damage propagates out around the contact zone and the largest damaged ares appears in the top layer.

Figure 5.17 shows the impact response of the laminate with and without the consideration

Table 5.10: Dimensions of damaged area

	Max. length (mm)	Max. width (mm)
Experimental Result	42.4	19.8
FE solution ( $40 \times 40$ )	39.4	18.0
Shell-based SPH ( $16 \times 16$ )	43.2	17.8
Shell-based SPH ( $21 \times 21$ )	43.8	17.1
Shell-based SPH ( $26 \times 26$ )	41.1	16.8
Shell-based SPH ( $41 \times 41$ )	41.0	18.1

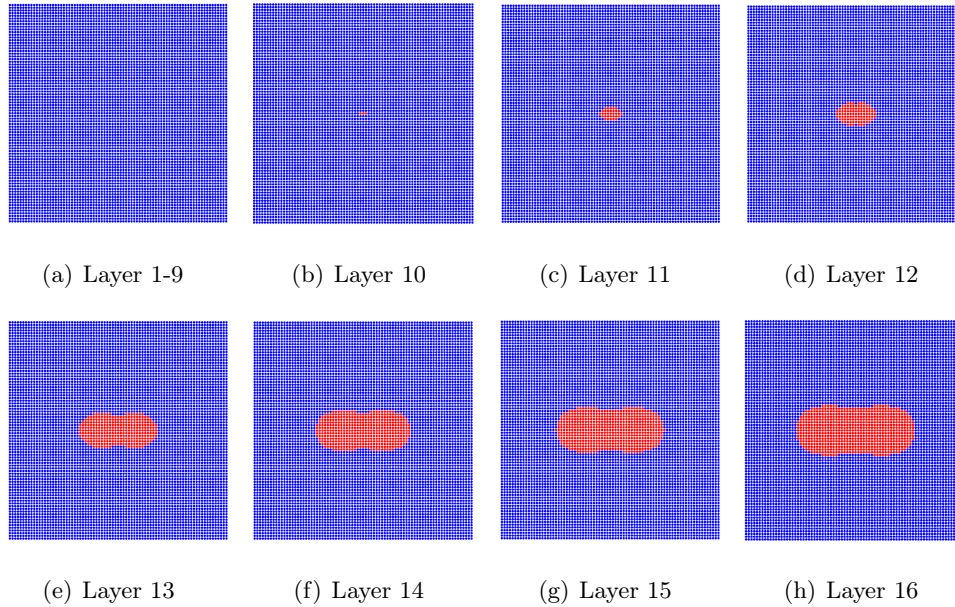
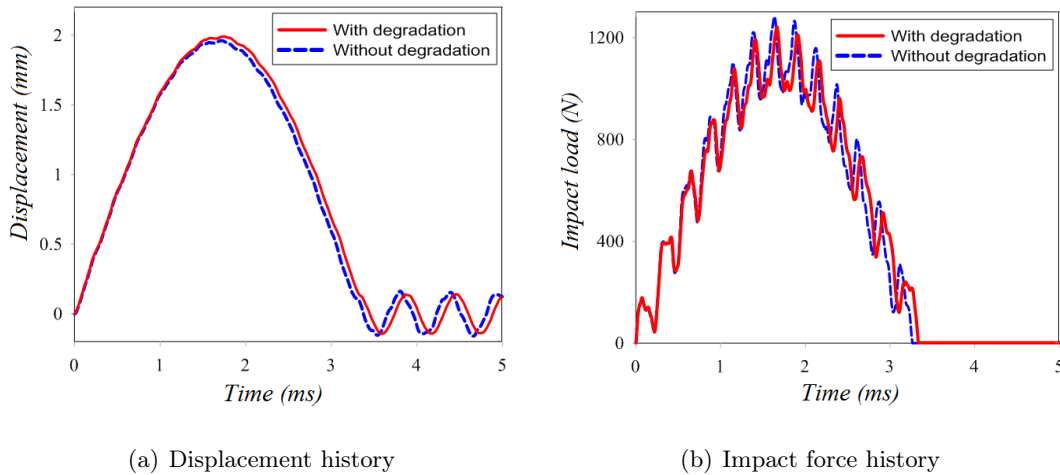


Figure 5.16: Damage area of all plies

of material properties degradation. From the above figure, we can notice that the reduced material properties just influence to a small extent the impact response. This phenomenon can be attributed to the fact that only matrix crack cannot introduce much stiffness reduction in the structure.

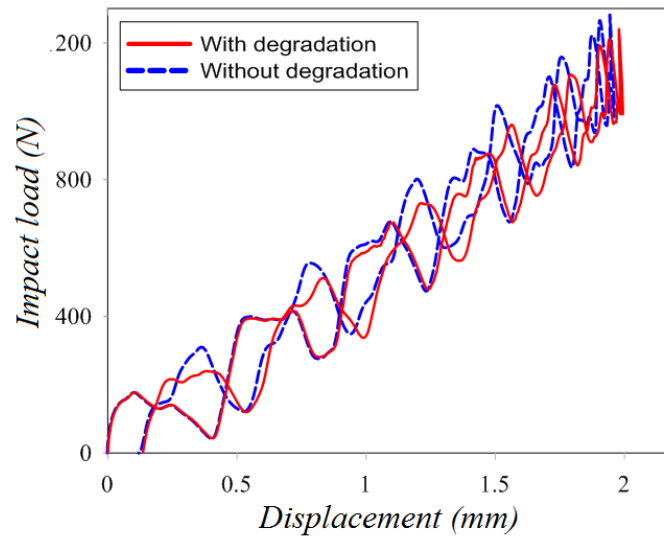
Another study on the impact of the same laminate with a projectile of a mass  $4M_p$  and an initial velocity  $V_p$  has been modeled using the present shell-SPH model. In this case, the fiber fracture initiated in the bottom layer and propagated from bottom up until the midplane. The damage of matrix crack and fiber breakage primarily occur near the impact site, but also evolve near the boundaries. The evolution of laminate center displacement and the impact load is plotted in 5.18, from which we can see that degradation of material





(a) Displacement history

(b) Impact force history



(c) Force vs. displacement

Figure 5.17: Transient reponse of the laminate impacted by  $1M_p$  mass projectile - Effect of matrix degradation.

property influences significantly the transient response. When integrating the stiffness deterioration, the normal displacement of the plate center at impact arises and the free vibration amplitude after impact ease increases. The reduced stiffness also leads to a longer contact duration and smaller impact force.

### 5.5.2 Damage analysis of a carbon/epoxy cylindrical shell panel impacted by a point-nose projectile

The last application deals with the damage analysis of a  $[0_4/90_4]_s$  symmetric cross-ply carbon/epoxy cylindrical shell panel subjected to impact by a point-nose projectile. The

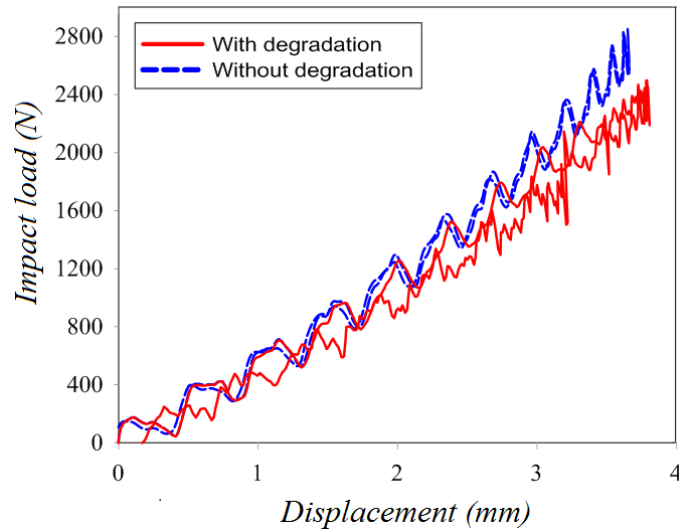
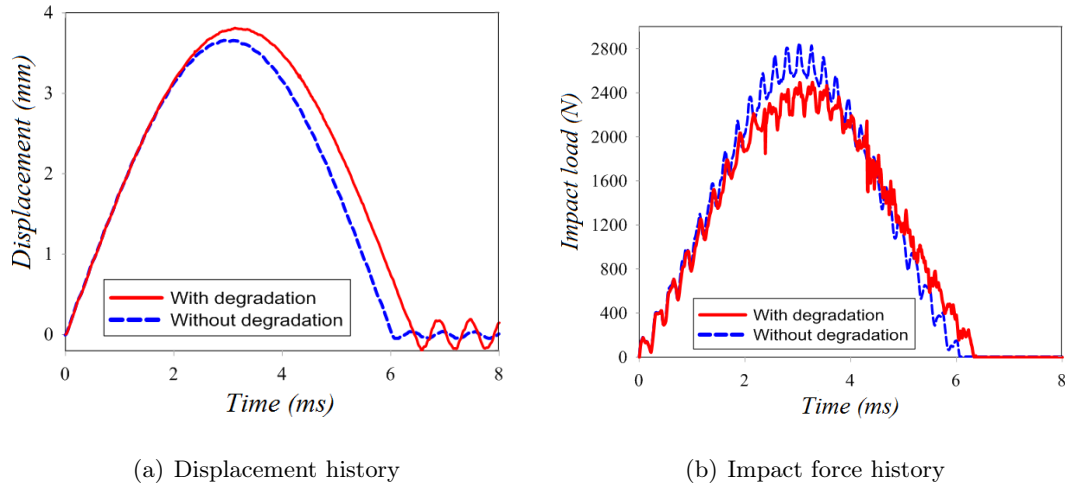


Figure 5.18: Transient reponse of the laminate impacted by  $4M_p$  mass projectile - Effect of matrix/fibers degradation.

geometry of the panel is given in Figure 5.19, where the radius  $R = 381mm$ , length  $L = 76.2mm$ , thickness  $t = 2mm$  and the angle  $\theta = 11.46^\circ$ . The material properties of the panel are identical to those used in the previous application. The same projectile impacts the panel with a velocity of  $1.647m/s$ , which corresponds an initial kinetic energy of  $0.8J$ . For symmetry reasons, only one quarter of the cylindrical shell panel was analyzed, using  $41 \times 41$  SPH particles in the present shell-SPH model and  $40 \times 40$  shell FE in the work of [157].

Damaged area was predicted in each ply and superposed on one another to get the outer most damage contour, which is plotted in Figure 5.20. The agreement between the present

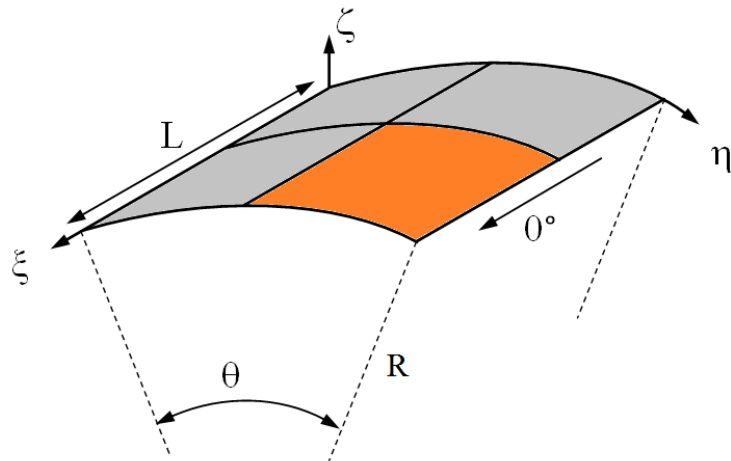


Figure 5.19: Geometry of the laminated cylindrical shell panel

shell-SPH results and the FE solution is very good. The damage is also initiated in the top ply and then spreads around the impact point, much wider along the fiber direction than in the direction normal to the fiber direction.

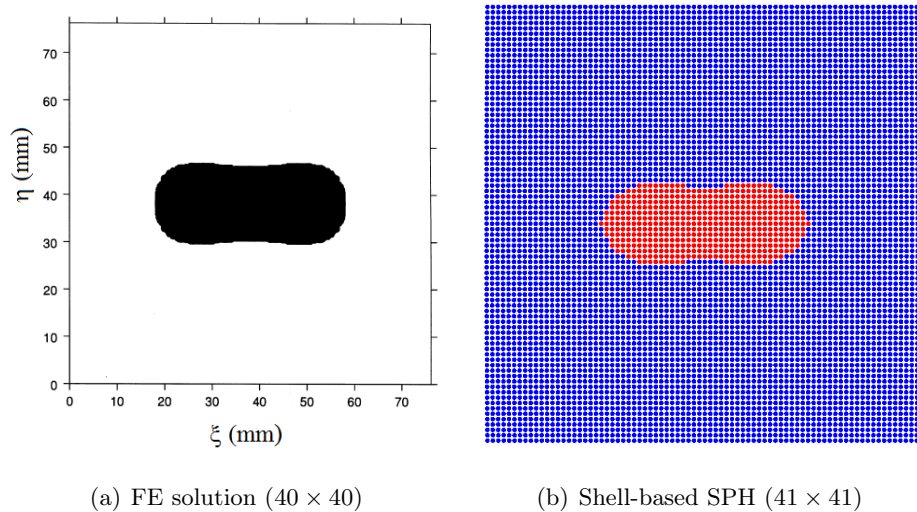


Figure 5.20: Superposed damage area and location

Table 5.11 gives the dimensions of the outer most damaged contour. The present shell-SPH model underestimates the maximum damage size compared to the FE solution given by [157].

Table 5.11: Dimensions of damaged area

	Max. length (mm)	Max. width (mm)
FE solution ( $40 \times 40$ )	39.8	16.4
Shell-SPH ( $41 \times 41$ )	37.2	14.3

## 5.6 Conclusion

In this Chapter, Shell-SPH method was used for the modeling of the transient response of isotropic and laminated structures impacted by foreign objects. The projectile was approximated by a rigid sphere and its movement is updated thanks to the explicit dynamics scheme for the time integration. Nonlinear contact law of Hertz was adopted to describe the relationship between the impact force and the indentation induced in the target. The transient response of the impacted composite structure is calculated using our developed Shell-SPH method based on the first-order shear deformation theory. Several numerical applications have been treated using the proposed methodology. Without considering the geometrical nonlinearity, the maximum impact load was varying in proportion to the projectile velocity and to the square root of its mass. The same effect of square root of the projectile mass, has been observed on the total contact duration, but the impact velocity has no influence. The geometric nonlinearities introduced in the impact modeling reveal that smaller impact force but longer contact duration can be obtained if geometric nonlinearities are not taken into account (linear transient response).

After validation of Shell-SPH impact model, the failure analysis has been included in the model by considering the Tsai-Wu failure criterion. The damage modes of matrix cracking and fiber fracture is distinguished by the maximum stress failure criterion. The correspondent degradation of elastic constants were integrated to generate a progressive damage of the structure. two numerical applications were presented in order to validate this approach.

---

# *Conclusion*

---

## **5.7 General conclusion**

The present research has been focused mainly on exploring the possibilities offered by the Smoothed Particle Hydrodynamic (SPH) method, which has been widely applied in astrophysical and fluid dynamic problems. The topic of major interest has been the modeling of laminated composite shell structures under dynamic or impulsive loading.

Primarily, the classical SPH formulation for a field and its derivatives have been modified for the analysis of 2D solids under the plane stress condition. The adaptability and accuracy of the modified SPH have been validated by simulating several benchmarks and comparing the results with solutions taken from literature and those obtained using the FE method. Geometric nonlinearities were also considered including the large transformations of solids and thin structures.

The key techniques for assuring its effectiveness consist of:

- The classical SPH method was reformulated using the Total Lagrangian Formulation which allowed reduction of the so-called tensile instability problem. In this new concept, initial configuration was taken as the reference configuration. The neighborhood of the particles was searched only once in the beginning of numerical calculation and hence CPU time is saved noticeably.
- Another defect of the classical SPH method, was the inconsistency problem, which was alleviated through the use of the Corrective Smoothed Particle Method (CSPM). This correction is based on the Taylor's series expansion and can exactly reproduce a linear function and its derivatives.
- An artificial viscous force was introduced to avoid the unphysical oscillations usually appear in the numerical calculation when dealing with problems of shocks and impacts.

In addition, the current SPH method integrated the constitutive equation to describe the stress-strain relationship, rather than the equations of state employed in the classical SPH for fluid and high-gradient-deformed solid.

Based on the robust performance of 2D-SPH method, modeling of thin-walled shell structures was conceived through a layer of particle located in the mid-surface. Mindlin-Reissner theory made it possible by degenerating the realistic three-dimensional continuum problem to two-dimensional problem. This theory took account of the transverse shear and hence made it valid for thin to thick shell structures and especially composite shells. Large rotations were treated thanks to the rotations parametrization using Rodrigues rotation formula and quaternion parameters. The artificial viscosity was also extended to shell structures.

Further more, a particular interest has been done to the large bending and buckling behaviors of multilayered composite shell structures based on the first-order shear deformation theory. Constitutive relationship of the orthotropic composite material under plane stress state and the dynamic equilibrium equations have been presented and formulated by the modified shell-SPH method.

Finally, transient response of laminate shell structures subjected to impact by foreign projectiles was investigated using the present shell-SPH method. The impact force between the projectile and target was described in function of the indentation through the use of Hertzian contact law. Damage involved by the impact was simulated thanks to the Tsai-Wu failure criterion. Maximum stress criterion was employed as a auxiliary tool to distinguish the damage form between matrix cracking and fiber breakage. Correspondent stiffness degradation was integrated to simulate progressive damage of the structure.

The good capabilities of the modified SPH method in aforementioned applications have been proven through various numerical applications involving geometrically nonlinear behavior. They were solved using the explicit dynamics scheme for the time integration. Accurate solution have been obtained when comparing with results available from the literature as well as with those obtained using the FE method.

## 5.8 Future works

Further study is warranted into:

- SPH formulation with high-order consistency should be considered, for example, Mov-

ing Least Square Particle Hydrodynamics (MLSPH) [67,68], Modified SPH (MSPH) [69], Symmetric SPH (SSPH) [70]. However, more neighbor particles need to be include in the support domain, and some difficulties merges for the boundary particles.

- Zero energy mode cannot be thoroughly removed by Total Lagrangian SPH formulation. Stress point technique [170] or Updated Lagrangian SPH formulation [171] have been reported to solve this problem.
- The locking phenomenon is not considered in this research. But for very thin shell structures, it may be severe and result in catastrophic calculation. The idea including the Discrete Kirchhoff shell formulation may constitute a good alternative.
- For impact problem, permanent indentation occurs even at relatively low loading levels. Therefore the unloading phase is significantly different from the loading phase. The permanent indentation and relative parameters have to be determined by experiment.
- For damage analysis, more damage forms (matrix tensile/shear cracking, fiber breakage, buckling and lamination) can be determined through other failure criteria, like Hashin-type failure criteria [172]. Detailed degradation of material properties can be estimated by some emerged modes or determined by experiments.
- With consideration of plastic deformation, the shell-SPH can be used in sheet metal forming, or hydroforming.





---

# Bibliography

---

- [1] GUCKENHEIMER J., "Numerical computation in the information age", *SIAM News*, vol. 31, No.5, 1998.
- [2] FERREIRA A.J.M., KANSA E.J., FASSHAUER G.E., "Progress on Meshless Methods", *Edition Springer Netherlands*, ISBN-10:9048179971, 320 pages, 2009.
- [3] LI S., LIU W.K., "Meshfree particle methods", *Edition Springer Netherlands*, ISBN-10: 3540222561, 2004.
- [4] LIU G.R., GU Y.T., "An Introduction to Meshfree Methods and Their Programming", *Edition Springer Netherlands*, ISBN-10: 1-4020-3228-5, 2005.
- [5] LIBERSKY L.D., PETSCHKE A.G., CARNEY T.C., HIPPEL J.R., ALLAHDADI F. A., "High strain Lagrangian hydrodynamics: a three-dimensional SPH code for dynamic material response", *J. Comput. Phys.*, Vol. 109, pp. 67-75, 1993.
- [6] LI S., HAO W., LIU, W.K., "Meshfree simulations shear banding under large deformation", *Int. J. Solids Struct.*, Vol. 37, pp. 7185-7206, 2000.
- [7] BELYTSCHKO T., KRONGAUZ Y., ORGAN D., FLEMING M., KRYSL P., "Meshless methods: an overview and recently developments", *Comput. Meth. Appl. Mech. Eng.*, Vol. 139, pp. 3-47, 1996.
- [8] LIU M.B., LIU G.R., LAM K.Y., ZONG Z., "Computer simulation of shaped charge detonation using meshless particle method", *Fragblast*, Vol.7, No.3, pp. 181-202, 2003.
- [9] LUCY L.B., "A numerical approach to the testing of the fission hypothesis", *Astron. J.*, Vol. 82, pp. 1013-1024, 1977.
- [10] GINGOLD R.A., MONAGHAN J.J., "Smoothed Particle Hydrodynamics: Theory and Application to Non-spherical stars", *Mon. Not. R. Astron. Soc.*, Vol. 181, pp. 375-389, 1977.
- [11] ONATE E., IDELSOHN S., ZIENKIEWICZ, O.C., TAYLOR R.L., "A finite point method in computational mechanics applications to convective transport and fluid flow", *Int. J. Numer. Meth. Eng.*, Vol. 39, No.22, pp. 3839-3866, 1996.
- [12] KANSA E.J., "Multiquadrics-A Scattered Data Approximation Scheme with Applications to Computational Fluid dynamics", *Comput. Math. Appl.*, Vol. 19, pp. 127-145, 1990.
- [13] NAYROLES B., TOUZOT G., VILLON P., "Generalizing the finite element method: diffuse approximation and diffuse elements", *Comput. Mech.*, Vol. 10, pp. 307-318, 1992.
- [14] LANCASTER P., SALKAUSKAS K., "Surfaces generated by moving least squares methods", *Math. Comput.*, Vol. 37, pp. 141-158, 1981.
- [15] BELYTSCHKO T., LU Y.Y., GU L., "Element-free Galerkin methods", *Int. J. Numer. Meth. Eng.*, Vol. 37, pp. 229-256, 1994.
- [16] KRYSL P., BELYTSCHKO T., "Analysis of thin plates by the element free Galerkin method", *Comput. Mech.*, Vol. 17, pp. 26-35, 1995.

- [17] GU Y.T., LIU G.R., "A boundary radial point interpolation method (BRPIM) for 2-D structural analyses, Structural Engineering and Mechanics", *Struct. Eng. Mech.*, Vol. 15, No. 5, pp. 535-550, 2003.
- [18] LIU W.K., JUN S., ZHANG Y.F., "Reproducing kernel particle methods", *Int. J. Numer. Meth. Eng.*, Vol. 20, pp. 1081-1106, 1995.
- [19] ATLURI S.N., ZHU T., "A new Meshless Local Petrov-Galerkin (MLPG) approach in computational mechanics", *Comput. Mech.*, Vol. 22, pp. 117-127, 1998.
- [20] DE S., BATHE K.J., "The method of finite spheres", *Comput. Mech.*, Vol. 25, pp. 329-345, 2000.
- [21] ARMANDO D.C., ODEN J.T., "Hp clouds-a meshless method to solve boundary value problems", *TICAM Report 95-05*, University of Texas at Austin, 1995.
- [22] LIU G.R., GU Y.T., "A meshfree method: meshfree weak-strong (MWS) form method, for 2-D solids", *Comput. Mech.*, Volume 33, Issue 1, pp 2-14, 2003.
- [23] LIU G.R., "Mesh Free Methods: moving beyond the finite element method", *CRC Press, Boca Raton.*, 2002.
- [24] BERCIK P., "Modeling the Star Formation in Galaxies Using the Chemo-dynamical SPH code", *Astron. Astrophys.*, Vol. 360, pp. 76-84, 2000.
- [25] GARCIA-SEN, D., BRAVO E., WOOSLEY, S.E., "Single and multiple detonations in white dwarfs", *Astron. Astrophys.*, Vol. 349, pp. 177-188, 1999.
- [26] MONAGHAN J.J., "Modeling the universe", *P. Astron. Soc. of Aust.*, Vol. 18, pp. 233-237, 1990.
- [27] GINGOLD R.A., MONAGHAN J.J., "Kernel estimates as a basis for general particle method in hydrodynamics", *J. Comput. Phys.*, Vol. 46, pp. 429-453, 1982.
- [28] HU X.Y., ADAMS N.A., "Angular-momentum conservative smoothed particle dynamics for incompressible viscous flows", *Phys. Fluids*, Vol. 18, 101702, 2006.
- [29] MORRIS J.P., ZHU Y., FOX P.J., "Parallel simulation of pore-scale flow through porous media", *Comput. Geotech.*, Vol. 25, pp. 227-246, 1999.
- [30] MONAGHAN J.J., "Gravity currents and solitary waves", *Physica D*, Vol. 98, pp. 523-533, 1996.
- [31] MONAGHAN J.J., KOCHARYAN A., "SPH simulation of multiphase flow", *Comput. Phys. Commun.*, Vol. 87, pp. 225-235, 1995.
- [32] CLEARY P.W., "Modelling confined multi-material heat and mass flows using SPH", *Appl. Math. Model.*, Vol. 22, No. 12, pp. 981-993, 1998.
- [33] CHEN J.K., BERAUN J.E., CARNEY T.C., "A corrective smoothed particle method for boundary value problems in heat conduction", *Int. J. Numer. Meth. Eng.*, Vol. 46, pp. 231-252, 1999.
- [34] COLAGROSSI A., LANDRINI M., "Numerical simulation of interfacial flows by smoothed particle hydrodynamics", *J. Comput. Phys.*, Vol. 191, No.2, pp. 448-475, 2003.
- [35] ALIA A., SOULIM., "High explosive simulation using multimaterial formulations", *Appl. Therm. Eng.*, Vol. 26, No. 10, pp. 1032-1042, 2006.
- [36] BONET J., KULASEGARAM S., "Correction and stabilization of smooth particle hydrodynamics methods with applications in metal forming simulations", *Int. J. Numer. Meth. Eng.*, Vol. 47, No. 6, pp. 1189-1214, 2000.
- [37] CLEARY P., HA J., ALGUINE V., NGUYEN T., "Flow modelling in casting processes", *Appl. Math. Model.*, Vol. 29, pp. 171-190, 2002.

- [38] GRAY J.P., MONAGHAN J.J., SWIFT R.P., "SPH elastic dynamics", *Comput. Meth. Appl. Mech. Eng.*, Vol. 190, pp. 6641-6662, 2001.
- [39] ZUKAS J. A., "High velocity impact", *John Wiley & Sons*, New York, 1990.
- [40] RANDLES P.W. CARNEY T.C, LIBERSKY L.D., RENICK J.R., PETSCHKE A.G., "Calculation of oblique impact and fracture of tungsten cubes using smoothed particle hydrodynamics", *Int. J. Impact. Engng.*, Vol. 17, pp. 661-672, 1995.
- [41] MEHRA V., CHATURVEDI S., "High velocity impact of metal sphere on thin metallic plates: A comparative smooth particle hydrodynamics study", *J. Comput. Phys.*, Vol. 212, pp. 318-337, 2006.
- [42] BENZ W., ASPHAUG E., "Simulations of brittle solids using smooth particle hydrodynamics", *Comput. Phys. Commun.*, Vol. 87, pp. 253-265, 1995.
- [43] SWEGLE J.W., ATTAWAY S.W., "On the feasibility of using smoothed particle hydrodynamics for underwater explosion calculations", *Comput. Mech.*, Vol. 17, pp. 151-168, 1995.
- [44] LIU M.B., LIU G.R., ZONG Z., LAM K.Y., "Computer simulation of the high explosive explosion using smoothed particle hydrodynamics methodology", *Comput. Fluids*, Vol. 32, pp. 305-322, 2003.
- [45] MONAGHAN J.J., "Smoothed particle hydrodynamics", *Ann. Rev. Astron. Astr.*, Vol. 30, pp. 543-574, 1992.
- [46] MONAGHAN J.J., "New developments in smoothed particle hydrodynamics. In Meshfree Methods for Partial Differential Equations, Griebel M, Schweitzer MA (eds)", *Lecture Notes in Computational Science and Engineering*, Vol. 26. Springer: Berlin, 2003.
- [47] MONAGHAN J.J., "Smoothed particle hydrodynamics", *Rep. Prog. Phys.*, Vol. 68, pp. 1703-1759, 2005.
- [48] RANDLES P.W., LIBERSKY L.D., "Smoothed particle hydrodynamics: some recent improvements and applications", *Comput. Meth. Appl. Mech. Eng.*, Vol. 139, pp. 375-408, 1996.
- [49] VIGNJEVIC R., "Review of development of the smooth particle hydrodynamics (SPH) method", *Sixth Conference on Dynamics and Control of Systems and Structures in Space*, Riomaggiore, Italy, July 2004.
- [50] LIU M.B., LIU G.R., "Smoothed particle hydrodynamics (SPH): an overview and recent developments", *Arch. Comput. Methods Engrg.*, Vol. 17, pp. 25-76, 2010.
- [51] LIU G.R., LIU M.B., "Smoothed particle hydrodynamics: a meshfree particle method", *World Scientific*, Singapore, 2003.
- [52] FANG J.N., OWENS R.G., TACHER L., PARRIAUX A., "A numerical study of the SPH method for simulating transient viscoelastic free surface flows", *J. Non-Newton. Fluid.*, Vol. 139, pp. 68-84, 2006.
- [53] ZHOU C.E., LIU G.R., HAN X., "Classic Taylor-bar impact test revisited using 3D SPH", *Springer Netherlands*, pp. 1405-1409, in *Computational Methods*, LIU G.R., TAN V.B.C., HAN X.(eds), ISBN: 978-1-4020-3952-2, 2006.
- [54] MCCARTHY M.A., XIAO J.R., PETRINIC N., KAMOULAKOS A., MELITO V., "Modelling of Bird Strike on an Aircraft Wing Leading Edge Made from Fibre Metal Laminates - Part 2: Modelling of Impact with SPH Bird Model", *Appl. Compos. Mater.*, Vol. 11, pp. 317-340, 2004.
- [55] BROWN K., ATTAWAY S., PLIMPTON S., HENDRICKSON B., "Parallel strategies for crash and impact simulations", *Comput. Meth. Appl. Mech. Eng.*, Vol. 184, pp. 375-390, 2000.
- [56] CLEARY P.W., PRAKASH M., HA J., "Novel applications of smoothed particle hydrodynamics (SPH) in metal forming", *J. Mater. Process. Technol.*, Vol. 177, pp. 41-48, 2006.

- [57] VIGNJEVIC R., DE VUYST T., CAMPBELL J., BOURNE N., "Modelling of Impact on a Fuel Tank Using Smoothed Particle Hydrodynamics", *5th International Conference on Dynamics and Control of Systems and Structures in Space (DCSSS)*, Kings College, Cambridge, July 2002.
- [58] KRYSL P., BELYTSCHKO T., "Analysis of thin shells by the element free Galerkin method", *Int. J. Num. Meth. Eng.*, Vol. 33, pp. 3057-3078, 1996.
- [59] LI S., HAO W., LIU W.K., "Numerical simulations of large deformation of thin shell structures using meshfree methods", *Comput. Mech.*, Vol. 25, pp. 102-116, 2000.
- [60] LI D., LIN Z., LI S., "Numerical analysis of Mindlin shell by meshless local petrov-galerkin method", *Acta Mech. Solida. Sin.*, Vol. 21, No.2 pp. 160-169, 2008.
- [61] MORRIS J.P., "Analysis of Smoothed Particle Hydrodynamics with Applications", *Monash University*, PhD. Thesis, 1996.
- [62] MONAGHAN J.J., LATTANZIO J.C., "A refined particle method for astrophysical problems", *Astron. Astrophys.*, Vol. 149, pp. 135-143, 1985.
- [63] FULK D.A., "A numerical analysis of smoothed particle hydrodynamics", *Air Force Institute of Technology*, PhD. Thesis, 1994.
- [64] LIBESKY L.D., PETSCHKE A.G., "Smoothed particle hydrodynamics with strength of materials", in *Advances in the Free-Lagrange Method Including Contributions on Adaptive Gridding and the Smooth Particle Hydrodynamics Method, Lecture Notes in Physics*, Trease H, Fritts J, Crowley W (eds). Springer: New York, Vol. 395, pp. 248-257, 1991.
- [65] RANDLES P.W., LIBESKY L.D., "Smoothed particle hydrodynamics some recent improvements and applications", *Comput. Meth. Appl. Mech. Eng.*, Vol. 138, pp. 375-408, 1996.
- [66] JUN S., LIU W.K., BELYTSCHKO T., "Explicit reproducing kernel particle methods for large deformation problems", *Int. J. Numer. Meth. Eng.*, Vol. 41, pp. 137-166, 1998.
- [67] DILTS G.A., "Moving-Least-Squares-particle hydrodynamics I: Consistency and stability", *Int. J. Numer. Meth. Eng.*, Vol.44, pp. 1115-1155, 1999.
- [68] DILTS G.A., "Moving least square particle hydrodynamics II: conservation and boundaries", *Int. J. Numer. Meth. Eng.*, Vol. 48, pp. 1503-1524, 2000.
- [69] ZHANG G.M., BATRA R.C., "Modified Smoothed Particle Hydrodynamics Method and Its Application to Transient Problems", *Comput. Mech.*, Vol. 34, pp. 137-146, 2004.
- [70] BATRA R.C., ZHANG G.M., "SSPH Basis Functions for Meshless Methods, and Comparison of Solutions with Strong and Weak Formulations", *Comput. Mech.*, Vol. 41, pp. 527-545, 2008.
- [71] CHEN JK, BERAUN JE, "A generalized smoothed particle hydrodynamics method for nonlinear dynamic problems", *Comput. Method. Appl. Mech. Eng.*, Vol. 190, pp. 225-239, 2000.
- [72] VON NEUMANN J., RICHTMYER R.D., "A method for the numerical calculation of hydrodynamic shocks", *J. Appl. Phys.*, Vol. 21, pp. 232-247, 1950.
- [73] MONAGHAN J.J., GINGOLD R.A., "Shock simulation by the particle method of SPH", *J. Comput. Phys.*, Vol. 52, pp. 374-381, 1983.
- [74] SWEGLE J.W., ATTAWAY S.W., HEINSTEIN M.W., MELLO F.J., HICKS D.L., "An analysis of smoothed particle hydrodynamics", *Sandia Report SAND94-2513*, Sandia National Lab., Alb. NM 87185, 1994.
- [75] BALSARA D.S., "Von Neumann stability analysis of smoothed particle hydrodynamics-suggestions for optimal algorithms", *J. Comput. Phys.*, Vol. 121, pp. 357-372, 1995.
- [76] ADAMS B., WICKE M., "Meshless approximation methods and applications in physics based modeling and animation", *In Eurographics 2009 Tutorials.*, pp. 213-239, 2009.

- [77] MONAGHAN, J.J., "SPH without a Tensile Instability", *J. Comput. Phys.*, Vol. 159, pp. 290-311, 2000.
- [78] BELYTSCHKO T., GUO Y., LIU W.K., XIAO S.P., "A unified stability analysis of meshless particle methods", *Int. J. Numer. Meth. Eng.*, Vol. 48, pp. 1359-1400, 2000.
- [79] ADHIKARI S., "Damping Models for Structural Vibrations", *Cambridge University Engineering Department*, Cambridge, U.K., Ph.D. Thesis, 2000.
- [80] LIU C.H., LEE K.M., "Dynamic modeling of damping effects in highly damped compliant fingers for applications involving contacts", *ASME J. Dyn. Syst-T ASME.*, Vol. 134, No. 1, pp. 011005.1-011005.9, 2012.
- [81] D.J. BENSON, "Computational methods in Lagrangian and Eulerian hydrocodes", *Comput. Meth. Appl. Mech. Engr.*, Vol. 99, pp. 2356-2394, 1992.
- [82] TIMOSHENKO S.P., GERE J.M., "Mechanics of materials", *D. Van Nostrand Company*, New York, ISBN-13: 9780442226374, 1972.
- [83] MAUREL B., "Modélisation par la méthode SPH de l'impact d'un réservoir rempli de fluide", *INSA de lyon*, PhD thesis, 2008.
- [84] MAUREL B., COMBESURE A., "An SPH shell formulation for plasticity and fracture analysis in explicit dynamics", *Int. J. Numer. Meth. Eng.*, Vol. 76, No. 7, pp. 949-971, 2008.
- [85] "LS-DYNA Keyword User's Manual, Vol. I (revision: 3937)", *Edition Livermore Software Technology Corporation (LSTC)*, 2321 pages, Livermore, California, USA, October 17, 2013.
- [86] COOK R.D., "Improved two dimensional finite element", *J. Struct. Div-ASCE.*, Vol. 100, No. 9, pp. 1851-1863, 1974.
- [87] WISNIEWSK K., "Finite Rotation Shells Basic Equations and Finite Elements for Reissner Kinematics", *Edition Springer*, ISBN: 978-90-481-8760-7, 483 pages, 2010.
- [88] SABI, A.B., LOCK A.C., "The applications of finite elements to large deflection geometrically nonlinear behaviour of cylindrical shells In, Brebbia, C.A. and Tottenham, H. (eds.) Variational methods in engineering: proceedings on an international conference held at the University of Southampton", *Southampton University Press*, Southampton, UK, 7/54-7/65, 1972.
- [89] YAU J.D., YANG Y.B., "Geometrically nonlinear analysis of planar circular arches based on rigid element concept - A structural approach", *Int. J. Numer. Meth. Eng.*, Vol. 30, pp. 955-964, 2008.
- [90] WRIGGERS P., SIMO J.C., "A general procedure for the direct computation of turning and bifurcation", *Eng. Struct.*, Vol. 30, pp. 155-176, 1990.
- [91] KEMMOCH, K., UEMURA M., "Measurement of Stress Distribution in Sandwich Beams under Four-Point Bending", *Exp. Mech.*, Vol. 20, pp. 80-86, 1980.
- [92] BELYTSCHKO T., LIU W.K., MORAN B., "Nonlinear Finite Elements for Continua and Structures", *John Wiley & Sons*, ISBN: 0471987743, 2000.
- [93] NOGUCHI H., KAWASHIMA T., MIYAMURA T., "Element free analyses of shell and spatial structures", *Int. J. Numer. Meth. Engng.*, Vol. 47, pp. 1215-1240, 2000.
- [94] LONG S., ATLURI S.N., "A meshless local Petrov-Galerkin method for solving the bending problem of a thin plate", *CMES-Comp. Model. Eng.*, Vol.3, No.1, pp.53-63, 2002
- [95] MING F.R., ZHANG A.M., CAO X.Y., "A robust shell element in meshfree SPH method", *Acta Mech. Sin.*, Vol. 29, pp. 241-255, 2013.
- [96] CALEYRON F., COMBESURE A., FAUCHER V., POTAPOV S., "Dynamic simulation of damage-fracture transition in smoothed particles hydrodynamics shells", *Int. J. Numer. Meth. Eng.*, Vol. 90, pp. 707-738, 2012.

- [97] BATOZ J.L., DHATT G., "Structural modeling by the finite element method. Vol 3. (in French)", *Edition Hermès Paris*, ISBN-10: 2866013042, 1992.
- [98] ZIENKIEWICZ O.C., TAYLOR R.L., "The Finite Element Method for Solid and Structural Mechanics, 6th Edition", *Elsevier Butterworth-Heinemann*, ISBN 0 7506 6321 9, 2005.
- [99] P. BETSCH, A. MENZEL, E. STEIN, "On the parametrization of finite rotations in computational mechanics", *Comput. Meth. Appl. Mech. Eng.*, Vol. 155, pp. 273-305, 1998.
- [100] IBRAHIMBEGOVIC A., "On the choice of finite rotation parameters", *Comput. Meth. Appl. Mech. Eng.*, Vol. 149, pp. 49-71, 1997.
- [101] IBRAHIMBEGOVIC A., "On finite element implementation of geometrically nonlinear Reissner's beam theory: three-dimensional curved beam elements", *Comput. Method. Appl. M.*, Vol. 122, pp. 11-26, 1995.
- [102] REDDY J.N., "Mechanics of Laminated Composite Plates and Shells: Theory and Analysis, 2nd edition", *CRC Press*, ISBN 9780849315923, 2004.
- [103] GORIELY A., VANDIVER R., DESTRADE M., "Nonlinear Euler buckling", *P. Roy. Soc. A-Math. Phys.*, Vol. 464, pp. 3003-3019, 2008.
- [104] YOUNG W.C., BUDYNAS R.G., "Roark's formulas for stress and strain, 7-th Edition", *McGraw-Hill*, ISBN 0-07-072542-X, New York, 2002.
- [105] KLINKEL S., GRUTTMANN F., WAGNER W., "A continuum based 3D-shell element for laminated structures", *Comput. Struct.*, Vol. 71, pp. 43-62, 1999.
- [106] LEICESTER R.H., "Finite deformations of shallow shells", *J. Eng. Mech. Div. ASCE*, Vol. 94 (EM 2), pp. 1409-1423, 1968.
- [107] BUCALEM M.L., BATHE K.J., "Finite Element Analysis of Shell Structures, Archives of Computational Methods in Engineering", *Arch. Comput. Method E.*, Vol. 4, No. 1, pp. 3-61, 1997.
- [108] GAY D., HOA S.V., "Composite Materials: Design And Applications", *Edition CRC Press Inc (2nd edition)*, ISBN-10: 1420045199, 568 pages, 2007.
- [109] VALCHOUTSIS S., "Shear correction factors for plates and shells", *Int. J. Numer. Meth. Eng.*, Vol. 33, pp. 1537-1552, 1992.
- [110] MADABHUSI-RAMAN P., DAVALOS J.F., "Static shear correction factor for laminated rectangular beams", *Compos. Part. B-ENG.*, Vol. 27, pp. 285-293, 1996.
- [111] SLEIGHT D.W., "Progressive failure analysis methodology for laminated composite structures", *NASA/TP-19999-209107*, Washington DC, 20546-0001, 1999.
- [112] REDDY Y.S.N., REDDY J.N., "Linear and non-linear failure analysis of composite laminates with transverse shear", *Comput. Sci. Technol.*, Vol. 44, pp. 227-255, 1992.
- [113] ZHANG Y.X., KIM K.S., "A simple displacement-based 3-node triangular element for linear and geometrically nonlinear analysis of laminated composite plates", *Comput. Meth. Appl. Mech. Eng.*, Vol. 194, pp. 4607-4632, 2005.
- [114] MOITA J.S., MOTA SORES C.M., MOTA SOARES C.A., "Buckling behaviour of laminated composite structures using a discrete higher-order displacement field", *Comput. Struct.*, Vol. 35, pp. 75-92, 1996.
- [115] LIEW K.M., HUANG Y.Q., "Bending and buckling of thick symmetric rectangular laminates using the moving least-squares differential quadrature method", *Int. J. Mech. Sci.*, Vol. 45, No. 1, pp. 95-114, 2003.
- [116] XIAO J.R., GILHOOLEY D.F., BATRA R.C., GILLESPIE JR J.W., MCCARTHY M.A., "Analysis of thick composite laminates using a higher-order shear and normal deformable plate theory (HOSNDPT) and a meshless method", *Compos. Part B-Eng.*, Vol. 39, pp. 414-427, 2008.

- [117] FERREIRA A.J.M., BATRA R.C., ROQUE C.M.C., QIAN L.F., MARTINS P.A.L.S., "Static analysis of functionally graded plates using third-order shear deformation theory and a meshless method", *Compos. Struct.*, Vol. 69, No.4, pp. 449-457, 2005.
- [118] WANG J., LIEW K.M., TAN M.J., RAJENDRAN S., "Analysis of rectangular laminated composite plates via FSDT meshless method", *Int. J. Mech. Sci.*, Vol. 44, pp. 1275-1293, 2002.
- [119] SINGH J., SHUKLA K.K., "Nonlinear flexural analysis of functionally graded plates under different loading using RBF based meshless method", *Eng. Anal. Bound. Elem.*, Vol. 36, pp. 1819-1827, 2012.
- [120] SINGH S, SINGH J, SHUKLA KK, "Buckling of laminated composite plates subjected to mechanical and thermal loads using meshless collocations", *J. Mech. Sci. Technol.*, Vol. 27, No. 2, pp. 327-336, 2013.
- [121] LIEW .KM., ZHAO X., FERREIRA A.J.M., "A review of meshless methods for laminated and functionally graded plates and shells", *Compos. Struct.*, Vol.93, pp. 2031-2041, 2011.
- [122] SHINTATE K., SEKINE H., "Numerical simulation of hypervelocity impacts of a projectile on laminated composite plate targets by means of improved SPH method", *Compos. Part A-Appl. S.*, Vol. 35, pp. 683-692, 2004.
- [123] MEDINA D.F., CHEN J.K., "Three-dimensional simulations of impact induced damage in composite structures using the parallelized SPH method", *Compos. Part A-Appl. S.*, Vol. 31, pp. 853-860, 2000.
- [124] GRIMALDI A., SOLLO A., GUIDA M., MARULO F., "Parametric study of a SPH high velocity impact analysis - A bird strike windshield application", *Compos. Struct.*, Vol. 96, pp. 616-630, 2013.
- [125] MAVEL S., "Development of a numerical tool for design of sandwich structures subjected to impact at intermediate velocity", , PHD thesis (in French), University of Valenciennes; 2012.
- [126] ZHANG Y.X., YANG C.H., "A family of simple and robust finite elements for linear and geometrically nonlinear analysis of laminated composite plates", *Compos. Struct.*, Vol. 75, pp. 545-552, 2006.
- [127] KANT T., KOMMINENI J.R., "C<sup>0</sup> finite element geometrically non-linear analysis of fibre reinforced composite and sandwich laminates based on a higher-order theory", *Comput. Struct.*, Vol. 45, pp. 511-520, 1992.
- [128] GORGI M., "On large deflection of symmetric composite plates under static loading", *Proc. Inst. Mech. Eng.*, Vol. 200, pp. 13-19, 1986.
- [129] NAFEMS, "National Agency for Finite Element Methods and Standards (NAFEMS)", *Test R0031/2 from NAFEMS publication R0031*, Composites Benchmarks, Issue 2, February 5, U.K., 2001.
- [130] LASCHET G., JEUNETTE J.P., "Postbuckling finite element analysis of composite panels", *Comput. Struct.*, Vol. 14, pp. 35-48, 1990.
- [131] BRANK B., PERIC D., DAMJANIC F.B., "On implementation of a nonlinear four node shell finite element for thin multilayered elastic shells", *Comput. Mech.*, Vol. 16, pp. 341-359, 1995.
- [132] BALAH M., AL-GHAMEDY H.N., "Finite element formulation of a third- order laminated finite rotation shell element", *Comput. Struct.*, Vol. 80, pp. 1975-1990, 2002.
- [133] TO CWS, WANG B, "Transient responses of geometrically nonlinear laminated composite shell structures", *Finite Elem. Anal. Des.*, Vol. 31, pp. 117-134, 1998.
- [134] YANG S.H., SUN C.T, "Indentation law for composite laminates", *ASTM STP*, Vol. 787, pp. 425-429, 1982.
- [135] TAN T.M., SUN C.T., "Use of static indentation laws in the impact analysis of laminated composite plates", *J. Appl. Mech.*, Vol. 52, pp. 6-12, 1985.
- [136] SUEMASU H., HERTH S., MAIER M, "Indentation of spherical head indentors on transversely isotropic composite plates", *J. Compos. Mater.*, Vol. 28, Issue. 17, pp. 1723-1739, 1994.

- [137] WU E., YEN C.-S., "The contact behavior between laminated composite plates and rigid spheres", *J. Appl. Mech.*, Vol. 61, pp. 60-66, 1994.
- [138] CHOI I.K.H., LIM C.H., "Low-velocity impact analysis of composite laminates using linearized contact law", *Compos. struct.*, Vol. 66, pp. 125-132, 2004.
- [139] SETOODEH A.R., MALEKZADEH P., NIKIBIN K., "Low velocity impact analysis of laminated composite plates using a 3D elasticity based layerwise FEM", *Mater. Design*, Vol. 30, pp. 3795-3801, 2009.
- [140] PIERSON M.O., VAZIRI R., "Analytical solution for low-velocity impact response of composite plates", *AIAA J.*, Vol. 34, No.8, pp. 1633-1640, 1996.
- [141] SUN C.T., "An analytical method for evaluation of impact damage energy of laminated composites", *ASTM Spec. Tech. Publ.*, Vol. 617, pp. 427-440, 1977.
- [142] NALLIM L.G., RICARDO O.G., "Natural frequencies of symmetrically laminated elliptical and circular plates", *Int. J. Mech. Sci.*, Vol. 50, Issue 7, pp. 1153-1167, 2008.
- [143] SHIVAKUMAR K. N., ELBER W., ILLG W., "Prediction of impact force and duration due to low-velocity impact on circular composite laminates", *J. Appl. Mech.*, Vol. 52, pp. 674-680, 1985.
- [144] ABRATE S., "Modeling of impacts on composite structures", *Comput. Struct.*, Vol. 51, pp. 129-138, 2001.
- [145] ABRATE S., "Impact on Composite Structures", *Cambridge University Press*, ISBN-10 0-521-47389-6, 2005.
- [146] OLSSON R., "Impact response of orthotropic composite plates predicted from a one-parameter differential equation", *AIAA J.*, Vol. 30, No. 6, pp. 1587-1596, 1992.
- [147] CHUN K. S., KASSEGNE S. K., "Low-Velocity Impact Dynamic Behavior of Laminated Composite Nonprismatic Folded Plate Structures", *J. Eng. Mech.-ASCE*, Vol. 131, No. 7, pp. 678-688, 2005.
- [148] HERTZ H., "Über die berührung fester elastischer körper", *Journal für die reine und angewandte Mathematik*, Vol. 92, pp. 156-171, 1881.
- [149] JOHNSON K.L., "Contact Mechanics", *Cambridge University Press*, ISBN : 0-521-34796-3, 454 pages, 2003.
- [150] KRECU LJ D., RASUO B., "Review of impact damages modelling in laminated composite aircraft structures", *Technical Gazette*, Vol. 20, pp. 485-495, 2013.
- [151] SJOBLUM P.O., HARTNESS J.T., CORDELL T.M., "On low-velocity impact testing of composite materials", *J. Compos. Mater.*, Vol. 22, pp. 30-52, 1988.
- [152] SHIVAKUMAR K.N., ELBER W., ILLG W., "Prediction of low-velocity impact damage in thin circular laminates", *AIAA J.*, Vol. 23, pp. 442-449, 1985.
- [153] KUMAR K., "Analysis of impact response and damage in laminated composite shell involving large deformation and material degradation", *J. Mech. Mater. Struct.*, Vol. 3, No. 9, pp. 1741-1756, 2008.
- [154] CHOI H.Y., DOWNS R.J., CHANG F.K., "A new approach toward understanding damage mechanisms and mechanics of laminated composites due to low-velocity impact: Part I experiments", *J. Compos. Mater.*, Vol. 25, pp. 992-1011, 1991.
- [155] CHOI H.Y., DOWNS R.J., CHANG F.K., "A new approach towards understanding damage mechanisms and mechanics of laminated composites due to low-velocity impact: Part II-Analysis", *J. Compos. Mater.*, Vol. 25, pp. 1012-1038, 1991.
- [156] CHOI H.Y., CHANG F.K., "A model for predicting damage in graphite/epoxy laminated composites resulting from low-velocity point impact", *J. Compos. Mater.*, Vol. 26, No. 6, pp. 2134-2169, 1992.



- [157] GANAPATHY S., RAO K.P., "Failure analysis of laminated composite cylindrical/spherical shell panel subjected to low-velocity impact", *Comput. Struct.*, Vol. 68, pp. 627-641, 1998.
- [158] KRISHNAMURTHY K.S., MAHAJAN P., MITTAL R.K., "A parametric study of the impact response and damage of laminated cylindrical composite shells", *Compos. Sci. Technol.*, Vol. 61, pp. 1655-1669, 2001.
- [159] ZHAO G.P., CHO C.D., "Damage initiation and propagation in composite shells subjected to impact", *Comput. Struct.*, Vol. 78, pp. 91-100, 2007.
- [160] TSAI S.W., WU E.M., "A general theory of strength for anisotropic materials", *J. Comp. Mater.*, Vol. 5, pp. 58-80, 1971.
- [161] TSAI S.W., "A Survey of Macroscopic Failure Criteria for Composite Materials", *J. Reinf. Plast. Comp.*, Vol. 3, pp. 40-62, 1984.
- [162] HOU J.P., PETRINIC N., RUIZ C., HALLETT S.R., "Prediction of impact damage in composite plates", *Compos. Sci. Technol.*, Vol. 60, pp. 273-281, 2000.
- [163] LI C.F., HU N., YIN Y.J., SEKINE H., FUKUNAGA H., "Low-velocity impact-induced damage of continuous fiber-reinforced composite laminates. Part I. An FEM numerical model", *Compos. Part A-Appl. S.*, Vol. 33, pp. 1055-1062, 2002.
- [164] KARAS K., "Platten Unter Seitlichen Stoss", *Ing. Arch.*, Vol. 10, Issue, 4 pp. 237-250, 1939.
- [165] MAHAJANA P., DUTTA A., "Adaptive computation of impact force under low velocity impact", *Comput. Struct.*, Vol. 70, pp. 229-241, 1999.
- [166] WU H.Y.T., CHANG F.K., "Transient dynamic analysis of laminated composite plates subjected to transverse impact", *Comput. Struct.*, Vol. 31, Issue 3, pp. 453-466, 1989.
- [167] QIAN Y., SWANSON S.R., "A comparison of solution techniques for impact response of composite plates", *Comput. Struct.*, Vol. 14, pp. 177-192, 1990.
- [168] CHOI I.H., HONG C.S., "New approach for simple prediction of impact force history on composite laminates", *AIAA J.*, Vol. 32, No. 10, pp. 2067-2072, 1994.
- [169] RAZI H., KOBAYASHI A.S., "Delamination in cross-ply laminated composite subjected to low-velocity impact", *AIAA J.*, Vol. 31, pp. 1498-1502, 1993.
- [170] DYKA C.T., RANDLES P.W., INGEL R.P., "Stress points for tension instability in SPH", *Int. J. Numer. Meth. Eng.*, Vol. 40, No. 13 pp. 2325-2341, 1997.
- [171] VIDAL Y., BONET J., HUERT A., "Stabilized updated Lagrangian corrected SPH for explicit dynamic problems", *Int. J. Numer. Meth. Eng.*, Vol. 69, Issue 13, pp. 2687-2710, 2007.
- [172] CESARI F., DAL RE V., MINAK G., ZUCHELLI A., "Damage and residual strength of laminated carbon/epoxy composite circular plates loaded at the centre", *Compos. Part A-Appl. S.*, Vol. 38, pp. 1163-1173, 2007.

**Title :**

Nonlinear transient analysis of isotropic and composite shell structures under dynamic loading by SPH method

**Abstract:**

The objective of this thesis is the development and the extension of the SPH method for the analysis of isotropic and multilayered composite shell structures, undergoing dynamic loading. Major defects of the classical SPH method such as the lack of consistency, the tensile instability are solved by "Corrective Smoothed Particle Method", the use of the Total Lagrangian Formulation and artificial viscosity. Mindlin-Reissner Theory is employed for the modeling of thick shells, by using only one layer of particles in the mid-plane. The strong form of the governing equations for shell structures are discretized directly by the modified SPH method and solved using the central difference time integration scheme. An extension of the method has been introduced for the modeling of low-velocity impact of shells by rigid impactors. The contact force is calculated based on the Hertzian contact law. A last extension of the SPH method concerns the integration of Tsai-Wu failure criterion for the modeling of progressive degradation of multilayered structures.

**Keyword :**

SPH; shell; Nonlinearities; Composites; Impact; Progressive failure.

**Titre :**

Modélisation du comportement non linéaire transitoire de structures coques isotropes et composites sous chargement dynamique par méthode SPH

**Résumé :**

L'objectif de cette thèse est le développement et l'extension de la méthode SPH pour l'analyse de structures de type coque, isotropes et composites multicouches soumises à des chargements dynamiques. Les différents verrouillages de la méthode SPH classique, tels que la non consistence, l'instabilité en traction, sont résolus par la méthode dite "Corrective Smoothed Particle Method", l'utilisation d'une Formulation Lagrangienne Totale et l'introduction de viscosité artificielle. Le modèle de coque basé sur la théorie de Reissner-Mindlin est adopté pour la modélisation des structures de coque épaisses en utilisant une seule couche de particules dans le plan moyen. La forme forte d'équations gouvernantes de coque sont discrétisées directement par la méthode SPH améliorée et résolues par un schéma explicite basé sur les différences finies centrées. Une extension de la méthode a été faite pour la modélisation d'impact de coques par des objets rigides à faible vitesse. La force de contact est calculée en utilisant la théorie de Hertz. Une dernière extension de la méthode concerne l'intégration du critère de rupture de Tsai-Wu pour la modélisation de la dégradation progressive pour les structures composites multicouches.

**Mots-clés :**

SPH; Coque; Non linéarités; Composites; Impact; Rupture progressive.